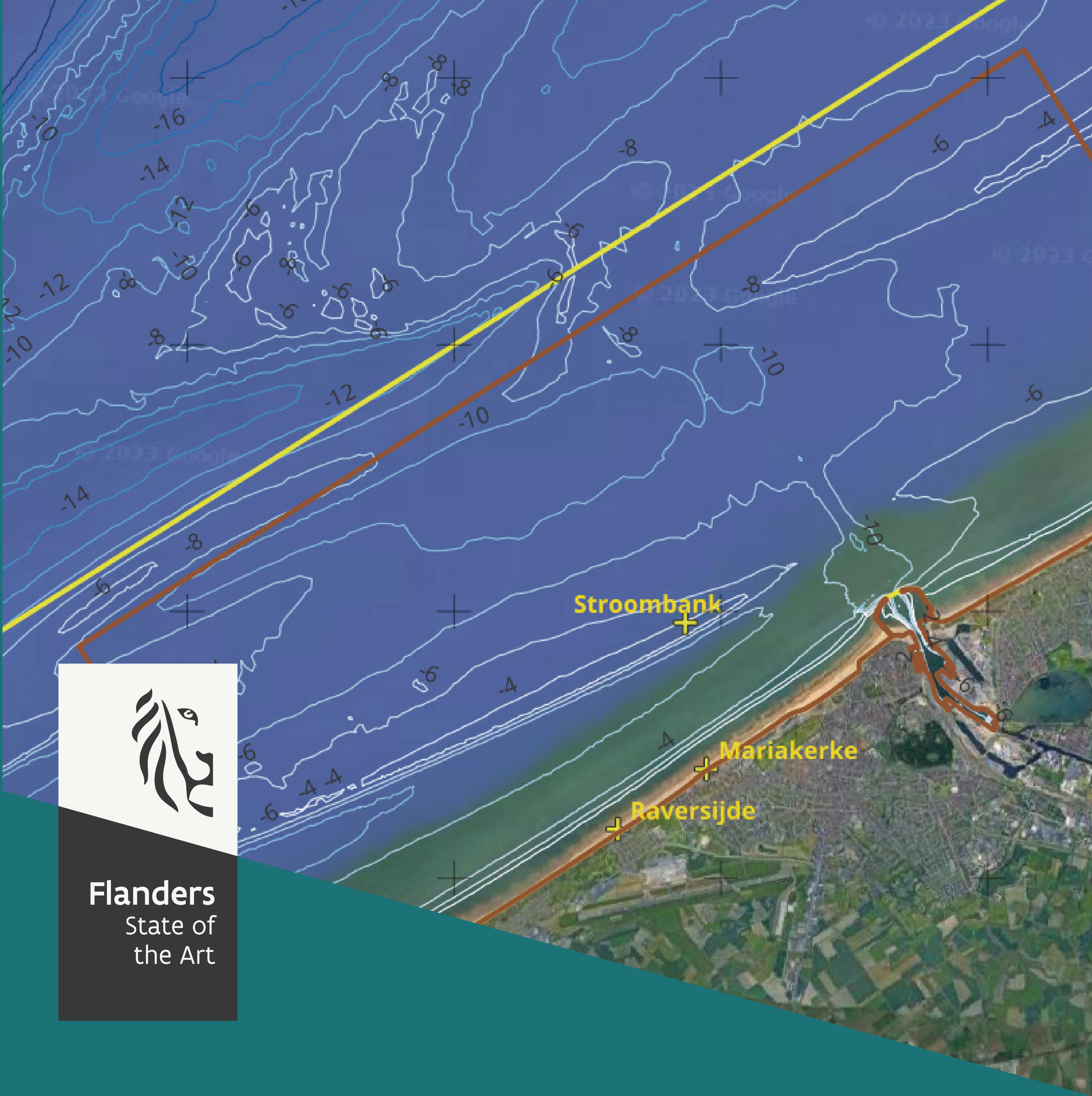

Flanders
State of
the Art

21_104_4
FH reports

Morphodynamic modelling of the Belgian Coastal zone

Sub report 4 – Cross-shore transport modelling with GAIA: Ostend model

DEPARTMENT
MOBILITY &
PUBLIC
WORKS

www.flandershydraulics.be

Morphodynamic modelling of the Belgian Coastal zone

Sub report 4 – Cross-shore transport modelling with GAIA: Ostend model

Kolokythas, G.; Breugem, A.; De Maerschalck, B.

Flanders Hydraulics

Flanders
State of the Art

Cover figure © The Government of Flanders, Department of Mobility and Public Works, Flanders Hydraulics

Legal notice

Flanders Hydraulics is of the opinion that the information and positions in this report are substantiated by the available data and knowledge at the time of writing.
The positions taken in this report are those of Flanders Hydraulics and do not reflect necessarily the opinion of the Government of Flanders or any of its institutions.
Flanders Hydraulics nor any person or company acting on behalf of Flanders Hydraulics is responsible for any loss or damage arising from the use of the information in this report.

Copyright and citation

© The Government of Flanders, Department of Mobility and Public Works, Flanders Hydraulics 2024
D/2024/3241/102

This publication should be cited as follows:

Kolokythas, G.; Breugem, A.; De Maerschalck, B. (2024). Morphodynamic modelling of the Belgian Coastal zone: Sub report 4 – Cross-shore transport modelling with GAIA: Ostend model. Version 4.0. FH Reports, 21_104_4. Flanders Hydraulics: Antwerp

Reproduction of and reference to this publication is authorised provided the source is acknowledged correctly.

Document identification

Customer:	Flanders Hydraulics	Ref.:	WL2024R21_104_4
Keywords (3-5):	Coastal modelling, sediment transport, Cross-shore sediment transport		
Knowledge domains:	Hydraulics and sediment > Hydrodynamics > Waves > Numerical modelling Hydraulics and sediment > Hydrodynamics > Tides > Numerical modelling Hydraulics and sediment > Sediment > Sediment transport > Numerical modelling		
Text (p.):	69	Appendices (p.):	/
Confidential:	☒ No	☒ Available online	

Author(s):	Kolokythas, G.

Control

	Name	Signature
Reviser(s):	Breugem, A.	Getekend door:Willem Breugem (Signatu Getekend op:2024-12-17 10:19:24 +01:0 Reden:Ik keur dit document goed Breugem Alexander Vlaamse overheid
Project leader:	De Maerschalck, B.	Getekend door:Bart De Maerschalck (Sig Getekend op:2024-09-17 17:10:54 +02:0 Reden:Ik keur dit document goed De Maerschalck Bart Vlaamse overheid

Approval

Head of Division:	Bellafkih, K.	Getekend door:Abdelkarim Bellafkih (Sig Getekend op:2024-09-17 16:00:24 +02:0 Reden:Ik keur dit document goed Bellafkih Abdelkarim Vlaamse overheid

Abstract

The presented report gives an comprehensive overview of the implementation of different cross-shore processes in GAIA, the sediment transport and bed-update module of the TELEMAC-MASCARET software suit:

- Surface roller energy generated in the breaking wave front
- Return flow generated to counterbalance the so-called Stokes drift
- Wave non-linearity, i.e. wave skewness and wave asymmetry
- Wave breaking turbulence generated in the collapsing wave front

In order to test the implementation of these cross-shore processes, a 2D-morphodynamic model for the central part of the Belgian coast, the so-called Ostend model, is build. The modelling strategy involves online coupling of the TELEMAC-2D, TOMAWAC and GAIA modules using the TEL2TOM and the implementation of Neumann conditions at the lateral boundaries of the hydrodynamic model. The model is driven by measured water levels and wind- and wave-forcing, and is validated by water level and near-shore current and wave measurements. The model is used for testing various calibration parameters for the cross-shore sediment transport modelling and finally validated against measured bed changes over the period 2016-2017.

In general the results of Ostend model with cross-shore current included, show good agreement to the measured profiles. The results show that the implementation of the cross-shore processes are an added value in the modelling of the near- and onshore bed evolution.

Contents

Abstract III
Contents IV
List of tables VI
List of figures VII
1 Introduction 1
2 Model set-up 2
2.1 Outline of the computational domains 2
2.2 Grid configuration 3
2.3 Bathymetry 5
2.4 Forcing of the model & Boundary conditions 7
2.4.1 Offshore boundary conditions 7
2.4.2 Lateral boundary conditions 8
2.4.3 Wind forcing 8
2.5 Computational time & Scalability 8
2.6 Preliminary sensitivity tests 9
2.6.1 TOMAWAC time-step & Number of breaking time-steps 9
2.6.2 Depth-induced breaking dissipation formula 13
3 Hydrodynamic & wave validation 15
3.1 Measurement data 15
3.2 Simulation period 18
3.3 Model settings 18
3.4 Hydrodynamics 20
3.4.1 Water level 20
3.4.2 Currents 20
3.5 Waves 24
4 Morphodynamic modelling 27
4.1 Theoretical background 27
4.1.1 Advection-diffusion equation 27
4.1.2 Stokes drift – Return flow 27
4.1.3 Wave non-linearity 28
4.1.4 Surface rollers 28
4.1.5 Wave breaking turbulence 29

4.2 Modification of the fortran files 29
4.3 Sensitivity tests 31
4.3.1 Bed evolution filtering 31
4.3.2 Concentration ratio R_{cs} 37
4.3.3 Wave asymmetry & skewness 41
4.3.4 Bed slope effect 45
4.3.5 Soulsby-van Rijn sediment transport formula magnitude 47
4.3.6 Return flow (Stokes drift) magnitude 49
4.3.7 Advection scheme for suspended sediment 53
4.3.8 Coupling period for TELEMAC-TOMAWAC 54
4.4 Morphological validation 54
4.4.1 Simulation period 54
4.4.2 Measurement data 54
4.4.3 Model settings 57
4.4.4 Results 58
5 Conclusions 67
References 68

List of tables

Table 1: Parallel performance metrics of the Ostend model considering coupled wave-current simulations. 8

Table 2: TOMAWAC time-step & Number of breaking time-steps test runs. 9

Table 3: TOMAWAC time-step & Number of breaking time-steps test runs. 13

Table 4: Measurement stations from the Meetnet Vlaamse banken network utilized for the validation of Ostend model. 16

Table 5: Measurement frames deployed in September 2015 at the nearshore area of Mariakerke 16

Table 6: Basic settings of the Hydrodynamic module. 19

Table 7: Basic settings of the Wave module.. 19

Table 8: Calibration parameters of the high-order filter implemented for bed evolution. 33

Table 9: Sensitivity tests for concentration ratio R_{cs} coupled with different bed filtering settings. 37

Table 10: Sensitivity tests for calibration factors f_{As} and f_{Sk} of wave assymetry and skewness. 42

Table 11: Sensitivity tests for calibration parameter CP_1 of Stokes velocity (U_{ST}). 50

Table 12: Additional settings of the Hydrodynamic & Wave modules for morphological simulations. 57

Table 13: Basic settings of the Morphology module (GAIA). 58

Table 14: Morphological simulations for the evaluation of Ostend model. 58

List of figures

Figure 1: Outlines of the TELEMAC and the TOMAWAC computational domains at the area of Ostend (Coordinate system: RD Paris). 2

Figure 2: TELEMAC-GAIA computational grid (top figure) and TOMAWAC grid (bottom figure) [Coordinate system: RD Paris]. 4

Figure 3: Element size and grid adaptation in the vicinity of port of Ostend. Top figure: TELEMAC-GAIA grid with the non-erodible elements coloured blue; Bottom figure: TOMAWAC grid at the same area. 5

Figure 4: Polygons of the updated bathymetric data for the TELEMAC model domain for the year 2015. Pink polygon: Lidar data from 10/2015; Orange polygon: Multibeam data from 07-10/2015; Yellow polygon: Compilation of port data from 2015. 6

Figure 5: Polygons of the updated bathymetric data for the TELEMAC model domain for the year 2016. Brown polygon: Lidar data from 04/2016; Red polygon: Single-beam data from 09/2016. 7

Figure 6: Efficiency versus the number of cores utilized for the parallel test runs. 9

Figure 7: Significant wave height (H_{mo}) distribution for the reference run mcs000B1 (above) and the run with increased Number of breaking time-steps (x4) mcs000B16 (bottom). 10

Figure 8: Significant wave height (H_{mo}) distribution for the run with increased time-step (20s) mcs000B11 (above) and the run with increased time-step and Number of breaking time-steps (x4) mcs000B13 (bottom). 11

Figure 9: Significant wave height (H_{mo}) distribution along the two transects perpendicular to the shoreline (see Figure 10) for four test runs included in Table 2. Top figure: Transect CS1; Bottom figure: Transect CS2. 12

Figure 10: Locations of the perpendicular to the shoreline transects utilized for wave height comparisons. 13

Figure 11: Significant wave height (H_{mo}) distribution along the two transects perpendicular to the shoreline (see Figure 10) for the default Battjes & Janssen breaking formula (blue) and the updated one (black). Top: Transect CS1; Bottom: Transect CS2. 14

Figure 12: Measurement stations utilized for the forcing and the hydrodynamic-wave validation of Ostend model. 15

Figure 13: Wind speed & direction measured at Ostend station (OS7) utilized for the forcing of the model. 17

Figure 14: Nearshore measurement stations including the locations of the measurement frames (Hercules & Hylas I) from the campaign of September 2015 within WL project 00_128. 18

Figure 15: Measured water level variation at Ostend harbor versus the numerically predicted one for the entire validation period. 20

Figure 16: Eastward U and northward V velocity components at measuring station Hercules (deployed at depth -6.5 m TAW) against the numerical results. 21

Figure 17: Eastward U and northward V velocity components at measuring station Hylas I (deployed at depth -3.5 m TAW) against the numerical results. 22

Figure 18: Velocity magnitude and direction at measuring station Hercules (deployed at depth -6.5 m TAW) against the numerical results. 23

Figure 19: Velocity magnitude and direction at measuring station Hylas I (deployed at depth -3.5 m TAW) against the numerical results. 24

Figure 20: Significant wave height (numerical & measured) at the offshore station (OPO) and at two nearshore stations (RAV, OST). 25

Figure 21: Peak wave period measured at the offshore boundary (OPO) and at a nearshore station (RAV) against numerical results. 26

Figure 22: Wave direction measured at the offshore boundary (OPO) and at a nearshore station (RAV) against numerical results. 26

Figure 23: Bed level change [m] at the end of the simulation period (8 months) with cross-shore processes activated. 32

Figure 24: Bed level change [m] at the end of the simulation period (8 months) with cross-shore processes deactivated. 32

Figure 25: Bed level change [m] at the end of the simulation period (80 days) for the run without bed filtering. 34

Figure 26: Bed level change [m] at the end of the simulation period (80 days) for three different high-order filter settings. 35

Figure 27: Location of the transects for bed profile extraction. 36

Figure 28: Bed level change [m] at Transect 6 during simulation without filtering and for three different high-order filter settings. 36

Figure 29: Bed level change [m] at Transect 2 during simulation without filtering and for three different high-order filter settings. 37

Figure 30: Bed level change [m] at the end of the simulation period (80 days) for the run with concentration ratio R_{cs} = 1. 38

Figure 31: Bed level change [m] at the end of the simulation period (80 days) for the run with concentration ratio R_{cs} = 10. 38

Figure 32: Bed level change [m] at the end of the simulation period (80 days) for the run with varying concentration ratio ($R_{cs,max}$ = 10). 39

Figure 33: Bed level change [m] at Transect 2 (Mariakerke) during simulations with 1st order filter (top) and 2nd order filter (bottom) with varying concentration ratio ($R_{cs,max}$ = 10). 40

Figure 34: Bed level change [m] at Transect 6 (Stroombank) during simulations with 1st order filter (top) and 2nd order filter (bottom) with varying concentration ratio ($R_{cs,max}$ = 10). 41

Figure 35: Bed level change [m] at the end of the simulation period for the f_{As} & f_{Sk} sensitivity tests mcs002I44 (reference) and mcs002I45. 43

Figure 36: Bed level change [m] at the end of the simulation period for the f_{As} & f_{Sk} sensitivity tests mcs002I49 and mcs002I50. 44

Figure 37: Bed level change [m] at the end of the simulation period for the f_{As} & f_{Sk} sensitivity test mcs002I59. 45

Figure 38: Bed level change [m] at the end of the simulation period for the f_{As} & f_{Sk} sensitivity tests mcs002I49 and mcs002I50. 46

Figure 39: Bed level change [m] at the end of the simulation period for the sensitivity test (mcs002I54) with calibration factor A_{cal} = 0.7 imposed to C_{eq}. 47

Figure 40: Bed level change [m] at Transect 2 (Mariakerke) during simulations with original SVR formula (top) and calibrated SVR formula (bottom) for C_{eq} calculation. 48

Figure 41: Bed level change [m] at Transect 6 (Stroombank) during simulations with original SVR formula (top) and calibrated SVR formula (bottom) for C_{eq} calculation. 49

Figure 42: Bed level change [m] at the end of the simulation period (243 days) for the reference run mcs003D without U_{ST} calibration. 50

Figure 43: Bed level change [m] at the end of the simulation period (243 days) for the run mcs003E with CP_1 = 0.5 (top) and the run mcs003E1 with CP_1 = 0.75 (bottom). 51

Figure 44: Bed level change [m] at Transect 2 (Mariakerke) during simulations without U_{ST} calibration (top), calibrated U_{ST} with CP_1 = 0.5 (middle) and calibrated U_{ST} with CP_1 = 0.75 (bottom). 52

Figure 45: Bed level change [m] at the end of the simulation period for the sensitivity test (mcs002I66) with ERIA advection scheme. 53

Figure 46: Bed level change [m] at Transect 6 (Stroombank) during simulation mcs002I66 with ERIA advection scheme. 54

Figure 47: Significant wave height, peak wave period & wave direction measured at Ostend Poortjes (OPO) utilized for the forcing of the model. 55

Figure 48: Wind speed & direction measured at Nieuwpoort station (NP7) utilized for the forcing of the model. 56

Figure 49: Measured bed level change between 2017 and 2016, at the coastal area west of Ostend harbour (Dan et al., 2023). 57

Figure 50: Measured bed level change [m] between years 2017 and 2016 interpolated on the computational grid of Ostend model. 59

Figure 51: Bed level change [m] at the end of the simulation period (243 days) for the run (mcs003R) with cross-shore current and deactivated wind-induced current. 60

Figure 52: Bed level change [m] at the end of the simulation period (243 days) for the run with cross-shore current and wind-induced current. 60

Figure 53: Bed level change [m] at the end of the simulation period (243 days) for the run without cross-shore current (wind-induced current is on). 62

Figure 54: Measured vs modelled bed level change [m] at Transect 1 (Raversijde) for the run with cross-shore current [Wind = ON] (top), and the run without cross-shore current [Wind = ON] (bottom). 63

Figure 55: Measured vs modelled bed level change [m] at Transect 2 (Mariakerke) for the run with cross-shore current [Wind = ON] (top), and the run without cross-shore current [Wind = ON] (bottom). 64

Figure 56: Measured vs modelled bed level change [m] at Transect 3 (Ostend – west dam) for the run with cross-shore current [Wind = ON] (top), and the run without cross-shore current [Wind = ON] (bottom). 65

Figure 57: Modelled bed level change [m] at Transect 5 (top) and Transect 6 (bottom) of Stroombank for the run with cross-shore current (mcs003R1) and the run without cross-shore current (mcs003Q2). 66

1 Introduction

The last years, the TELEMAC open-source platform has presented significant development in the wave-induced sediment transport modelling, thus becoming a reliable tool for short- and long-term morphological simulations at the nearshore areas. However, there is still space for further development and for incorporation of additional important mechanisms that drive sediment transport. The work presented here is an attempt to make the TELEMAC suite capable of simulating cross-shore sediment transport through the implementation of the different cross-shore processes in the GAIA and TOMAWAC modules. Namely, these are:

- Surface roller energy generated in the breaking wave front
- Return flow generated to counterbalance the so-called Stokes drift
- Wave non-linearity, i.e. wave skewness and wave asymmetry
- Wave breaking turbulence generated in the collapsing wave front

The incorporation of the aforementioned cross-shore processes in the wave and sediment transport modules of TELEMAC, has already been evaluated through the reproduction of the results of a large scale laboratory experiment for cross-shore transport over a sandy barred bed, the so-called 'CROSSTEX' experiment (Cobo et al., 2007), considering both storm (erosive) and mild (accretive) wave conditions. This validation exercise, which was presented in a previous memo (Kolokythas *et al.*, 2024), showed that the updated GAIA and TOMAWAC modules performed well in predicting the sandbar migration during erosive conditions, while for accretive conditions, the model was capable to predict partial movement of the offshore sandbar to the shallower foreshore.

Before implementing these additional processes in the full Scaldis-Coast model, it was decided to test the formulation in a smaller 2D coastal model first. In this report, the evaluation of a 2D-morphodynamic model for the central part of the Belgian coast, the so-called Ostend model, is presented. The Ostend model was constructed so that the new developments on the cross-shore transport modelling can be validated against larger scale (field) measurements under realistic forcing conditions. The modelling strategy involves online coupling of the TELEMAC-2D, TOMAWAC and GAIA modules using the TEL2TOM functionality (Breugem et al., 2019) and the implementation of Neumann conditions at the lateral boundaries of the hydrodynamic model (Breugem et al., 2018). First, the validation of the hydrodynamic and the wave modules against tidal current and wave measurements at the nearshore, takes place. Then the results are presented of the morphological simulations, performed in order to evaluate the updated GAIA module in predicting bottom changes in the surf zone in the time-scale of one year.

2 Model set-up

The Ostend model presented in this memo, was constructed so that the new developments on the cross-shore transport modelling can be validated against field measurements under realistic (measured) forcing conditions. The modelling strategy involves online coupling of the TELEMAC-2D, TOMAWAC and GAIA modules employing the TEL2TOM functionality (Breugem et al., 2019). By using TEL2TOM, the computational grids of TELEMAC and TOMAWAC are constructed with different extends and resolution. As presented in the following sections, the TOMAWAC grid is extended beyond the boundaries of the TELEMAC one, contributing in the proper imposition of the Neumann conditions at the lateral boundaries of TELEMAC avoiding local instabilities. As for the resolution, a relatively coarser mesh is chosen for TOMAWAC (compared to TELEMAC), reducing the computational cost without substantially affecting the simulation of wave propagation towards the coast.

2.1 Outline of the computational domains

The outlines of the computational domains of the TELEMAC and the TOMAWAC modules is shown in Figure 1. Note that the GAIA extent coincides with the TELEMAC one, and it actually determines the domain where the morphodynamic investigation of the coast takes place, being actually the main computational domain.

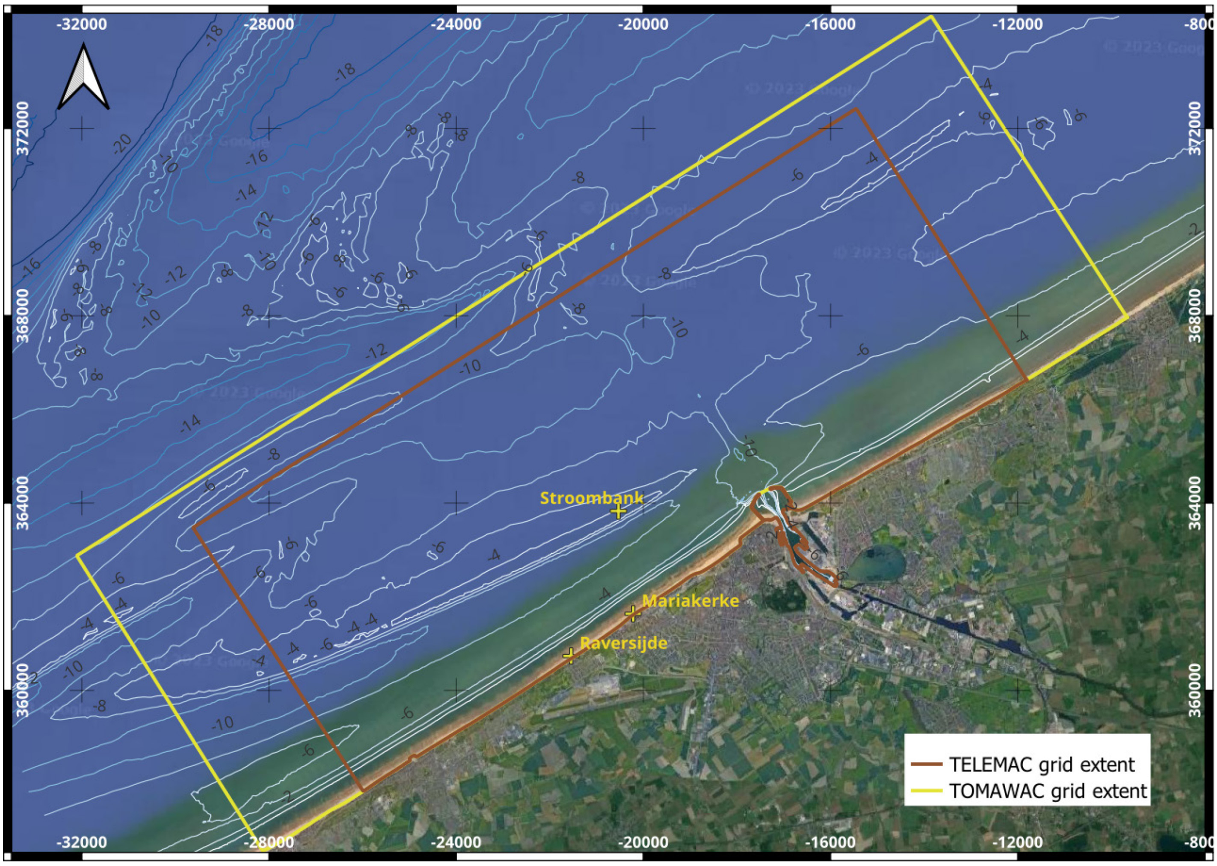

Figure 1: Outlines of the TELEMAC and the TOMAWAC computational domains at the area of Ostend (Coordinate system: RD Paris).

The dimensions of the main (TELEMAC) computational domain are 16.8 km by 6.7 km. The extent of the main computational domain was selected such that morphological changes due to cross-shore and longshore sediment transport can be investigated at the coast located west of port of Ostend (at Mariakerke and Raversijde). Furthermore, it was decided to include the port structures in the domain, taking into account its effect on the flow and the morphodynamics at the area of interest. As a result, the eastern boundary of the domain is located about 5.5 km away from the port, so that the lateral boundary effects on the hydrodynamics in the vicinity of the port are negligible. Note that, questions about the evolution of Stroombank and its interaction with the navigation channel of Ostend port could possibly be handled by this model.

The dimensions of the TOMAWAC computational domain are 21.5 km by 7.5 km. Its lateral boundaries are 2.4 km away for the corresponding ones of the TELEMAC domain, while the offshore boundary is located 0.8 km further than that of the TELEMAC domain. Note that the interior of the port of Ostend is excluded from the TOMAWAC domain, as the wave processes at this location are not affecting the areas of interest.

2.2 Grid configuration

The computational grids for the hydrodynamic and the wave modules are constructed by use of the finite element grid generator GMSH (Geuzaine & Remacle, 2009), and they are shown in Figure 2.

The TELEMAC (and GAIA) computational grid consists of 33 535 nodes and 65 772 triangular elements. Generally, the minimum element size of 25 m is found nearshore along the coastline and especially at the location of the groins the size becomes less than 20 m (see Figure 3). On the other hand, the grid resolution along the offshore (open) boundary corresponds to element sizes of 250 m. The element sizes at the Stroombank range between 60 m and 100 m.

The TOMAWAC computational grid consists of 22 535 nodes and 44 785 triangular elements. The minimum element size of ~20 m at the area of the groins is also chosen for the wave calculations, while the general element size at the nearshore is now relatively larger, equal to 40 m (see Figure 3). The grid resolution along the offshore (open) boundary remains the same as the one of the TELEMAC grid (element sizes of 250 m).

It has to be noted that the adaptive grid size of the two domains of the Ostend model was selected based on the work done before for the development of the Scaldis-Coast model (Kolokythas et al., 2019).

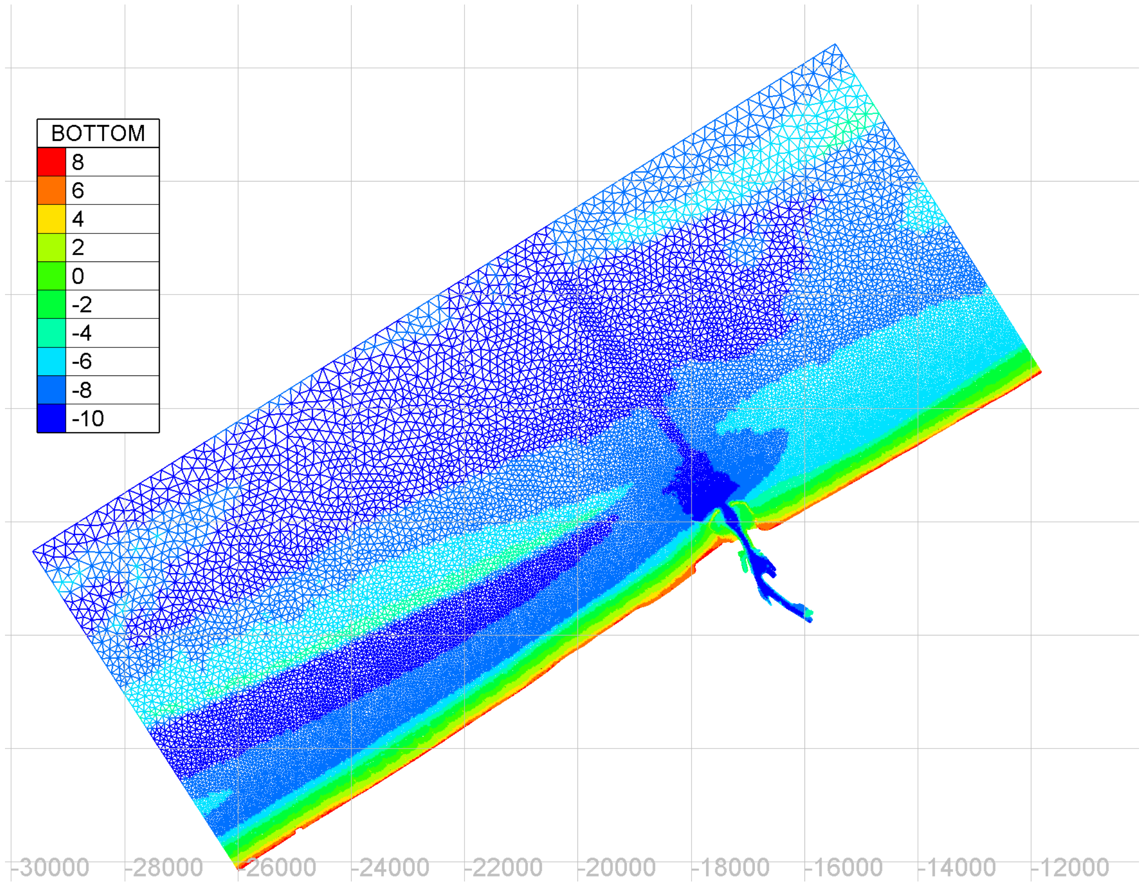

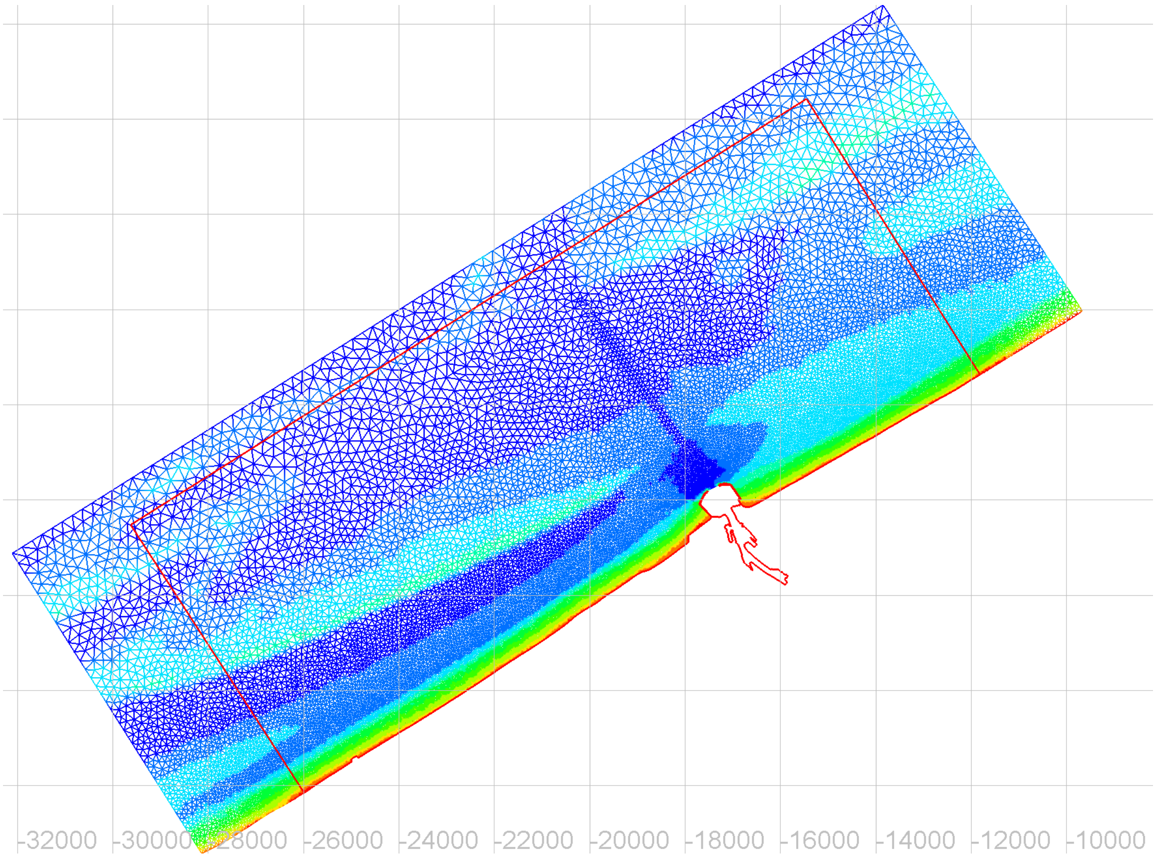

Figure 2: TELEMAC-GAIA computational grid (top figure) and TOMAWAC grid (bottom figure) [Coordinate system: RD Paris].

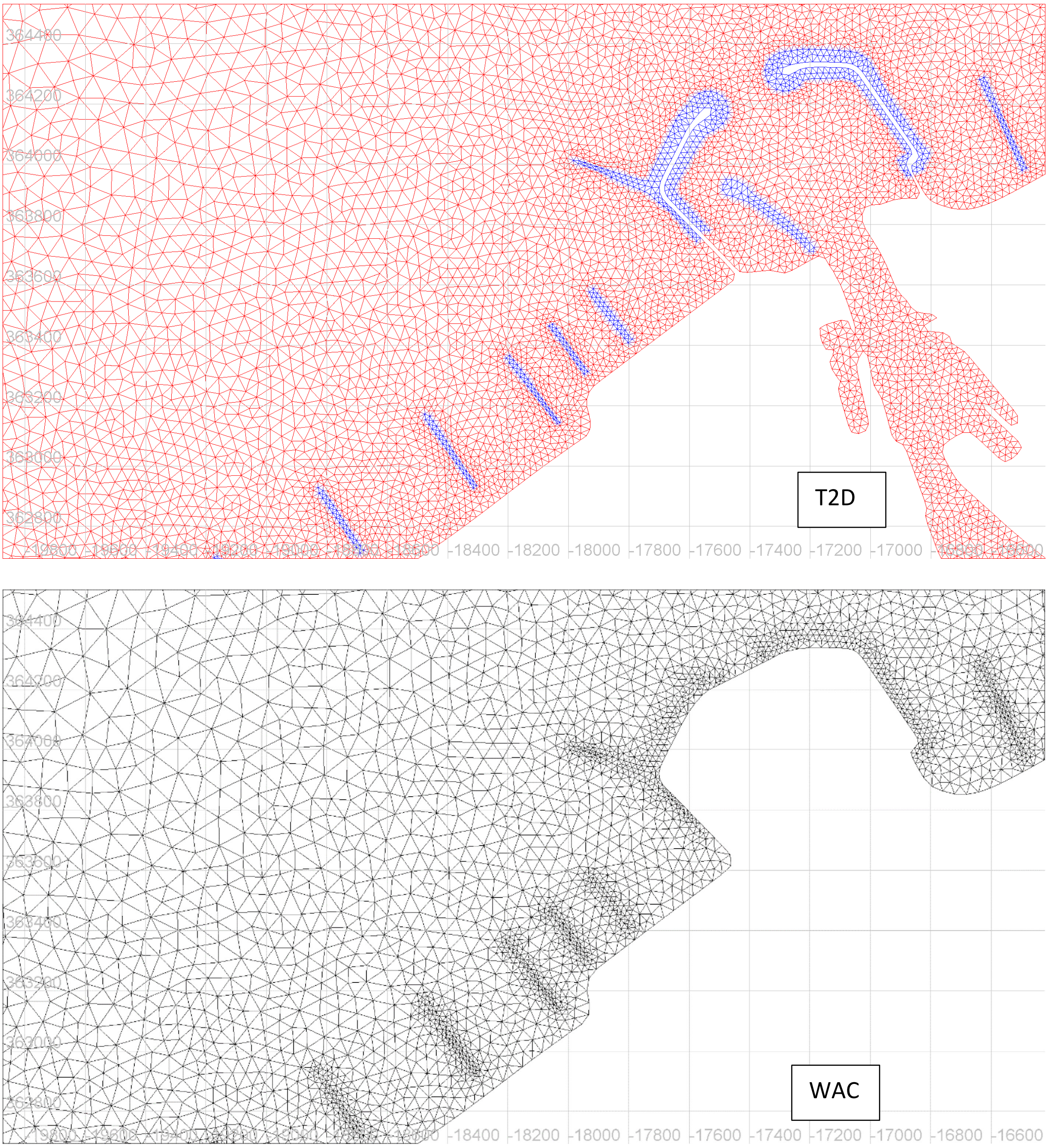

Figure 3: Element size and grid adaptation in the vicinity of port of Ostend. Top figure: TELEMAC-GAIA grid with the non-erodible elements coloured blue; Bottom figure: TOMAWAC grid at the same area.

2.3 Bathymetry

The bathymetry of the model domain results from the compilation of data from different sources.

Initially the bathymetric data from the ScaldisCoast model (Kolokythas et al., 2021) was interpolated on the computational grids of the Ostend model. The aforementioned data is a compilation of the following:

1. BCP data: Collected by different measurement campaigns of MDK from 2004 to 2016
2. Lidar data: High resolution data from 2015 that cover the beach and the intertidal areas

Next, the bathymetry was updated in the area of interest, in order to match the period of the measurement campaigns that are considered for the hydrodynamic/wave validation of the model. The update of the topographic/ bathymetric data was performed inside the (differently) coloured polygons shown in Figure 4. The topographic data of the beach and the intertidal zone at the west of Ostend port (pink polygon) come from Lidar measurements conducted in October 2015. Bathymetric data from the multibeam survey at the area of Stroombank conducted at the period July-October 2015 was also considered (orange polygon). More details about the aforementioned surveys can be found in (Dan et al., 2023). Finally, compiled bathymetric data at the area of port and along the navigational channel come from the year 2015 (15_068 project folder).

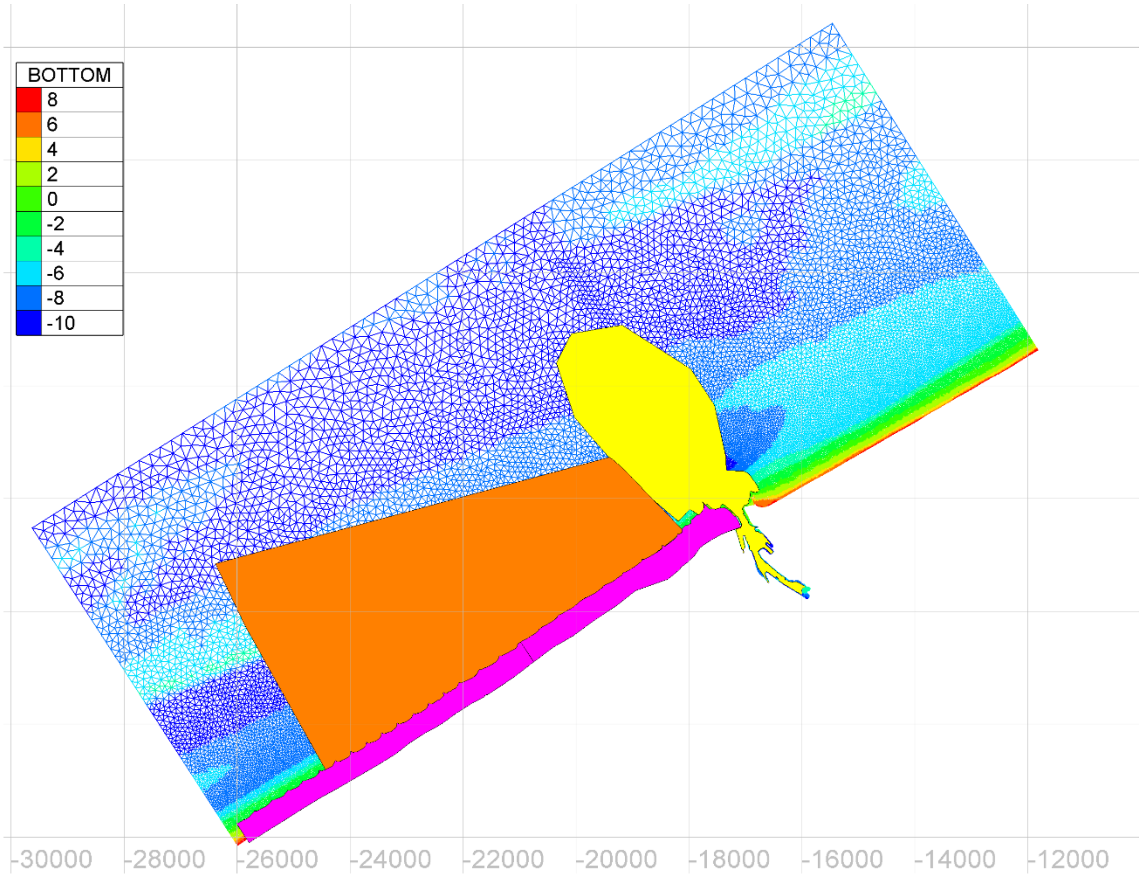

Figure 4: Polygons of the updated bathymetric data for the TELEMAC model domain for the year 2015. Pink polygon: Lidar data from 10/2015; Orange polygon: Multibeam data from 07-10/2015; Yellow polygon: Compilation of port data from 2015.

The topographic/bathymetric data at the area of interest was updated again, in order to match the selected simulation period for the morphological validation of the model. The update of the data was performed inside the coloured polygons shown in Figure 5. The topographic data of the beach and the intertidal zone at the west of Ostend port (brown polygon) come from Lidar measurements conducted in April 2016, while bathymetric data from a single-beam survey at the foreshore, conducted in September 2016 was also considered (red polygon). More details about the aforementioned surveys can be found in (Dan et al., 2023).

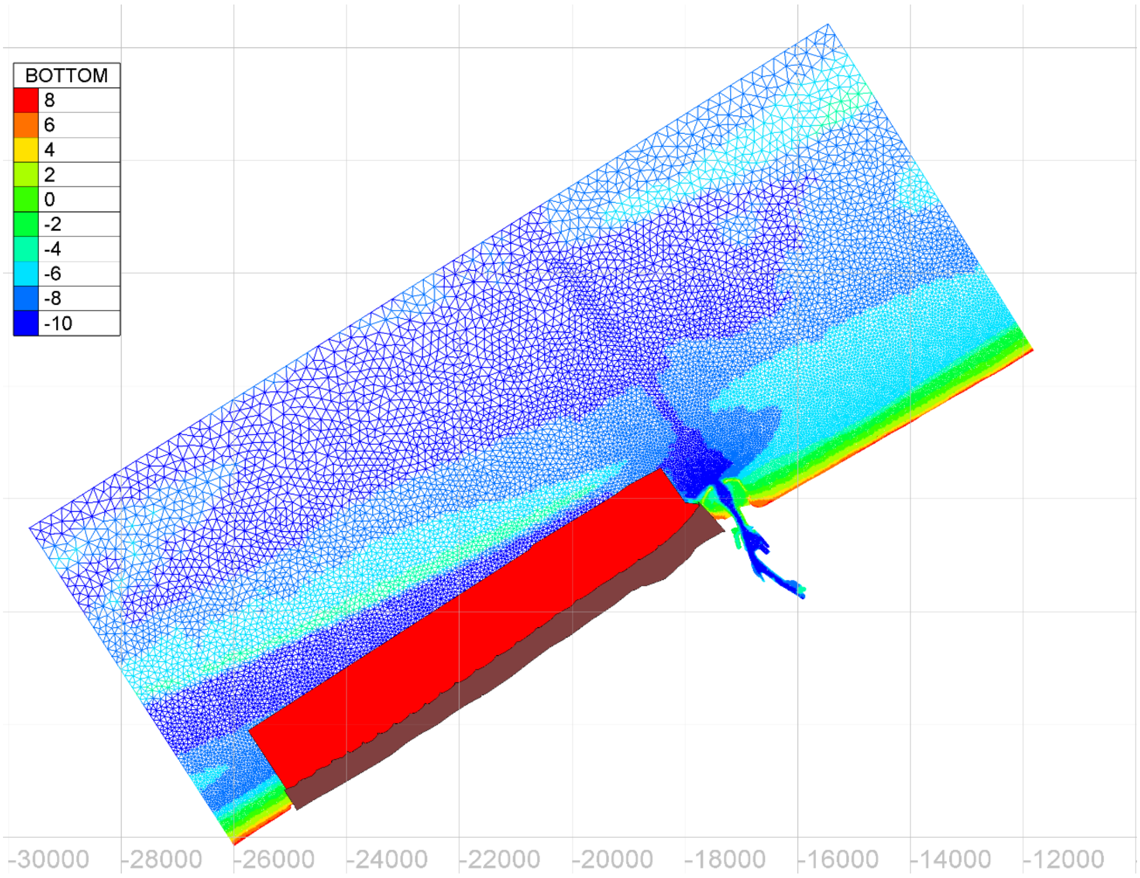

Figure 5: Polygons of the updated bathymetric data for the TELEMAC model domain for the year 2016. Brown polygon: Lidar data from 04/2016; Red polygon: Single-beam data from 09/2016.

2.4 Forcing of the model & Boundary conditions

2.4.1 Offshore boundary conditions

For the hydrodynamic forcing of the model, tidal signals from the gauges installed at Ostend (OHM) and Nieuwpoort (NPT) with a time interval of 5 min, are considered. The implementation of the tidal forcing along the offshore boundary of the model included the following:

1. The tidal signal from Nieuwpoort was applied, shifted in time, at the westmost offshore boundary node.
2. The tidal signal from Ostend was applied, shifted in time, at the eastmost offshore boundary node.
3. Linear interpolation of the two signals took place at each grid node along the offshore boundary.

It has to be noted that calibration factors had to be applied to the tidal signals of each station before interpolating along the offshore boundary, as found in the hydrodynamic validation exercise presented in the next chapter. Specifically the water level time-series of Nieuwpoort and Ostend were multiplied by 0.99 and 0.98, respectively.

As for the wave forcing of the model, time-series from the wave buoy at Ostend Poortjes (OPO), located at the offshore boundary of the TOMAWAC computational domain, are considered for the significant wave height, peak wave period and wave directions.

The locations of the aforementioned stations are depicted in Figure 12 of the next chapter, where the hydrodynamic and wave validation of the model is presented.

2.4.2 Lateral boundary conditions

For the lateral boundaries of the TELEMAC module, Neumann conditions (Breugem et al., 2018) are imposed. This means that time-series of water level gradients are prescribed perpendicular to each of the boundaries.

2.4.3 Wind forcing

Wind time series (of time-interval equal to 10 min) from Ostend (OS7) and Nieuwpoort (NP7) are imposed uniformly on the computational domain, depending on the availability of data. The locations of the aforementioned stations are depicted in Figure 12 of the next chapter. Note that wind forcing is applied only in the hydrodynamic module.

2.5 Computational time & Scalability

The scalability of the Ostend model, i.e. its ability to present substantially decreasing computational times with increasing number of utilized number of CPUs (cores), is evaluated by performing a set of coupled wave-current simulations. The simulation period is considered equal to one day and the model ran on 16, 32, 46 and 96 CPUs (cores). The computational time versus the number of utilized cores is shown in Table 1. Two metrics for the evaluation of the parallelization performance are also included in Table 1 , and they are the following:

1. Speedup index S_p, which is defined as the ratio between the computational time of the reference run and the computational time of a parallel run with multiple number of cores (n_{cpu}).
2. Efficiency, which is defined as the ratio between the Speedup and the normalized number of cores ($S_p/(n_{cpu}/n_{ref})$. Ideally it should be close to one.

The Efficiency versus the number of cores is also presented in Figure 6. It is observed that it drops abruptly for n_{cpu} = 46, while it seems to be poor when n_{cpu} = 96 (2 nodes employed). The larger wall clock time for n_{cpu} = 46 compared to that of n_{cpu} = 32, could be attributed to the differences in the partitioning of the computational domain.

Taking in to account the above, the suggested number of processors to be used for better performance of the Ostend model is 32 cores.

Table 1: Parallel performance metrics of the Ostend model considering coupled wave-current simulations.

Number of nodes	Total number of cores	Wall clock time [s]	Speedup	Efficiency
1	16	1438	1.00	1.00
1	32	787	1.83	0.91
1	46	848	1.70	0.59
2	96	755	1.90	0.32

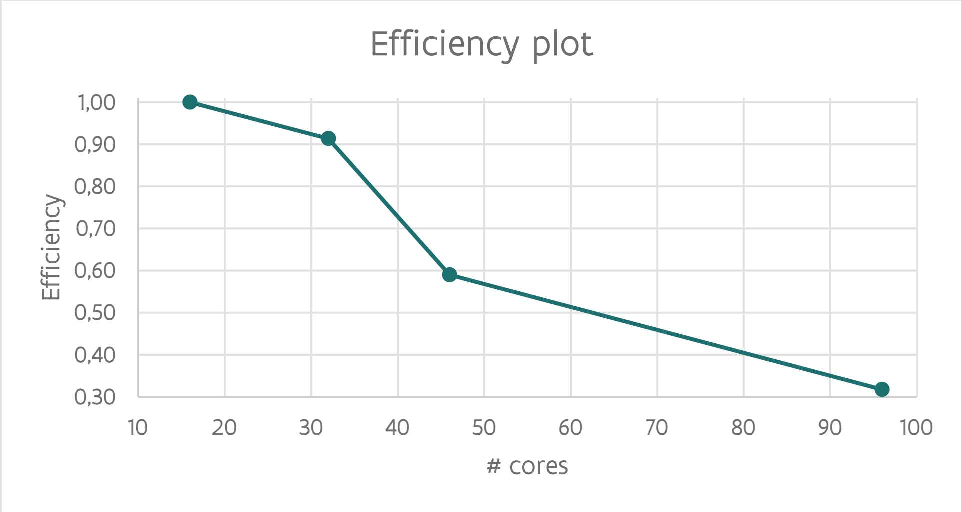

Figure 6: Efficiency versus the number of cores utilized for the parallel test runs.

2.6 Preliminary sensitivity tests

The sensitivity tests presented in this section refer to the following numerical parameters of TOMAWAC:

1. Time step (dt_{wac})
2. Number of breaking time steps (N_{dtbr})
3. Depth-induced breaking dissipation formula

2.6.1 TOMAWAC time-step & Number of breaking time-steps

The effect of the TOMAWAC time-step on the numerical results is investigated together with the Number of breaking time-steps, as they are co-related in the determination of the temporal discretization of the equations. The performed tests are presented in the table below (Table 2). Note that for the specific tests, the depth-induced breaking dissipation formula by battjes and Janssen (1978) is used.

Table 2: TOMAWAC time-step & Number of breaking time-steps test runs.

Run ID	WAC time-step [s]	No. Break time-steps	Wall clock time [s]	Wct difference [%]
mcs000B1	10	1 [default]	787	-
mcs000B15	10	2	873	11
mcs000B16	10	4	1046	33
mcs000B11	20	1	495	-37
mcs000B12	20	2	538	-32
mcs000B13	20	4	623	-21
mcs000B17	20	8	801	2

As previously, the simulation period is one day and the computational time is calculated too, as an important factor of the simulations. In the last column of Table 2, the percentage difference of computational time with respect to the reference run (mcs000B1), is shown. It is observed that doubling the time-step (mcs000B11) leads to significant reduction of the cpu time (≈37%), while increasing the Number of breaking time-steps by four (mcs000B16) results into a cpu time increase equal to 33%.

Next, the effect of the aforementioned temporal parameters on the wave propagation and transformation towards the shoreline is investigated. To this end, snapshots of the distribution of the significant wave height (H_{mo}) at the area of interest, are presented in Figure 7 and Figure 8, when the incoming wave height is H_{mo}≈2m (relatively high waves). As shown in Figure 7, the default value of Number of breaking time-steps (N_{dtbr}) leads to discontinuities in the H_{mo} distribution at the nearshore area and especially at the vicinity of the groins, which vanish when N_{dtbr} increased (by 4 times).

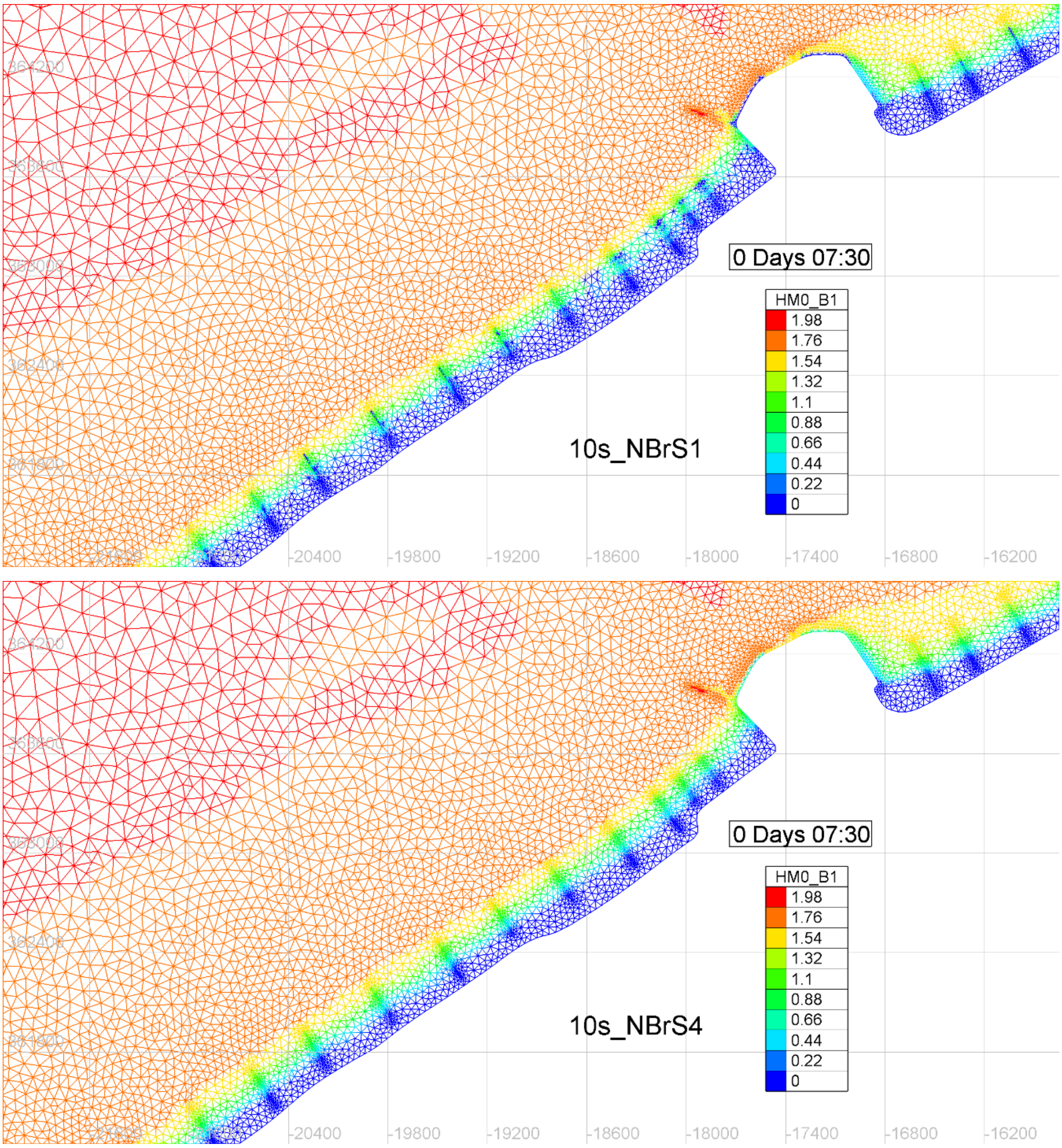

Figure 7: Significant wave height (H_{mo}) distribution for the reference run mcs000B1 (above) and the run with increased Number of breaking time-steps (x4) mcs000B16 (bottom).

In Figure 8 it is shown that the increased dt_{wac}=20s leads too poor performance of the wave model at the nearshore, as the discontinuities at the vicinity of the groins are coupled with substantially reduced wave heights. However, increasing the N_{dtbr} (by four) for the case of the increased time-step (dt_{wac}), leads to much better performance of the wave model at the nearshore. The results of the latter run (mcs000B13) are comparable to the ones of run mcs000B16 presented in Figure 7 (below), even though it seems that the wave breaking initiates relatively deeper in the case of the larger dt_{wac}. More detailed comparison of wave breaking is presented in the following paragraphs, where transects perpendicular to the shoreline, are considered. It is also worth mentioning that the results of run mcs000B17 (dt_{wac}=20s & no. breaking time-steps=8) are very similar to those of run mcs000B13.

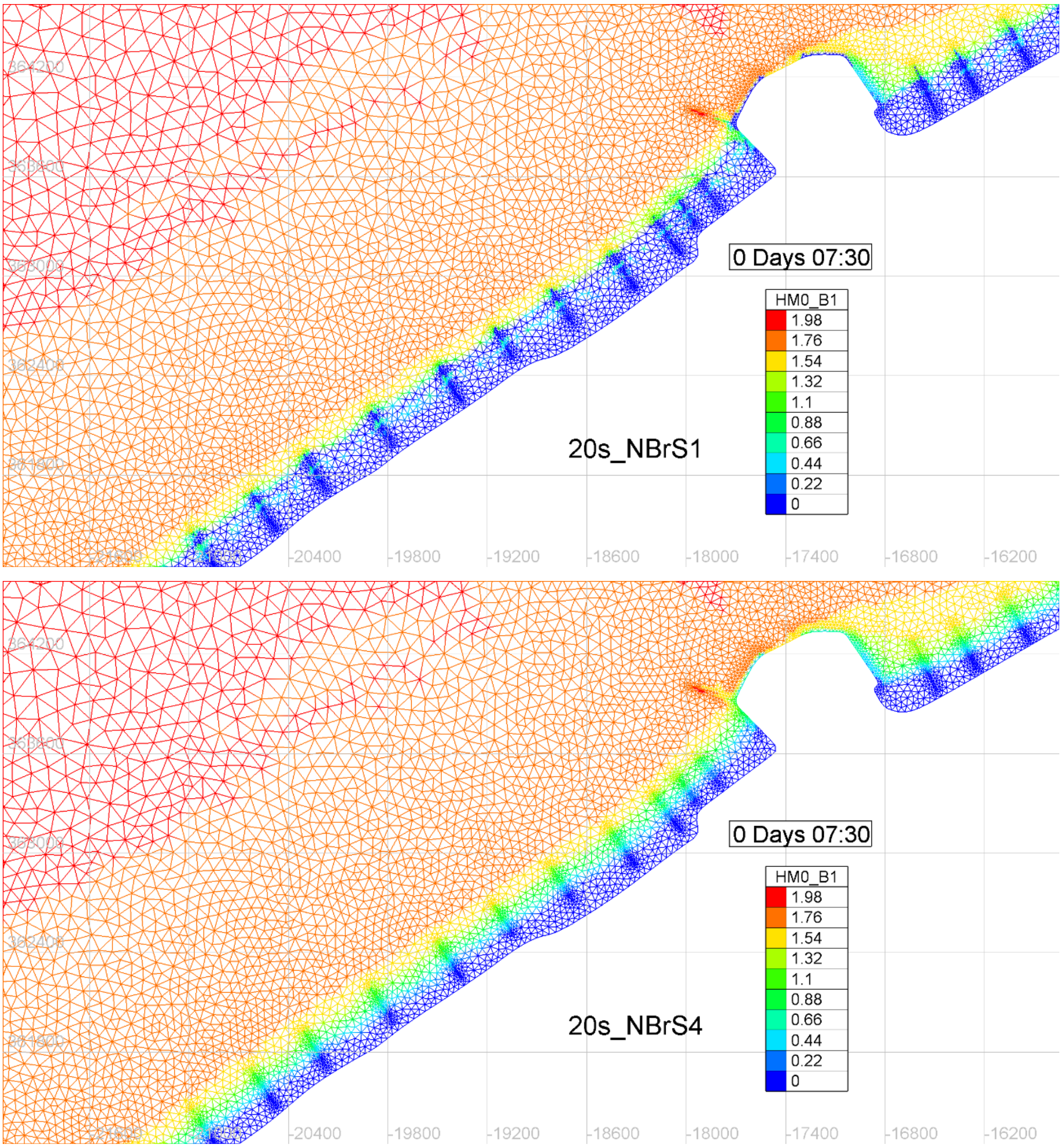

Figure 8: Significant wave height (H_{mo}) distribution for the run with increased time-step (20s) mcs000B11 (above) and the run with increased time-step and Number of breaking time-steps (x4) mcs000B13 (bottom).

In Figure 9, the instantaneous H_{mo} distribution along two transects perpendicular to the shoreline (see Figure 10) is presented, so that the effect of the temporal numerical parameters on wave breaking at the nearshore to be better examined. Note that the time instant of the presented results is the same as previously, and that one of two transects is located at an area between two successive groins (CS1), while the other one crosses (longitudinally) one of the groins at the area of interest (see Figure 10). The instabilities of the model when using the default Number of breaking time-steps (=1) are obvious at transect CS2 (red line), even if the time-step is relatively small (10 s). The behaviour of the model clearly improves with increasing N_{dtbr}, as shown in both figures (for CS1 & CS2). It is obvious that increasing N_{dtbr} moves to breaking point towards the shore. Keeping the N_{dtbr} increased (=4) and simultaneously doubling dt_{wac}, leads to deeper wave breaking, small instabilities at the breaking wavefront and relatively enhanced energy dissipation in the surf zone (black line).

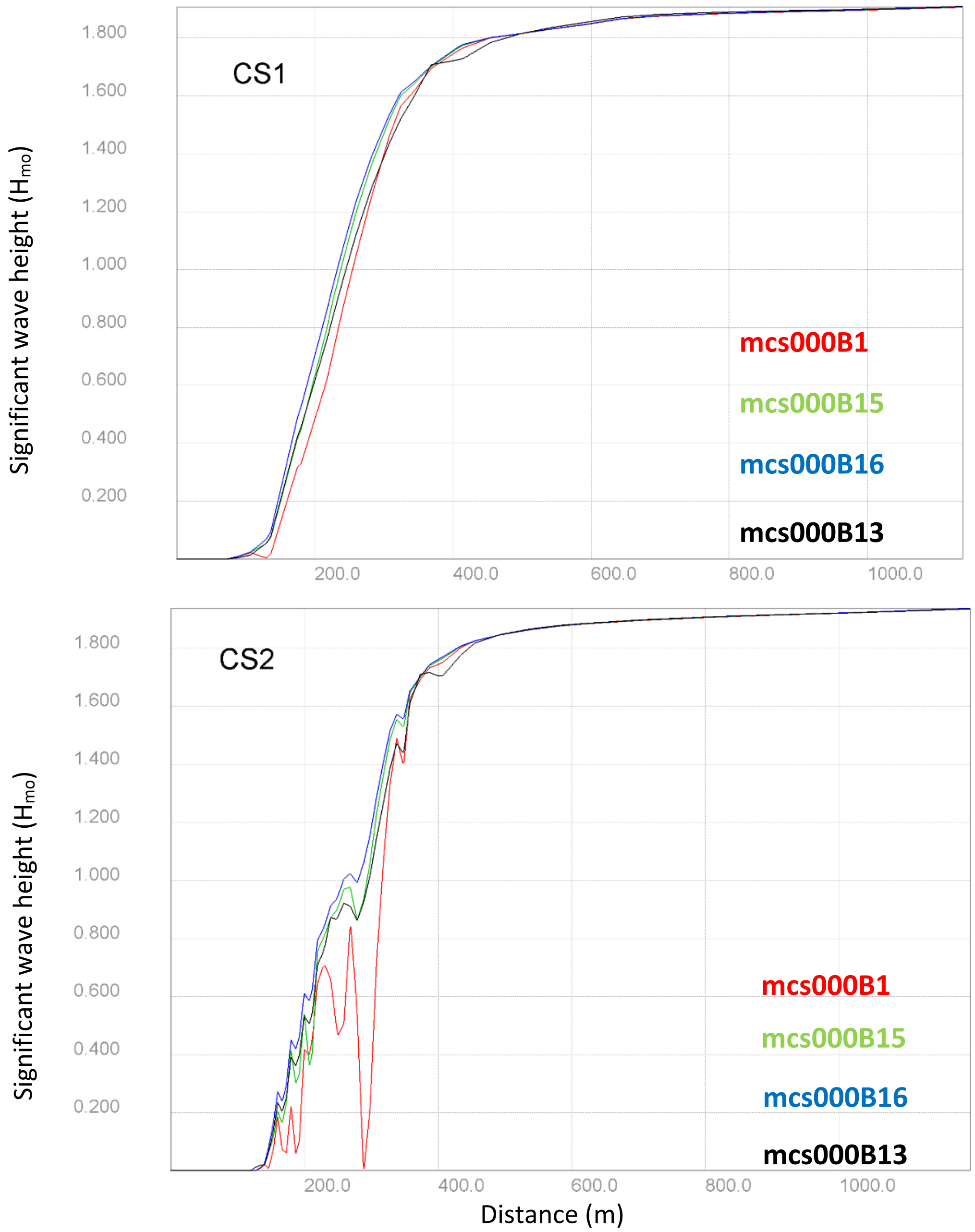

Figure 9: Significant wave height (H_{mo}) distribution along the two transects perpendicular to the shoreline (see Figure 10) for four test runs included in Table 2. Top figure: Transect CS1; Bottom figure: Transect CS2.

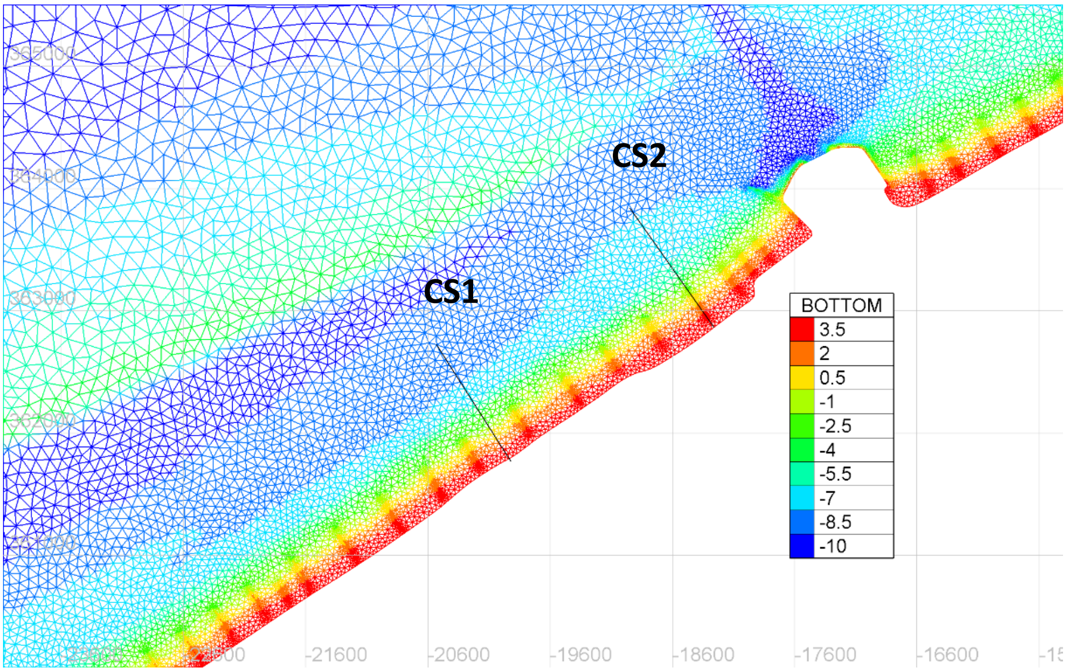

Figure 10: Locations of the perpendicular to the shoreline transects utilized for wave height comparisons.

2.6.2 Depth-induced breaking dissipation formula

The default option in TOMAWAC for the calculation of depth-induced breaking dissipation proposed by Battjes & Janssen (1978) has been proven to perform satisfactorily. In the latest versions of the code an updated, implicit version of the specific formula has been introduced, which is expected to reduce the computational time (Breugem W.A. et al., 2021). In this section, the evaluation of the updated breaking formula is presented. The performed tests are presented in the table below (Table 2).

Table 3: TOMAWAC time-step & Number of breaking time-steps test runs.

Run ID	Breaking formula	dt_{wac} [s] / N_{dtbr}	Wall clock time [s]	Wct difference [%]
mcs000B16	Battjes & Janssen [default] (1)	10 / 4	1046	-
mcs000B18	Battjes & Janssen [implicit] (10)	10 / 4	714	-32

As previously, the simulation period is one day and the computational time is calculated too, as an important factor of the simulations. In the last column of Table 2, the percentage difference of computational time with respect to the reference run (mcs000B16), is shown. It is found that the updated breaking formula (run mcs000B18) leads to significant reduction of the cpu time (32%).

Next, the effect of the updated breaking formula on the wave propagation and transformation towards the shoreline is investigated. Snapshots of the distribution of the significant wave height (H_{mo}) along the two perpendicular to the coast transects CS1 and CS2 (see Figure 10), is presented in Figure 11, when the incoming wave height is H_{mo}≈2m (relatively high waves). It is found that the two compared formulas give almost identical results for H_{mo} distribution in the surf zone, while they present an almost constant difference for larger depths than the breaking depth. For transect CS2, the updated breaking formula predicts about 5% larger H_{mo} values at deeper waters, while a smaller increase is found at CS1(about 3%). It seems that the updated formula is less dissipative (during shoaling) than the original one. This behavior though is not expected and it should be further investigated.

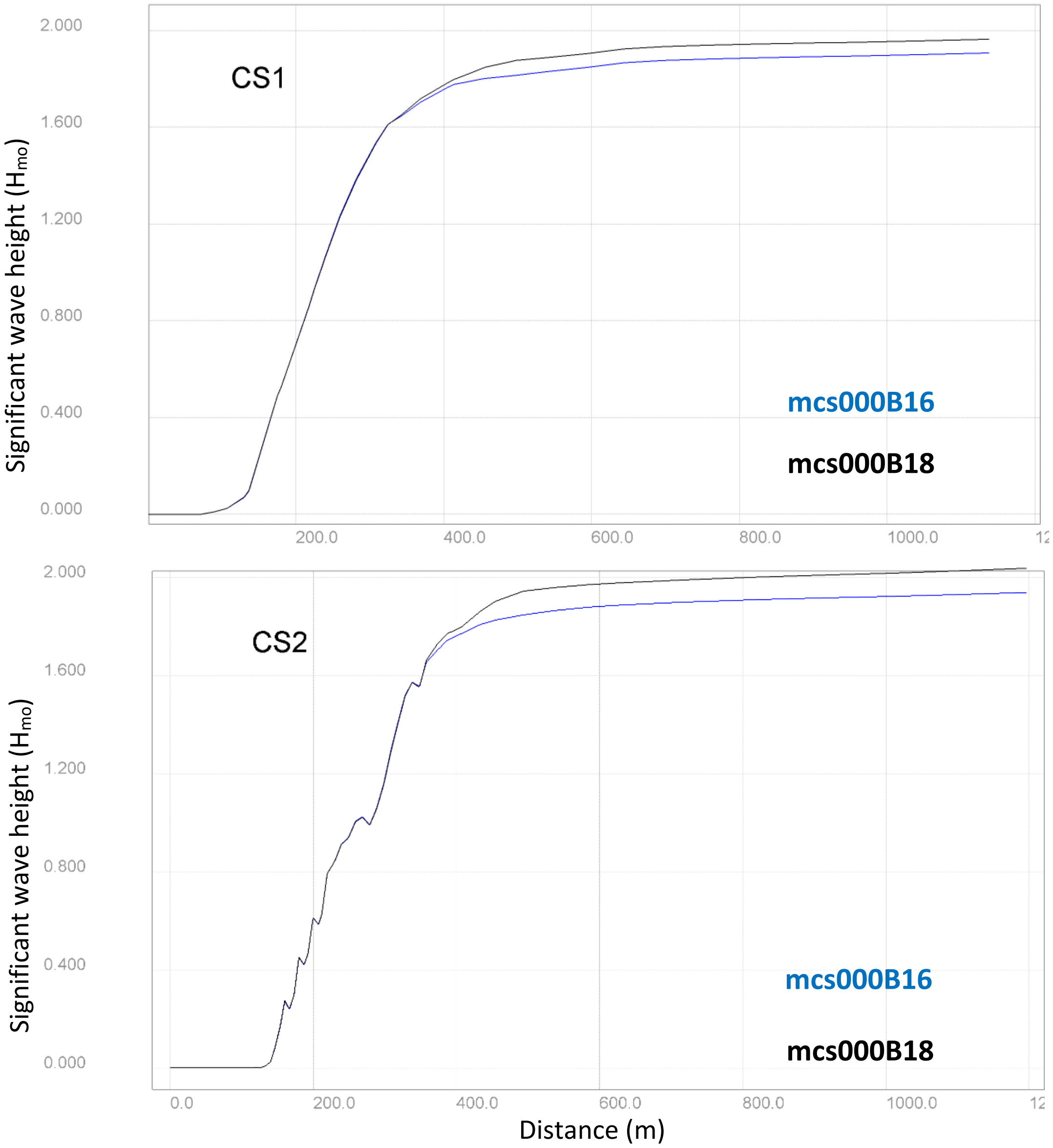

Figure 11: Significant wave height (H_{mo}) distribution along the two transects perpendicular to the shoreline (see Figure 10) for the default Battjes & Janssen breaking formula (blue) and the updated one (black). Top: Transect CS1; Bottom: Transect CS2.

3 Hydrodynamic & wave validation

3.1 Measurement data

The measurement data utilized for the tidal, wave and wind forcing but also for the hydrodynamic-wave validation of the Ostend model were mainly retrieved from the Meetnet Vlaamse Banken online database (MDK agency) and from personal communication with the Coordination team (Johan Vercruysse). The locations of the considered stations and the type of the data recordings are shown in Figure 12. More information about the stations is provided in Table 4. As mentioned in the previous chapter, measurements from Ostend and Nieuwpoort harbour stations (OHM, NPT, OS7, NP7) were considered for the tidal and wind forcing of the model, while recordings from Ostend Poortjes (OPO), were utilized for the wave forcing of the model. Data from the Ostend harbour (OHM), the Raversijde (RAV) and Ostend eastern palisade (OST) stations were considered for the water level and wave validation of the model, respectively.

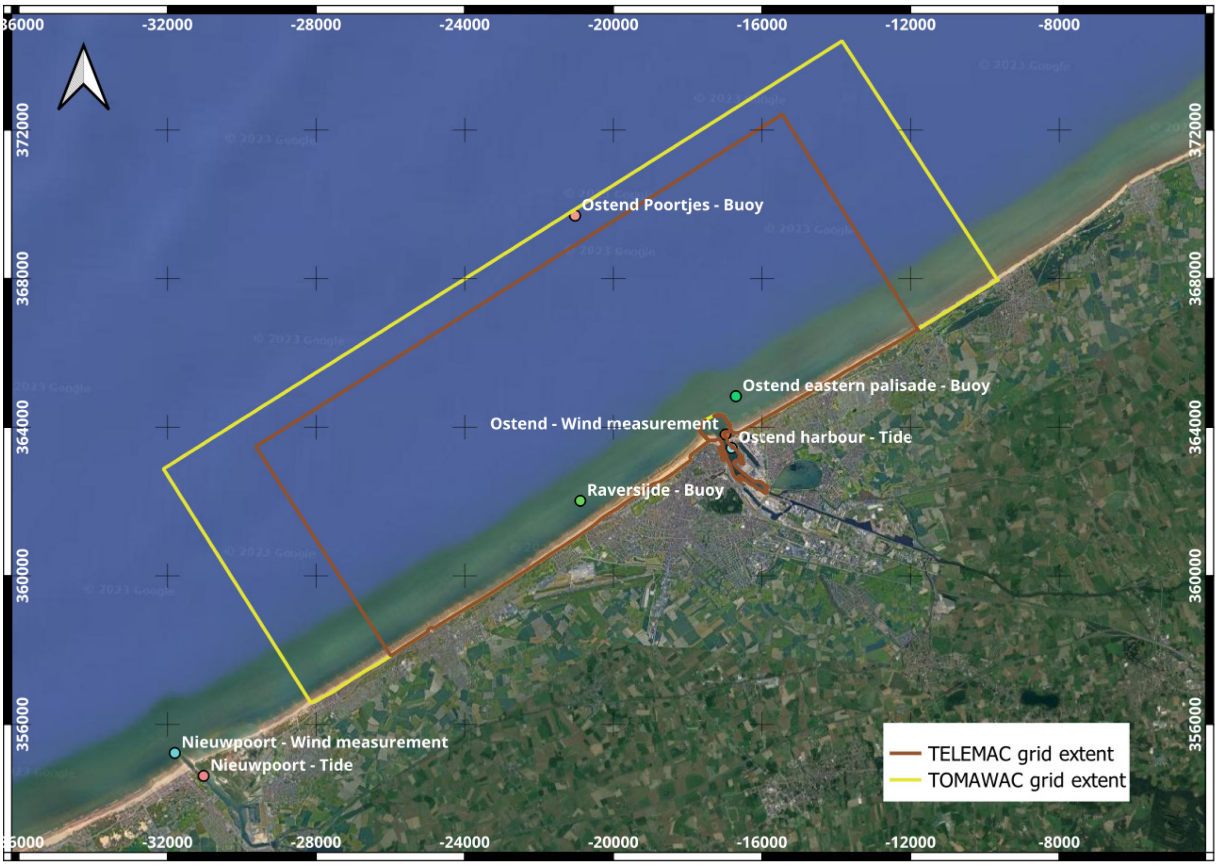

Figure 12: Measurement stations utilized for the forcing and the hydrodynamic-wave validation of Ostend model.

Table 4: Measurement stations from the Meetnet Vlaamse banken network utilized for the validation of Ostend model.

Location	ID	Measurement	Coordinates (RD-Paris)	Record. interval (min)
Nieuwpoort	NP7	Wind	X:-31806 Y: 355235	10
Nieuwpoort	NPT	Tide	X:-31030 Y: 354619	5
Ostend	OS7	Wind	X:-16988 Y: 363806	10
Ostend harbour	OHM	Tide	X:-16825 Y: 363443	5
Ostend east. palisade	OST	Waves	X:-16709 Y: 364836	30
Ostend Poortjes	OPO	Waves	X:-21036 Y: 369697	30
Raversijde	RAV	Waves	X:-20894 Y: 362022	30

For the completion of hydrodynamic validation, stationary velocity measurements at the nearshore area of Mariakerke were considered. This data comes from a measuring campaign conducted between 23/09/2015 and 14/11/2015, which, among others, involved the deployment of two measuring frames i.e. Hercules and Hylas I (Table 5). More information about the aforementioned campaign can be found in Montreuil et al. (2015). The exact location of the Hercules and Hylas I frames is shown in Figure 14. Note that he velocities were measured by means of an Acoustic Wave and Current profiler (AWAC-W) with a recording interval equal to 10 min.

Note that wind time series from Ostend (OS7) were utilized for the forcing of the hydrodynamic module, imposed uniformly on the computational domain. Wind characteristics for the simulation period are shown in Figure 13.

Table 5: Measurement frames deployed in September 2015 at the nearshore area of Mariakerke .

<table>
<tr><th colspan="2" rowspan="2">Station</th><th colspan="2">Coordinates (RD Paris)</th><th rowspan="2">Date</th><th rowspan="2">Depth
(m TAW)</th></tr>
<tr><th>X</th><th>Y</th></tr>
<tr><td rowspan="2">Hercules/M1</td><td>Deployment</td><td>-20624</td><td>362070</td><td>23/09/2015</td><td>-6.5 m</td></tr>
<tr><td>Retrieval</td><td>-20624</td><td>362070</td><td>03/12/2015</td><td>-6.5 m</td></tr>
<tr><td rowspan="2">Hylas I/M3</td><td>Deployment</td><td>-20524</td><td>361920</td><td>23/09/2015</td><td>-3.5 m</td></tr>
<tr><td>Retrieval</td><td>-20524</td><td>361920</td><td>03/12/2015</td><td>-3.5 m</td></tr>
</table>

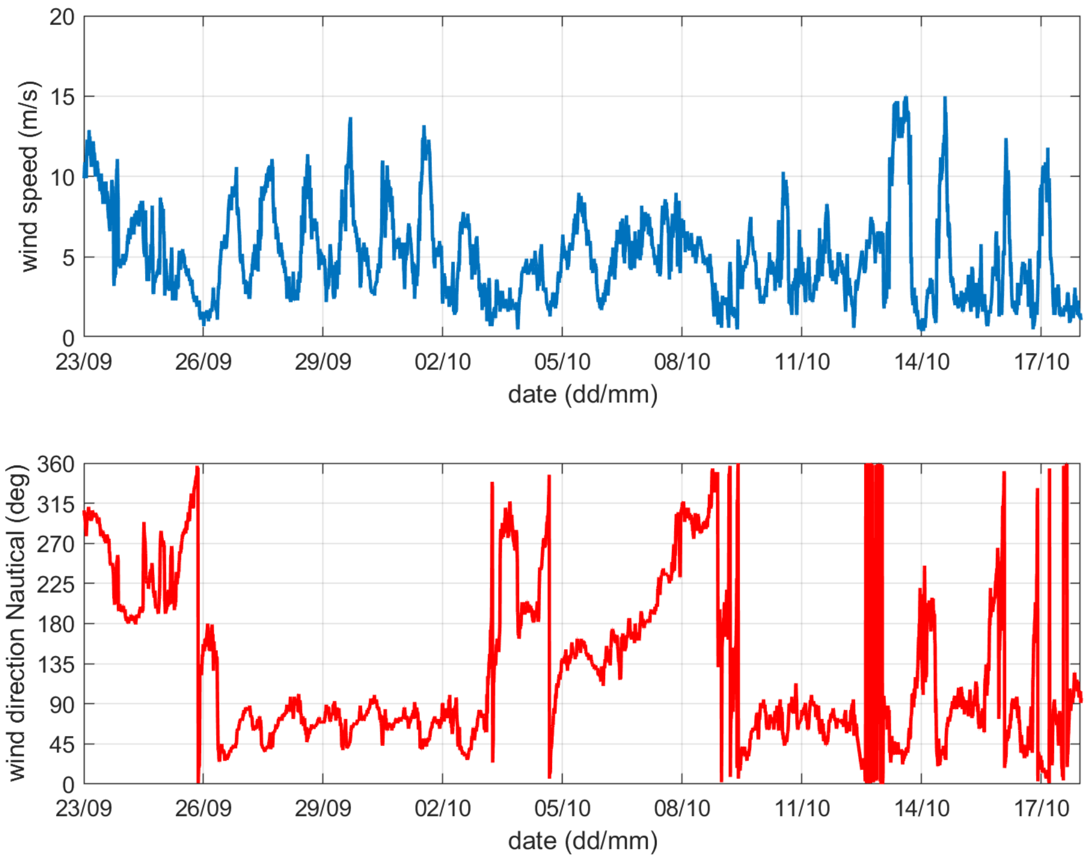

Figure 13: Wind speed & direction measured at Ostend station (OS7) utilized for the forcing of the model.

Figure 14: Nearshore measurement stations including the locations of the measurement frames (Hercules & Hylas I) from the campaign of September 2015 within WL project 00_128.

3.2 Simulation period

For the hydrodynamic-wave validation of Ostend a simulation period of 25 days in 2015 (from 23/09/2015 to 18/10/2015) was considered. The selection of the specific period is mainly based on the availability of velocity measurements from the campaign at the area of interest (Mariakerke) mentioned in the previous section. Furthermore, it was also taken into account that (at least) relatively high energetic wave events should be included in the selected simulation period.

3.3 Model settings

The basic settings of the hydrodynamic and the wave modules, which are online coupled are presented in the following tables (Table 6 and Table 7). Note that the branch ‘ScaldisCoast’ based on TELEMAC v8p4 is used for the simulations.

Table 6: Basic settings of the Hydrodynamic module.

Offshore boundary conditions	Water level interpolated from OHM and NPT gauges (MVB)
Lateral boundary conditions	Neumann type (water level gradient)
Bottom roughness	Manning (n=0.022)
Wind	ON (spatially uniform time-series from OS7)
Coefficient of wind influence varying with speed	ON (formula by Institute of Oceanographic Sciences (UK))
Wave-driven currents	ON
Coriolis	OFF
Turbulence	Smagorinsky (C_s=0.1)
Time-step	5 s
Coupling period for TOMAWAC	180 s
Scheme for advection of velocities	1: method of characteristics
Scheme for advection of depth	5: conservative scheme
SUPG OPTION	2;0
Free surface gradient compatibility	0.9
Solver	1: Conjugate gradient
Mass lumping on H	1.0
Option for the treatment of tidal flats	1: equations solved with correction on tidal flats
Treatment of negative depths	2: flux control

Table 7: Basic settings of the Wave module.

Offshore boundary conditions	H_{mo}, T_p, W_{dir} time-series from OPO buoy (MVB) / Jonswap directional spectrum (6)
Wind	OFF
Depth-induced wave breaking formula	10: implicit Battjes-Jansen
Depth-induced breaking comp. method	2
Breaking GAMMA1/GAMMA2/ALPHA	0.80/0.80/0.80
Number of breaking time-steps	4
Whitecapping/Triad interactions Non-linear transfers/Wind generation	OFF/OFF OFF/OFF
Bottom friction dissipation	1: Similar to that of WAM cycle 4
Time-step	10 s
Number of directions	36 (D_θ=10 degrees)
Number of frequencies	25 (minimal frequency = 0.052Hz)

3.4 Hydrodynamics

3.4.1 Water level

The successful imposition of the combined water level time-series, measured by the tidal gauges installed at the Ostend and Nieuwpoort harbours, for the hydrodynamic forcing of the model is (firstly) depicted in Figure 15. In this figure the numerically predicted water level variation is compared to the measured one at the Ostend harbour station (OHM). Details about the implementation of the tidal forcing have already been given in section 2.4.1.

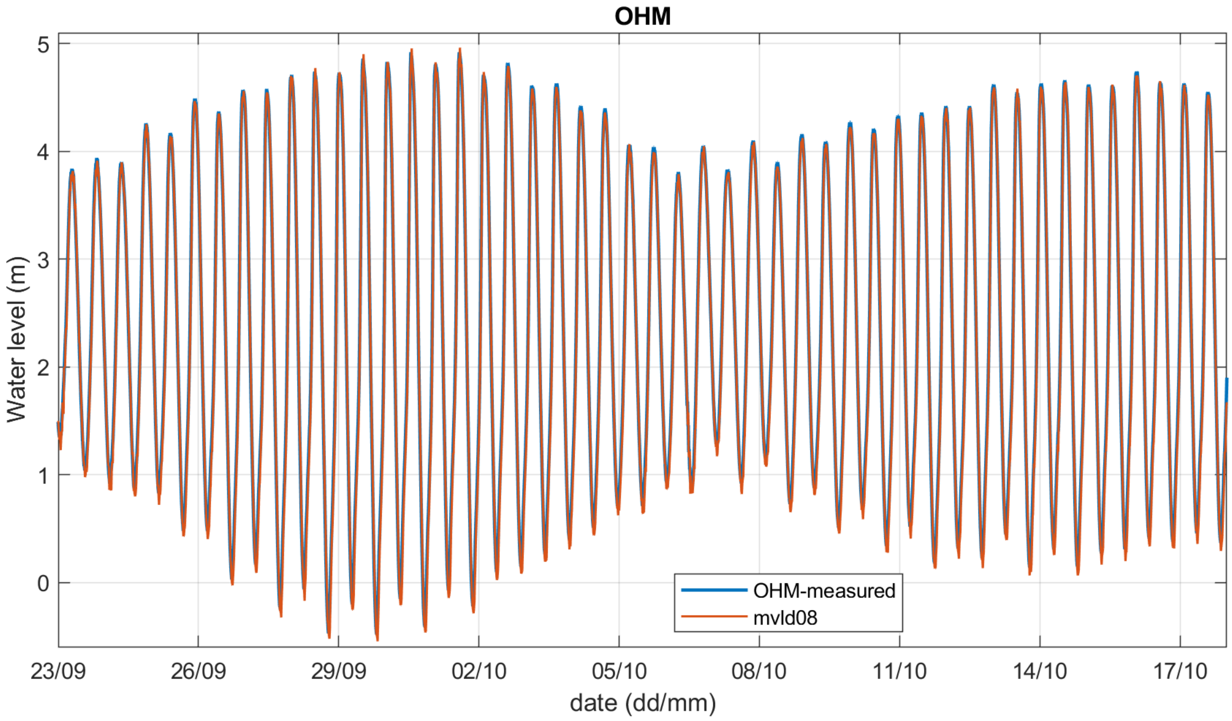

Figure 15: Measured water level variation at Ostend harbor versus the numerically predicted one for the entire validation period.

3.4.2 Currents

The performance of the model in predicting the current characteristics (magnitude and direction) at the area of interest is evaluated by comparing the corresponding numerical results against the field measurements at the two frames, Hercules and Hylas I, deployed at Mariakerke in autumn 2015. In Figure 16 and Figure 17, the comparison is expressed by means of the depth-averaged eastward U and northward V velocity components at the location of Hercules and Hylas I frames, respectively. It can be observed that a satisfactory agreement with the field measurements is achieved. The comparison of current characteristics expressed in terms of velocity magnitude and direction are given in Figure 18 and Figure 19 for Hercules and Hylas I frames, respectively. Observing the aforementioned figures, it can be concluded that the numerical predictions are in reasonable agreement with the field measurements, although the model tends to underestimate the maximum ebb velocities, especially at the shallower frame (Hylas I). The average underestimation by the numerical model for the ebb velocities, over the entire simulation period, is about 30% at Hercules frame and 40% at Hylas I frame. A limited (in time) underestimation of the maximum flood velocities is also observed at both frames during the period 27/9-02/10/2015. The maximum (absolute) difference between numerical and measured flood velocities (during this limited period) is about 10% at Hercules frame and 20% at Hylas I frame.

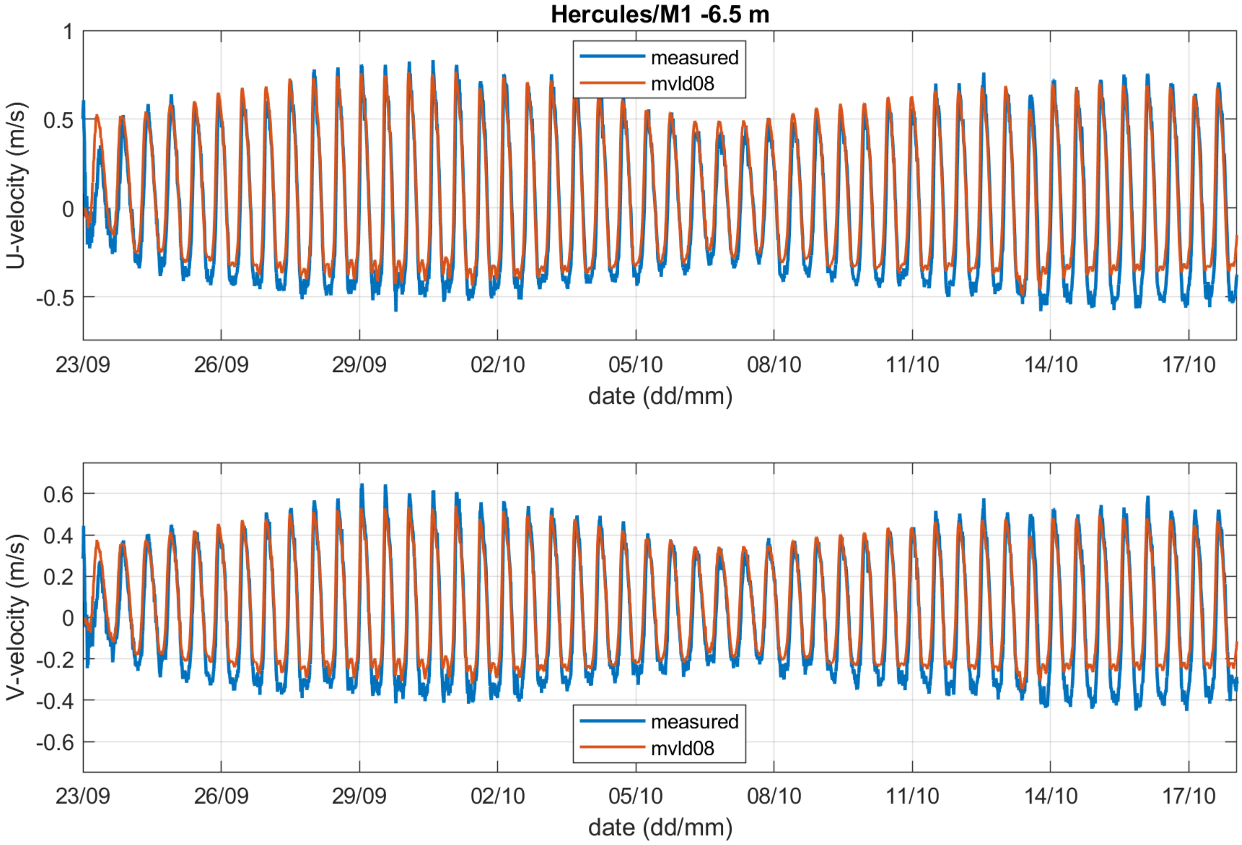

Figure 16: Eastward U and northward V velocity components at measuring station Hercules (deployed at depth -6.5 m TAW) against the numerical results.

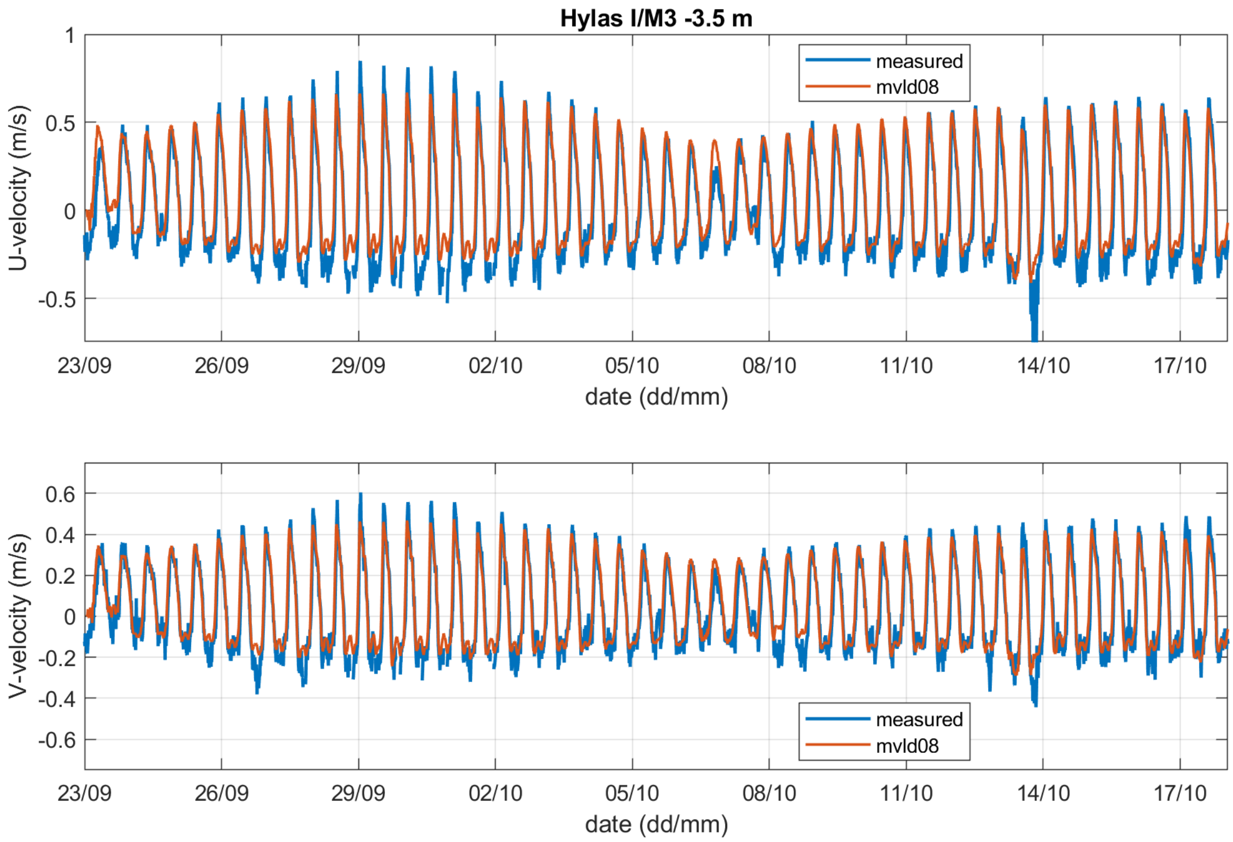

Figure 17: Eastward U and northward V velocity components at measuring station Hylas I (deployed at depth -3.5 m TAW) against the numerical results.

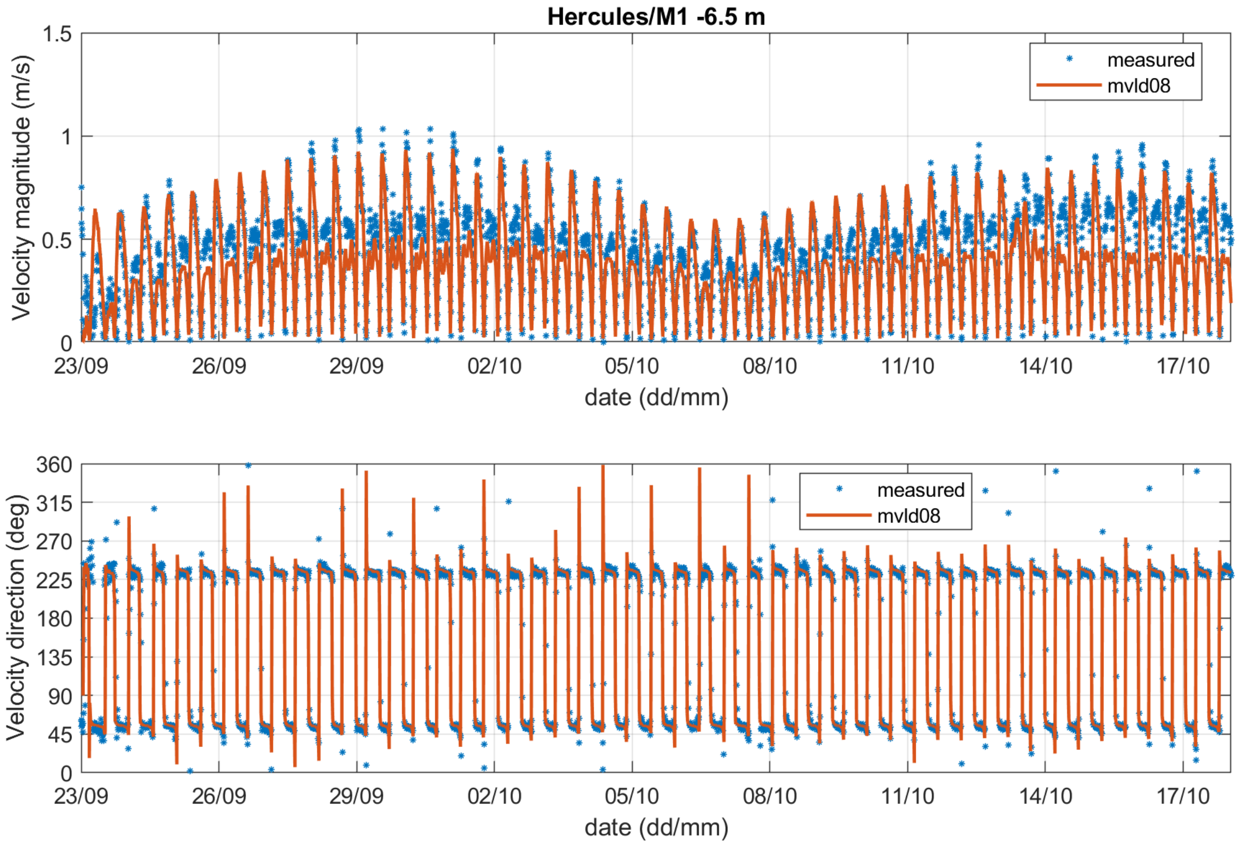

Figure 18: Velocity magnitude and direction at measuring station Hercules (deployed at depth -6.5 m TAW) against the numerical results.

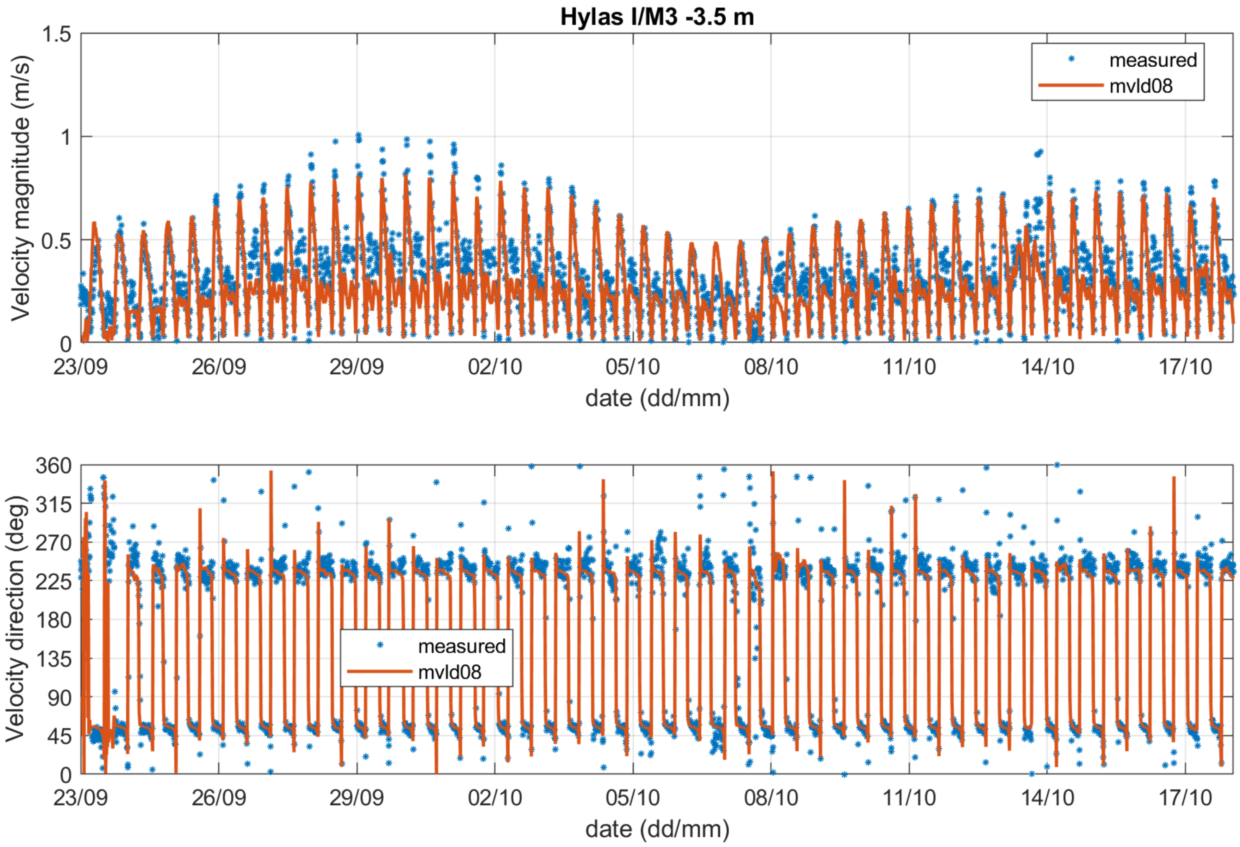

Figure 19: Velocity magnitude and direction at measuring station Hylas I (deployed at depth -3.5 m TAW) against the numerical results.

3.5 Waves

The validation of the wave module is achieved by comparing the modelled wave characteristics, i.e. significant wave height H_{mo}, peak wave period T_p and wave direction, against corresponding recordings from nearshore wave bouys at Raversijde (RAV) and Ostend eastern palisade (OST). The successful imposition of the wave parameters time-series recorded by the wave buoy at Ostend Poortjes (OPO), for the wave forcing of the model is also verified by comparing them to the numerical ones. In Figure 20, the comparison between modelled and measured H_{mo} at the three aforementioned stations, is presented. It is found that the model is capable of predicting the wave height transformation at the nearshore, as the agreement with the recordings is very good. In Figure 21 and Figure 22, the modelled and the measured peak wave period and wave direction are presented for only two stations OPO and RAV, as there was a lack of recordings at OST buoy for the specific period. The agreement at the offshore boundary location (OPO) is almost excellent (as expected), and reasonable at Raversijde. Though, a noticeable offset of the modelled wave directions from the recorded ones, of about 15-20 degrees, is observed for the period 26/09-03/10/2015 (Figure 22).

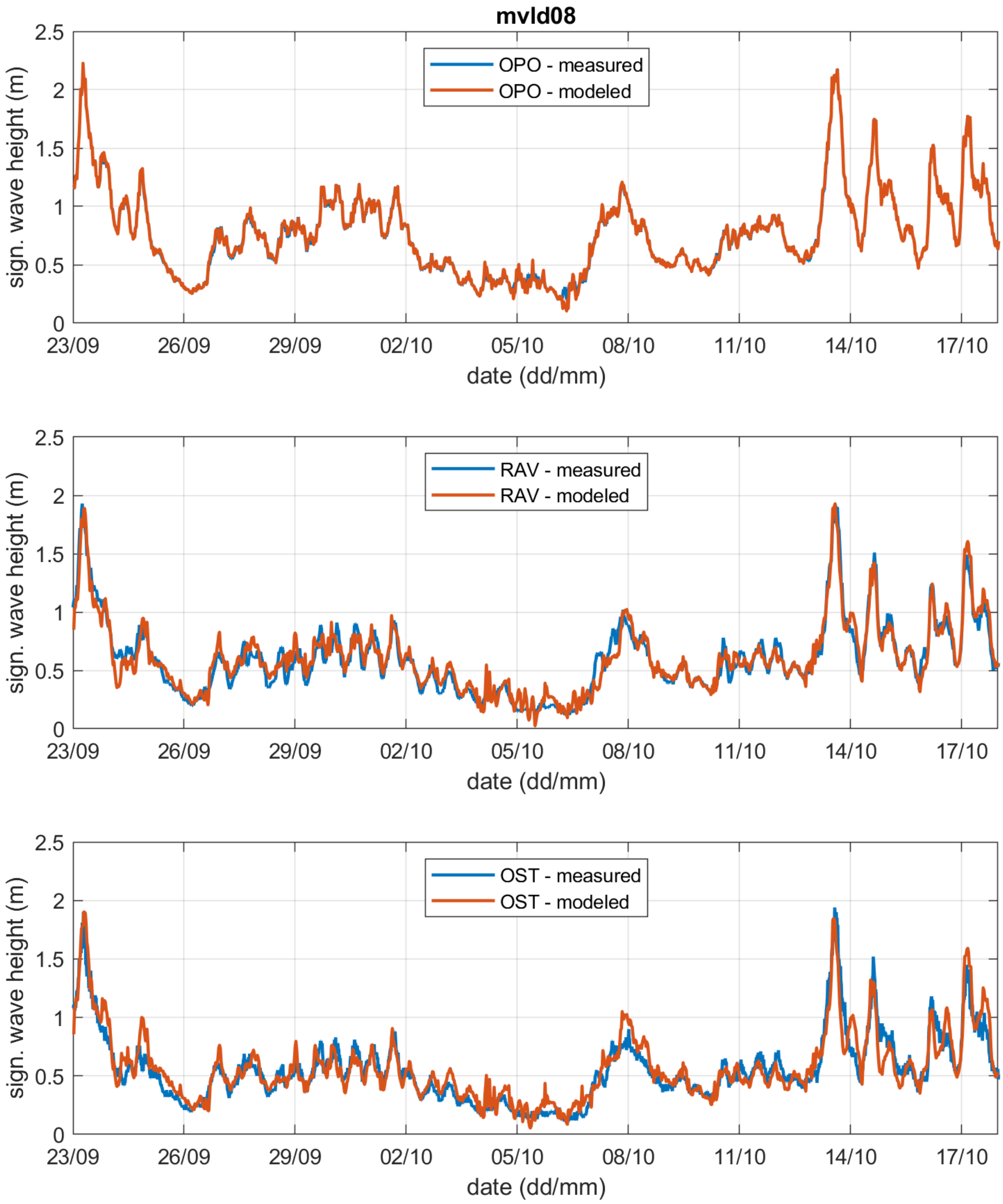

Figure 20: Significant wave height (numerical & measured) at the offshore station (OPO) and at two nearshore stations (RAV, OST).

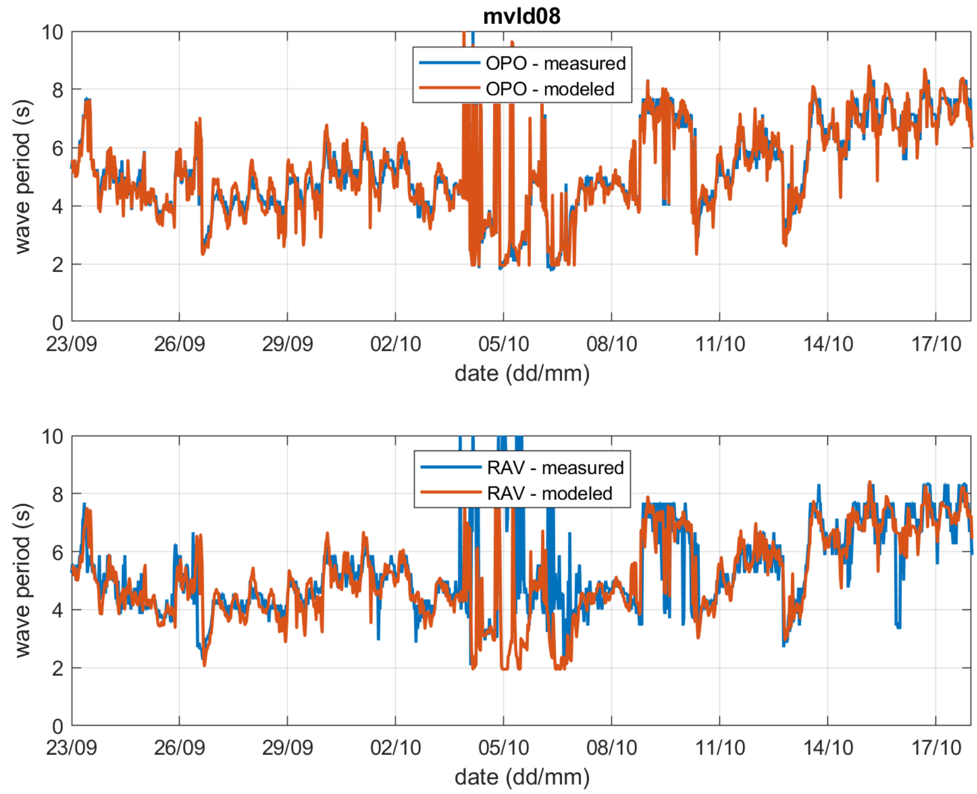

Figure 21: Peak wave period measured at the offshore boundary (OPO) and at a nearshore station (RAV) against numerical results.

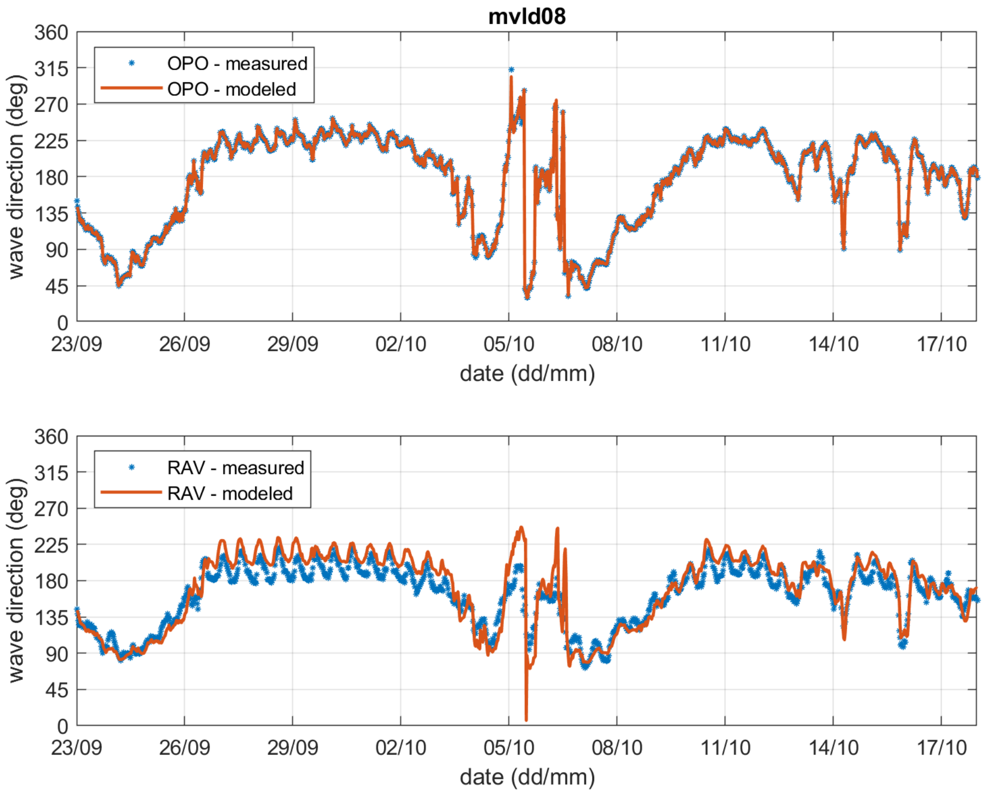

Figure 22: Wave direction measured at the offshore boundary (OPO) and at a nearshore station (RAV) against numerical results.

4 Morphodynamic modelling

4.1 Theoretical background

4.1.1 Advection-diffusion equation

The main cross-shore processes are incorporated in the sediment transport module through the mean velocities (U^E,V^E) that are introduced in the depth-averaged advection-diffusion equation for the calculation of sediment mean concentration *C* in the water column:

$$\frac{\partial hC}{\partial t}+\frac{\partial hU^E C}{\partial x}+\frac{\partial hV^E C}{\partial y}+\frac{\partial}{\partial x}\left(h\varepsilon_s\frac{\partial C}{\partial x}\right)+\frac{\partial}{\partial y}\left(h\varepsilon_s\frac{\partial C}{\partial y}\right)=w_s\left(C_{eq}-C\right)R_{cs} \quad (1)$$

where *t* is time, *x* and *y* are the two horizontal dimensions of the numerical domain, *h* is the water depth, ε_s is the eddy viscosity, w_s is the settling velocity, C_{eq} the equilibrium concentration, in this case a modified Soulsby-Van Rijn bedload equation (see Section 4.1.5), and R_{cs} is the ratio between near-bed concentration and the mean concentration.

Adding extra velocity components in the advection-diffusion equation, results into a non-mass conservative velocity field. Hence, updated advection schemes were implemented for cross-shore transport modelling, based on the NERD scheme (SCHEME FOR ADVECTION OF TRACERS = 13 or 14) and on the ERIA scheme (SCHEME FOR ADVECTION OF TRACERS = 15). The updated schemes has been described and validated in Fonias et al. (2021) and they are not presented here. Note that the addition of velocity components, which account for cross-shore sediment transport is based on the corresponding implementation in XBeach (Roelvink et al., 2009).

The (Eulerian) velocities U^E and V^E replace the mean velocities U^L and V^L (Lagrangian), which are calculated by the flow module (TELEMAC). The incorporation of the contribution of each cross-shore mechanism to the velocity field responsible for the advection of sediment can be expressed as:

$$\vec{U}^E=\vec{U}^L+\left(\vec{U}_{NL}-\vec{U}_{ST}-\vec{U}_{SR}\right) \quad (2)$$

where $\vec{U}_{NL}$ is the contribution of wave non-linearity, $\vec{U}_{ST}$ is the Stokes drift and $\vec{U}_{SR}$ is the contribution of surface rollers. The aforementioned mechanisms are described in the following paragraphs.

4.1.2 Stokes drift – Return flow

When waves approach the coastal areas, a mean current directed to the shore, called Stokes drift, is formed in the upper part of the water column, because the motion of water particles do not follow a perfectly circular track. According to the Eulerian approach, this mean current has to be counterbalanced. Hence an opposite directed current of the same magnitude, is developed in the water column below the wave trough, contributing to the offshore directed sediment transport. The Stokes drift is given by the following expression:

$$U_{ST}={}^{E_w}\!/_{\rho hc} \quad (3)$$

where, E^w is the wave-group varying short wave energy given by the following expression:

$$E^w = \rho g H_s^2 / 16 \qquad (4)$$

In the above expression ρ is the water density, c is the phase velocity, g is the gravitational acceleration and H_s is the significant wave height.

4.1.3 Wave non-linearity

The wave non-linearity consists of two mechanisms, i.e. wave skewness and wave asymmetry, which both contribute to the onshore directed sediment transport.

Wave skewness (*Sk*) indicates that wave crests are higher and shorter in duration than the troughs. The shoreward velocity under the crest is higher than the seaward velocity under the wave trough (skewness). Wave asymmetry (*As*) refers to the higher acceleration of the wave front compared to the wave tail.

The contribution of wave non-linearity is calculated by means of an extra velocity component in the advection-diffusion equation:

$$U_{NL} = (f_{Sk} Sk - f_{As} As) u_{rms} \qquad (5)$$

where f_{Sk} and f_{As} are calibration factors with values from 0 to 1.0 and a recommended values of 0.1, u_{rms} is the root-mean square wave orbital velocity computed as:

$$u_{rms} = U_w / \sqrt{2} \qquad (6)$$

and U_w is the wave orbital velocity. The expressions for skewness *Sk* and asymmetry *As* can be found in Fonias et al. (2021).

4.1.4 Surface rollers

During wave breaking, part of the wave energy is transformed into momentum transferred in an aerated region at the wave front, known as the surface roller. The energy stored by the surface roller from the breaker is released in the surf zone contributing to the wave-induced sediment transport (offshore directed). The surface roller energy (E_r) evolution and dissipation is given by the following energy balance equation

$$\frac{\partial}{\partial t}(E_r) + \frac{\partial}{\partial x}(c_x E_r) + \frac{\partial}{\partial y}(c_x E_r) = -D_r + D_w \; (7)$$

where c_x and c_x are the x and y components of the phase velocity, D_w is the dissipation due to wave breaking and D_r is the roller dissipation given by:

$$D_r = 2g(\beta_s / \beta_2) E_r / c \qquad (8)$$

where β_s and β_2 are calibration parameters usually assumed equal to 0.1 and 1.0, respectively. The implementation of surface rollers in TOMAWAC is extensively described in (Breugem, 2020) and is available since TELEMAC release v8p5.

The contribution of surface rollers in cross-shore sediment transport is introduced by an extra velocity component in the advection-diffusion equation (Svendsen, 1984):

$$U_{SR} = 2E_r / (ch) \qquad (9)$$

4.1.5 Wave breaking turbulence

Wave breaking is a process highly connected with the generation of turbulence at the collapsing wave front. In the surf zone turbulence energy is transferred towards the seabed resulting into stirring up of sediment. The model utilized for describing the wave-breaking turbulence impact near the bed is proposed by van Thiel de Vries (2009) and it is based on the exponential decay model by Roelvink & Stive (1989). The model for the computation of the wave-averaged near-bed turbulence energy (k_b) by van Thiel de Vries, adopted in the present work, is given by:

$$k_b = D_r^{2/3}/(\exp(h/L_{mix}) - 1) \qquad (10)$$

where L_{mix} is the mixing length, expressed as the thickness of the surface roller and depends on the roller volume A_r (Svendsen, 1984b):

$$L_{mix} = \sqrt{A_r} = \sqrt{2E_rT/c} \qquad (11)$$

where T is wave period.

The wave turbulence effect on sediment transport is introduced through the equilibrium concentration formula, $C_{eq,}$, according to the suggestion by van Thiel de Vries (2009). Specifically, the Soulsby-van Rijn equation (Soulsby, 1997) is properly modified considering increased wave orbital velocity (U_w) due to the contribution of turbulence:

$$C_{eq} = \frac{A_s}{h}\left(\sqrt{\overline{U}^2 + 0{,}018 u_{rms,2}/C_d} - \overline{U}_{cr}\right)^{2.4} \qquad (12)$$

where A_s is a coefficient that includes both bed load and suspended load parameters (A_{sb}, A_{ss}), $\overline{U}$ is the mean current velocity, $\overline{U}_{cr}$ is the critical velocity for the initiation of motion, C_d is the drag coefficient and $u_{rms,2}$ is the modified root-mean-square wave orbital velocity:

$$u_{rms,2} = \left(\sqrt{U_w^2 + \gamma_{turb} k_b}\right)/\sqrt{2} \qquad (13)$$

where γ_{turb} is a turbulence coefficient which can be set equal to 1.45 according to by van Thiel de Vries (2009).

4.2 Modification of the fortran files

For optimal implementation of the cross-shore transport mechanisms and the Neumann boundary conditions, the following modifications of selected fortran subroutines of the GAIA code were applied:

- *gaia_cross_shore.f*:
    1. The new cross-shore transport mechanisms are introduced in this subroutine, i.e. the contributions of the Stokes drift, the wave non-linearity and the surface rollers, presented in the previous section, are calculated in this subroutine.
    2. Since the cross-shore current contribution is valid only at the domain where wave calculations take place (i.e. at the intersection of TEMEMAC and TOMAWAC domain), cross-shore current is calculated only when wave period (T_p) is non-zero.
    3. Wave asymmetry becomes increasingly important as the waves shoal in the shallower water. According to Bosboom & Stive (2023), the wave asymmetry becomes important when

$$h \approx 0.01 g T^2 \qquad (14)$$

This suggestion is taken into account in the subroutine, by introducing increased f_{As} calibration factor for depths smaller than the one in Eq. (14). After a sensitivity analysis performed in the numerical representation of the 'CROSSTEX' laboratory experiment (Kolokythas *et al.*, 2024), it was found that the model performed better when an increase in f_{As} was coupled with the reduction of the wave skewness (f_{Sk}) calibration factor. The exact expression for the definition of the critical depth of Eq. (14) used in the code is:

$$h = d_c 0.01 g T_m^2 \qquad (15)$$

where d_c is a calibration coefficient ranging between 0.5 and 1.0 and T_m is the mean wave period.

4. Bed slope effects are introduced in the advection-diffusion equation for suspended sediment through modification of the convection velocities (U_E & V_E):

$$\overrightarrow{U_{E,mod}} = \overrightarrow{U_E} - bU_{mag}\partial z_b/\partial n \qquad (16)$$

where b (=1) is a calibration factor, U_{mag} is the magnitude of the velocity and z_b is the bed level. Note hereby that this formulation is different from the Kock and Flokstrat formulation that is used when sediment transport is calculated using the Exner equation. In particular, it does not have a dependence on the of the direction on the bed shear stress.

5. If cross-shore contribution is not considered, then the convection velocities (U_E & V_E) are not zeroed (as it used to be before), they just keep the incoming TELEMAC values.

6. A calibration factor (CP_1) for U_{ST} is introduced in this subroutine.

- *suspension_sandflow_gaia.f:*
  1. A modification took place in this subroutine so that the bed load component is taken into account in the calculation of the equilibrium concentration, C_{eq}, according to Soulsby-Van Rijn equation.
  2. The equation for calculation of C_{eq} is modified to include the contribution of (near-bed) wave breaking turbulence according to Eq. (12) and Eq. (13).
  3. To reduce instabilities at wet-dry areas C_{eq} is zeroed for h<0.1m.
  4. A calibration factor (A_{cal}) for C_{eq} is also introduced in this subroutine.

- *bed1_suspension_erode.f & bed1_suspension_deposit.f:*
  1. A modification took place in both subroutines in order to allow bed updating in a specified sub-domain (polygon) of the computational domain. This was implemented in order to avoid instabilities and unwanted increased sedimentation/erosion at the lateral and offshore boundaries.

- *gaia_step.F:*
  1. This subroutine is modified so that a high-order filter (*filter_ho.f*) can be applied to the updated bottom (after the invocation of *gaia_evolutions.f*), in order to reduce instabilities at the dry-wet areas. More details about the filter implementation can be found in Breugem (2022). Note that a special treatment is applied so that the non-erodible areas and the grid cells with negligible bed changes are excluded from the filtering process.

- *prep_advection_gaia.f:*
  1. The modification that took place in this subroutine is related to the ratio between near-bed concentration and the mean concentration (R_{cs}) or simpler the concentration ratio R_{cs}. The modification allows for varying R_{cs} depending on water depth and sediment characteristics representing more properly the entrainment response of sediment (adaptation time) in a similar manner as XBeach model does. Instead of a constant value defined in the cas-file (R_{cs_cas}), R_{cs} is now calculated as:

$$R_{cs} = \min\left(h/(w_s T_{min}),\ R_{cs\_cas}\right) \qquad (17)$$

where T_{min} is a time-scale that regulates adaptation time and it is related to the wave period. A proposed expression for the calculation of T_{min}, which resulted after a calibration procedure, is:

$$T_{min} = T_p\left(T_p/T_{p,min}\right)^a \qquad (18)$$

where $T_{p,min}$ = 2 s and α = 2.

4.3 Sensitivity tests

The sensitivity tests presented in this section refer to the following numerical and physical parameters and mechanisms introduced in the GAIA module:

1. Bed update filtering
2. Concentration ratio (R_{cs})
3. Wave asymmetry & skewness
4. Bed slope effect
5. Soulsby-van Rijn sediment transport formula magnitude
6. Return flow (Stokes drift) magnitude
7. Advection scheme for suspended sediment
8. Coupling period for TELEMAC-TOMAWAC

For the sensitivity tests a simulation period of 80 days in 2016 (from 02/09/2016 to 21/11/2016) was considered. The starting date of the simulations is identical to that of the morphological validation period, which will be presented later. It was decided though, to keep the sensitivity tests relatively shorter in duration compared to the validation simulations (243 days) in order to execute as many tests as possible saving computational time. All in all, the simulation period of the sensitivity tests has been found to be adequate for the purposes of the sensitivity analysis.

Note that a typical simulation of this series of tests lasts around 16.5 hours on 32 cpus of one Bernoulli node.

4.3.1 Bed evolution filtering

The need for bed evolution filtering resulted from the findings of relatively long-term morphological simulations with cross-shore mechanisms included. As shown in Figure 23, where the bed level change within 8 months at the area around Ostend harbour is depicted, instabilities appear at the shallow (intertidal) area along the coast. The numerically predicted bed evolution for the same period shown in Figure 24, corresponds to a simulation where cross-shore current contributions are deactivated. Comparing the bed evolutions of the aforementioned figures, it is obvious that the introduction of the cross-shore mechanisms in the model is the reason behind this unwanted behaviour of the model. Note that the numerical results shown in Figure 23, present already reduced instabilities, as some fixes of those mentioned in section 4.2, helped in this direction. As any other attempt didn't contributed substantially in improving the behaviour of the model at the shallow, it was decided to implement a high-order filter for the bed updating (section 4.2) in order to minimize or reduce the instabilities without affecting the mass balance of the sediment.

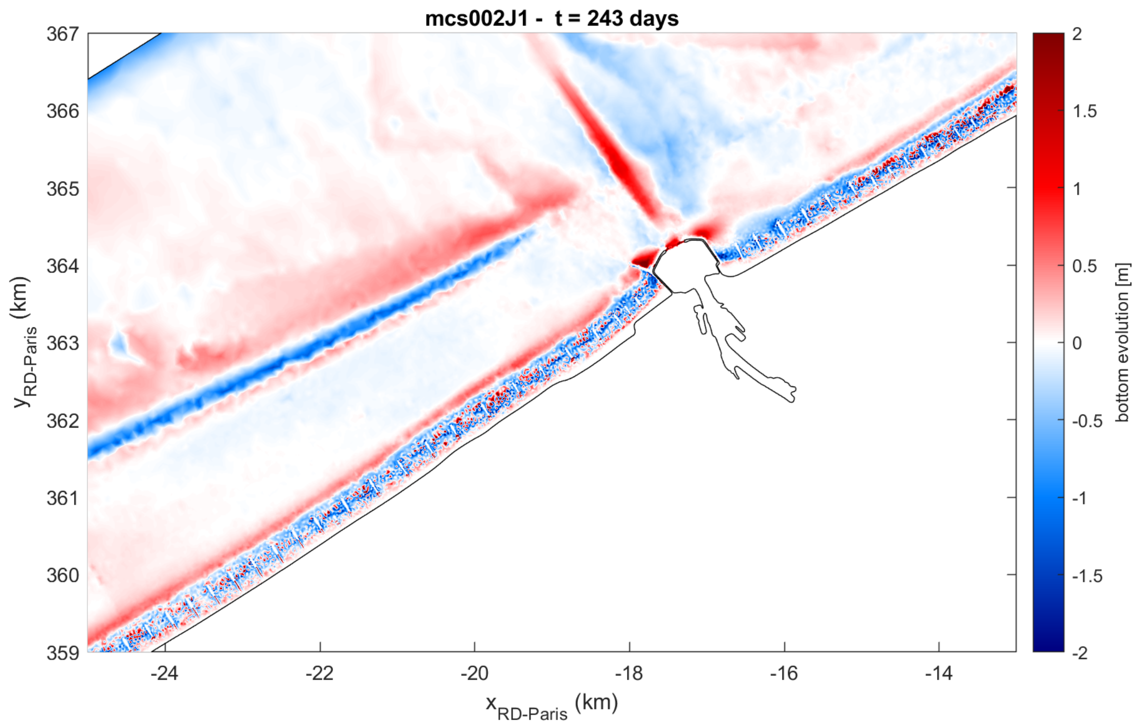

Figure 23: Bed level change [m] at the end of the simulation period (8 months) with cross-shore processes activated.

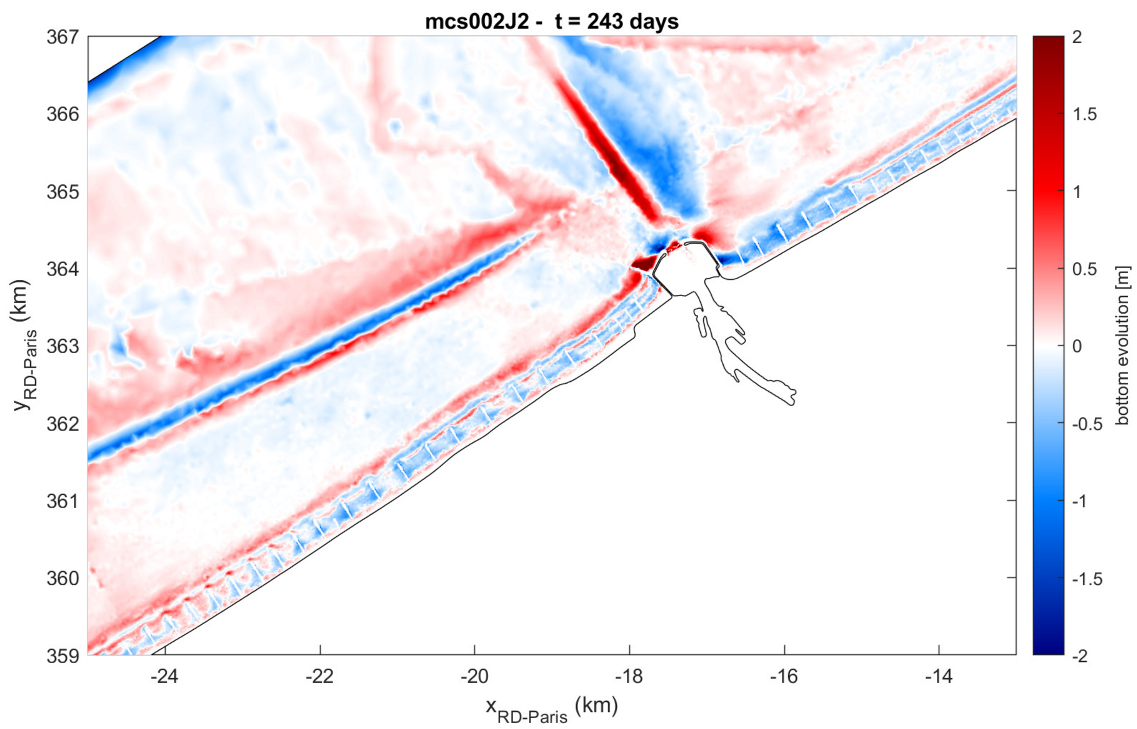

Figure 24: Bed level change [m] at the end of the simulation period (8 months) with cross-shore processes deactivated.

The high-order filter (*filter_ho.f*) is regulated by two parameters, i.e. NUMORDER, which determines the order of the filter and NUMITER, which defines the number of desired iterations of the filter implementation. Obviously, the filter becomes more effective for decreasing NUMORDER and increasing NUMITER values. A series of tests for the calibration of the filter were conducted as shown in Table 8.

Table 8: Calibration parameters of the high-order filter implemented for bed evolution.

Run ID	HO - FILTER	NUMORDER	NUMITER
mcs002I8	OFF	-	-
mcs002I32	ON	1	1
mcs002I33	ON	1	5
mcs002I34	ON	2	1
mcs002I35	ON	2	2
mcs002I31	ON	3	1

In Figure 25 the bed evolution at the end of the test simulation without implementation of bed filtering is shown. Bed level instabilities are obvious close to the coastline, especially at the east of Ostend harbour. In Figure 26, three different set-ups of the high-order filter applied during the temporal update of the bottom, are shown. Specifically, the run with the lowest order and number of iterations (mcs002I32) is compared to the one of the higher order (mcs002I31) and the one with the largest number of iterations (mcs002I33), in order to evaluate the influence of each of the two calibration parameters. Apparently, the filter of the higher order (NUMORDER=3) has less influence on the numerical results, as observed when comparing them with the corresponding ones of Figure 25 (reference run mcs002I8). On the contrary, when the filter is applied iteratively (NUMITER=5) the smoothening of the instabilities is rather exaggerated (see bottom panel of Figure 26). The first-order filter applied only once (NUMORDER=1, NUMITER=1) seems to achieve a more balanced smoothening even though it might lead in an overestimated smoothening at areas of increased seabed slopes interpolated at relatively low resolution grid, i.e. at the area of Stroombank. The aforementioned findings are better presented in the bed profile evolutions of Figure 28 and Figure 29 at Mariakerke and at the eastern 'edge' of Stroombank. The precise location of the profiles is shown in Figure 27.

It has to be mentioned that the high-order filter was also tested for the convection velocities, instead of the updated bottom, but the effect on the numerical results was negligible.

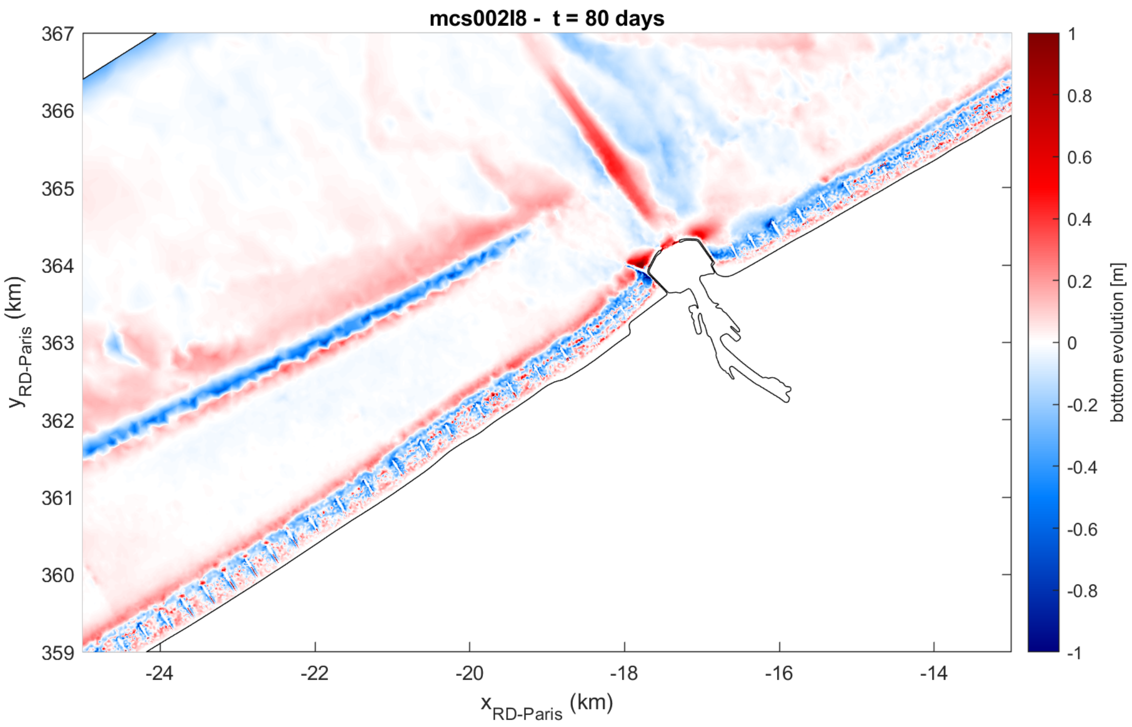

Figure 25: Bed level change [m] at the end of the simulation period (80 days) for the run without bed filtering.

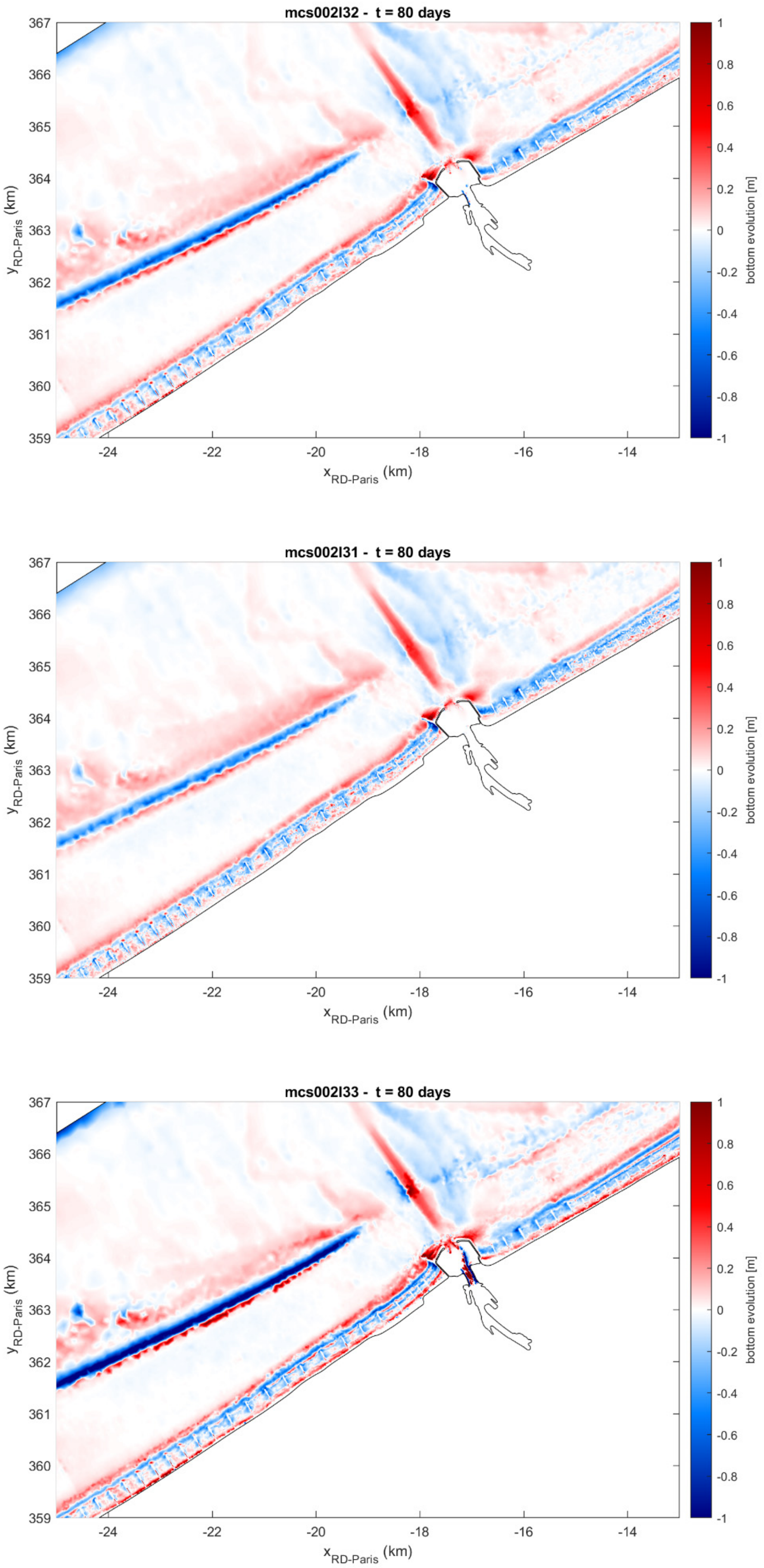

Figure 26: Bed level change [m] at the end of the simulation period (80 days) for three different high-order filter settings.

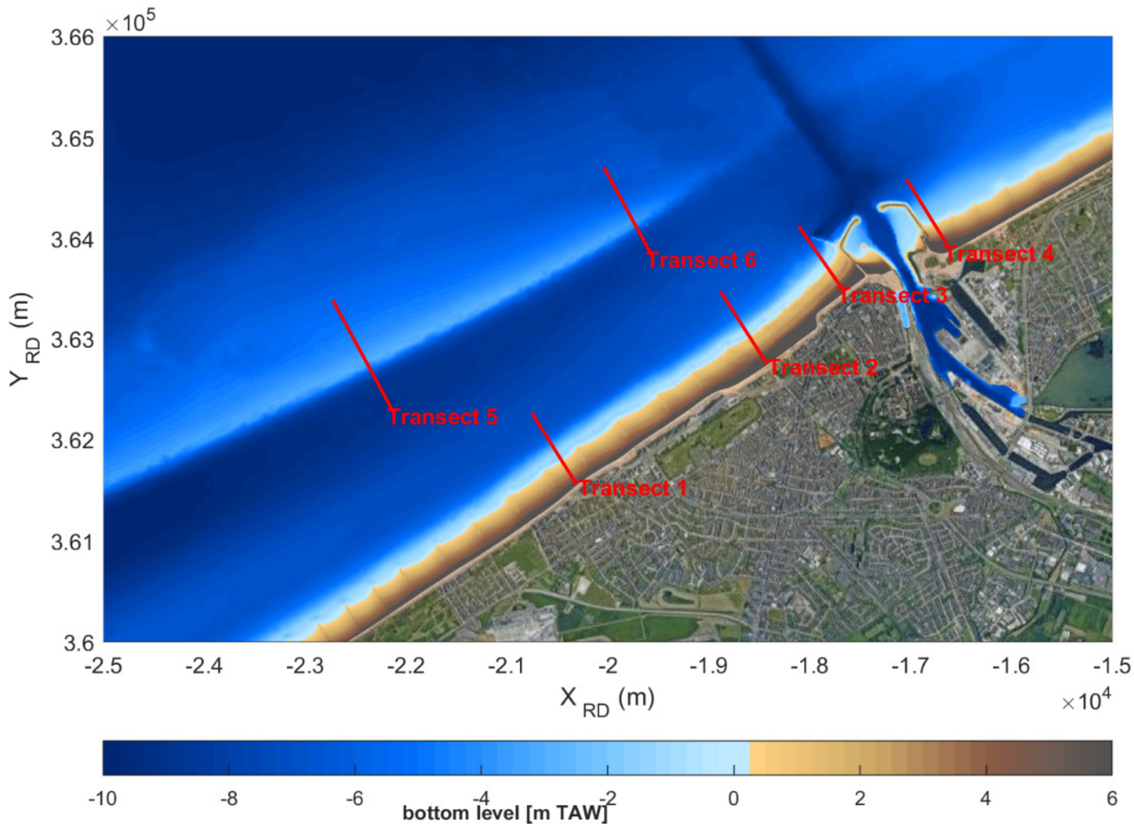

Figure 27: Location of the transects for bed profile extraction.

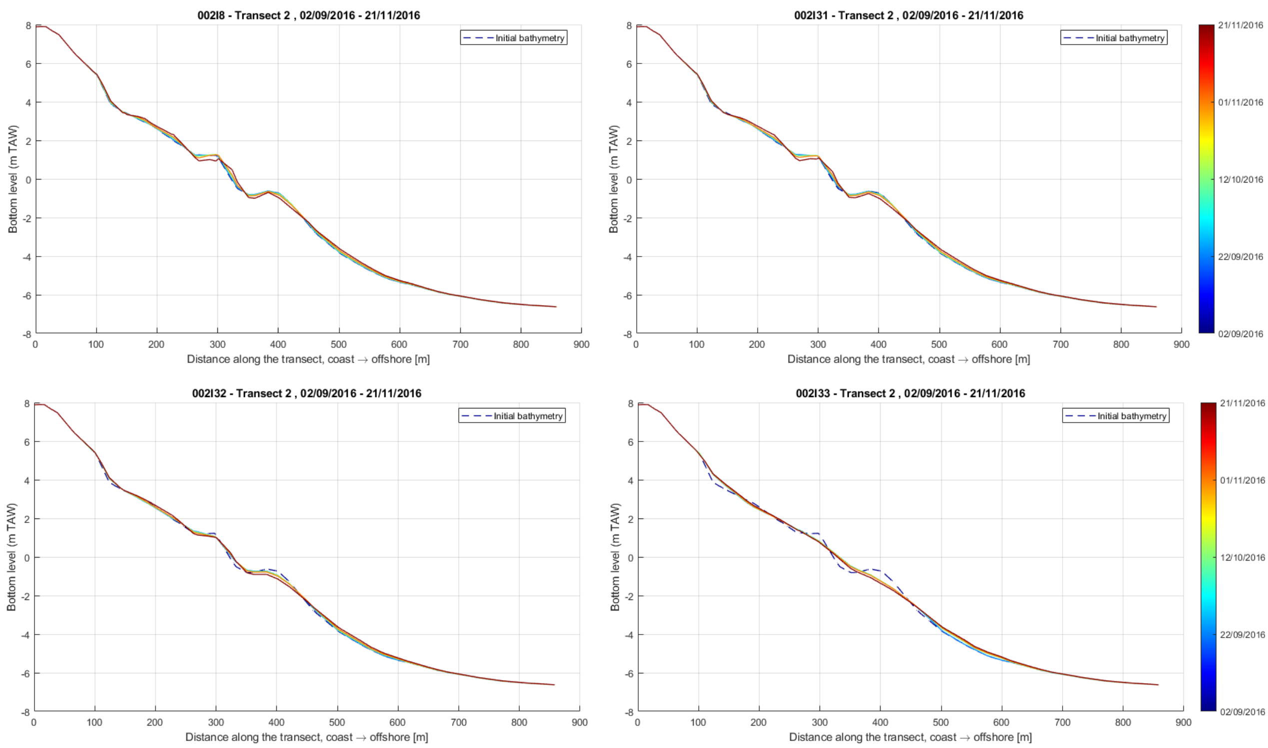

Figure 28: Bed level change [m] at Transect 6 during simulation without filtering and for three different high-order filter settings.

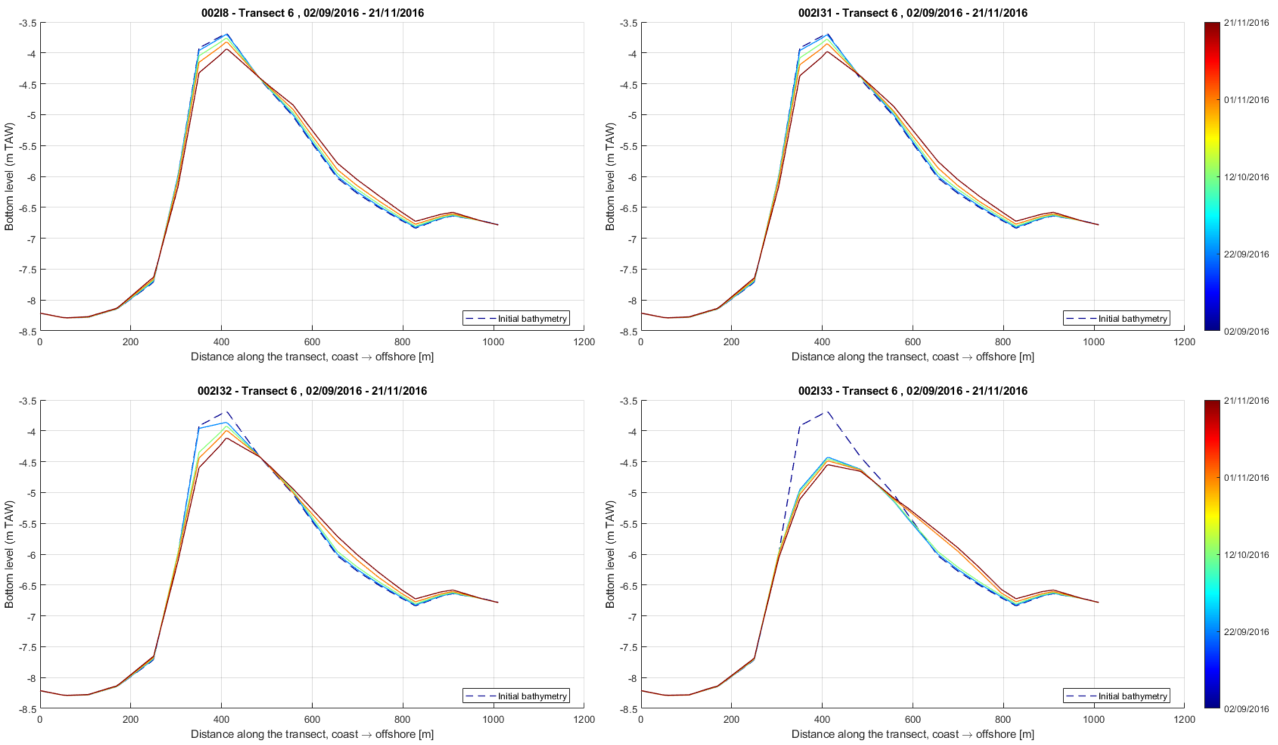

Figure 29: Bed level change [m] at Transect 2 during simulation without filtering and for three different high-order filter settings.

4.3.2 Concentration ratio R_{cs}

Concentration ratio R_{cs} is an important parameter for suspended sediment transport, as it determines how fast the sediment responds to the driving forces exerted on the movable seabed. According to Eq. 17, low values of R_{cs} correspond to large adaptation time (T_{min}) and hence to more diffusive behaviour of the model. On the contrary, larger R_{cs} values correspond to quick response of sediment to entrainment (model becomes less diffusive). The parameter settings for the sensitivity tests of the concentration ratio are presented in Table 9. Note that in the tests for bed filtering presented in the previous section, R_{cs} was considered equal to 1. Also note that the expression for the varying R_{cs} in tests mcs002I41 and mcs002I42 is given by Eq. 17 in section 4.2.

In Figure 30, the bed evolution at the end of the simulation period (80 days) for the reference run with R_{cs} = 1, is presented. In Figure 31 and Figure 32, the corresponding numerical results are shown for the tests with R_{cs} = 10 (constant all over the domain) and spatially-varying R_{cs} ($R_{cs,max}$ = 10).

Table 9: Sensitivity tests for concentration ratio R_{cs} coupled with different bed filtering settings.

Run ID	R_{cs}	H-O Filter	
		NUMORDER	NUMITER
mcs002I32	1	1	1
mcs002I36	10	1	1
mcs002I41	varying ($R_{cs,max}$ = 10)	1	1
mcs002I42	varying ($R_{cs,max}$ = 10)	2	2

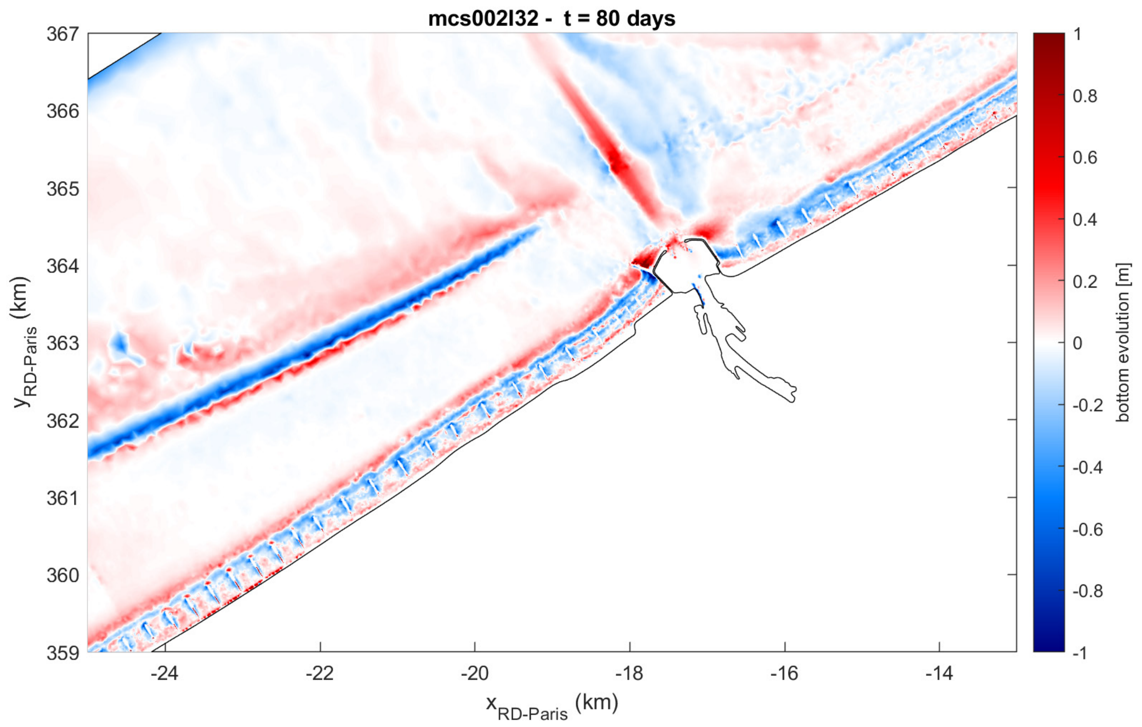

Figure 30: Bed level change [m] at the end of the simulation period (80 days) for the run with concentration ratio R_{cs} = 1.

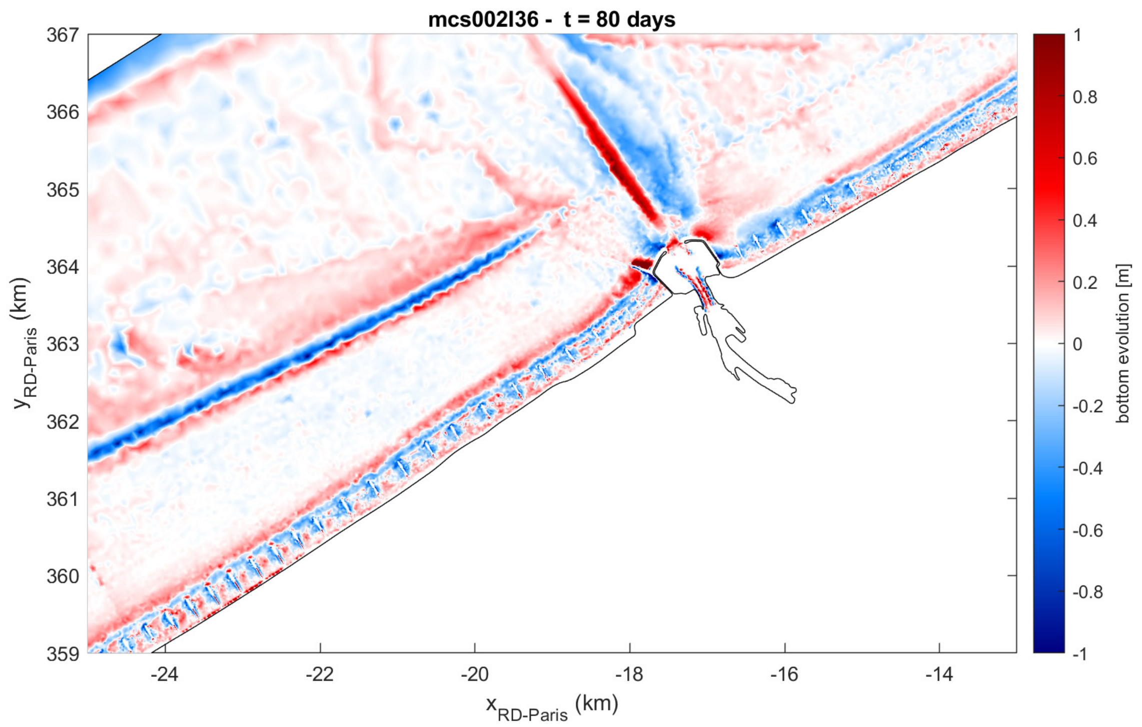

Figure 31: Bed level change [m] at the end of the simulation period (80 days) for the run with concentration ratio R_{cs} = 10.

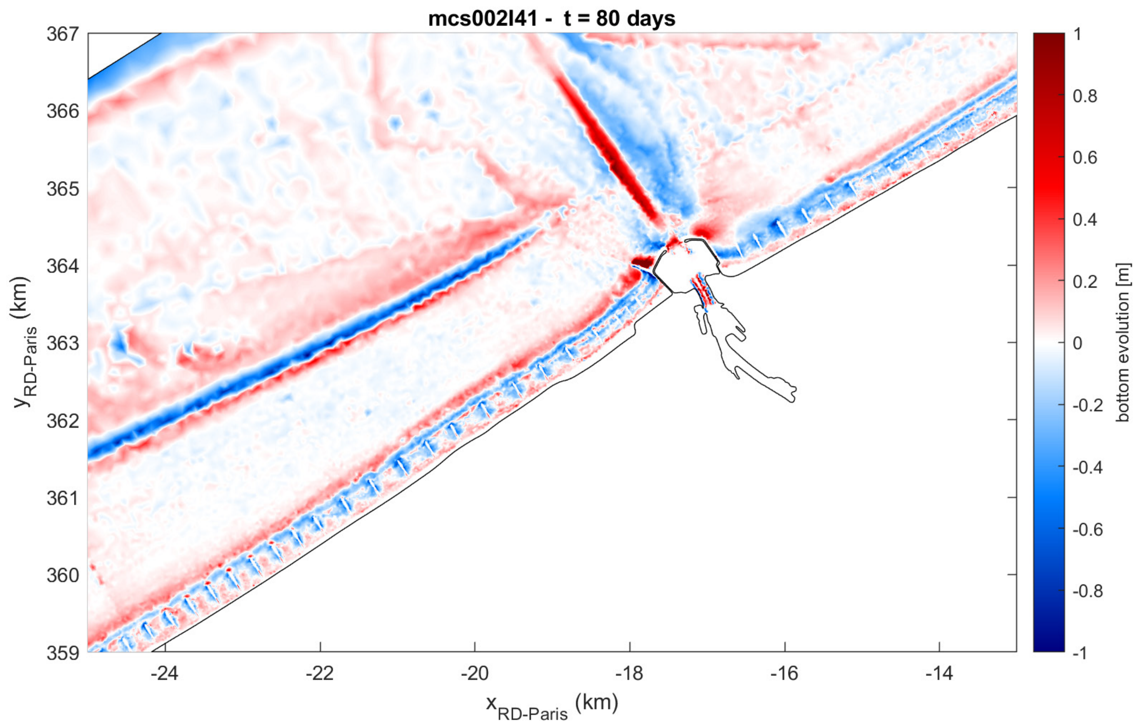

Figure 32: Bed level change [m] at the end of the simulation period (80 days) for the run with varying concentration ratio ($R_{cs,max}$ = 10).

Comparing Figure 31 to Figure 30 it can be observed that the sedimentation/erosion patterns in the first one (R_{cs} = 10) are more rough all over the computational domain and that these patterns are smoothened by use of a lower value for R_{cs} (=1). In Figure 32 it is indicated that using spatially varying R_{cs}, i.e. larger values at deeper and smaller at shallower, leads to smoother sed/ero patterns at the 'problematic' dry-wet areas along the coastline, while the bed evolution patterns at deeper are not smoothened excessively. It is worth mentioning that the increase of R_{cs} led to the appearance of an erosion pattern at the western breakwater of Ostend harbour (Figure 31 and Figure 32), which was apparently smoothened out for R_{cs} =1 (Figure 30).

The last test presented in Table 9 (mcs002I42) refers to the coupling of the successfully implemented spatially-varying R_{cs} with a 2nd order bed filter, in order to reduce numerical diffusion even more, but also ensuring that the instabilities at the dry-wet areas remain minimized. The sedimentation/erosion patterns are very similar to those of run mcs002I41, therefore a contour plot of the bed evolution is not presented here. In Figure 33, the bed profile evolution is shown for the 1st and the 2nd order bed filters at Transect 2 (Mariakerke), while in Figure 34 the bed profile evolution is presented at Transect 6 (Stroombank). Note that the precise location of the aforementioned transects is shown in Figure 27. It is found that the differences at the bed profile evolution at Mariakerke is limited, while the implementation of a higher-order filter results into substantially less diffusive behaviour of the model at the area of Stroombank.

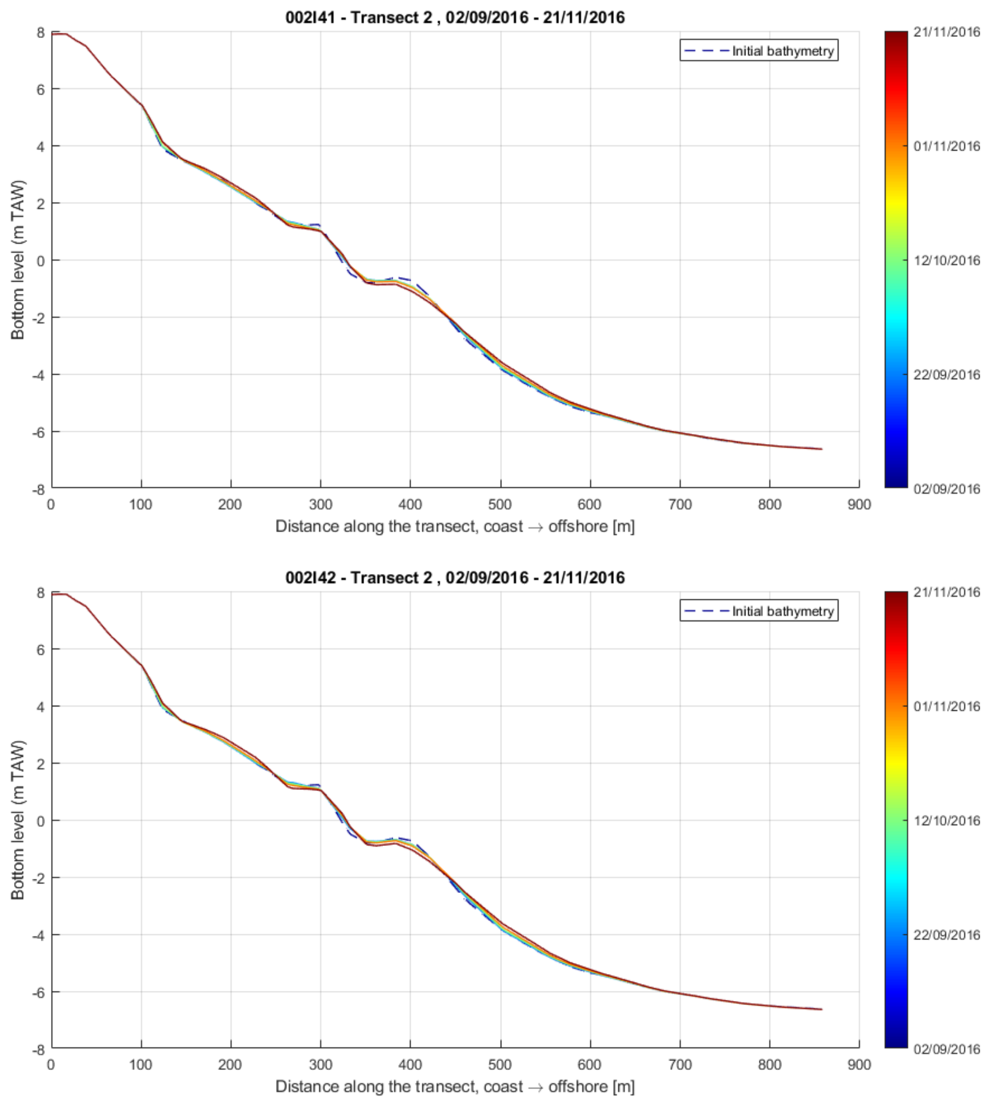

Figure 33: Bed level change [m] at Transect 2 (Mariakerke) during simulations with 1st order filter (top) and 2nd order filter (bottom) with varying concentration ratio ($R_{cs,max}$ = 10).

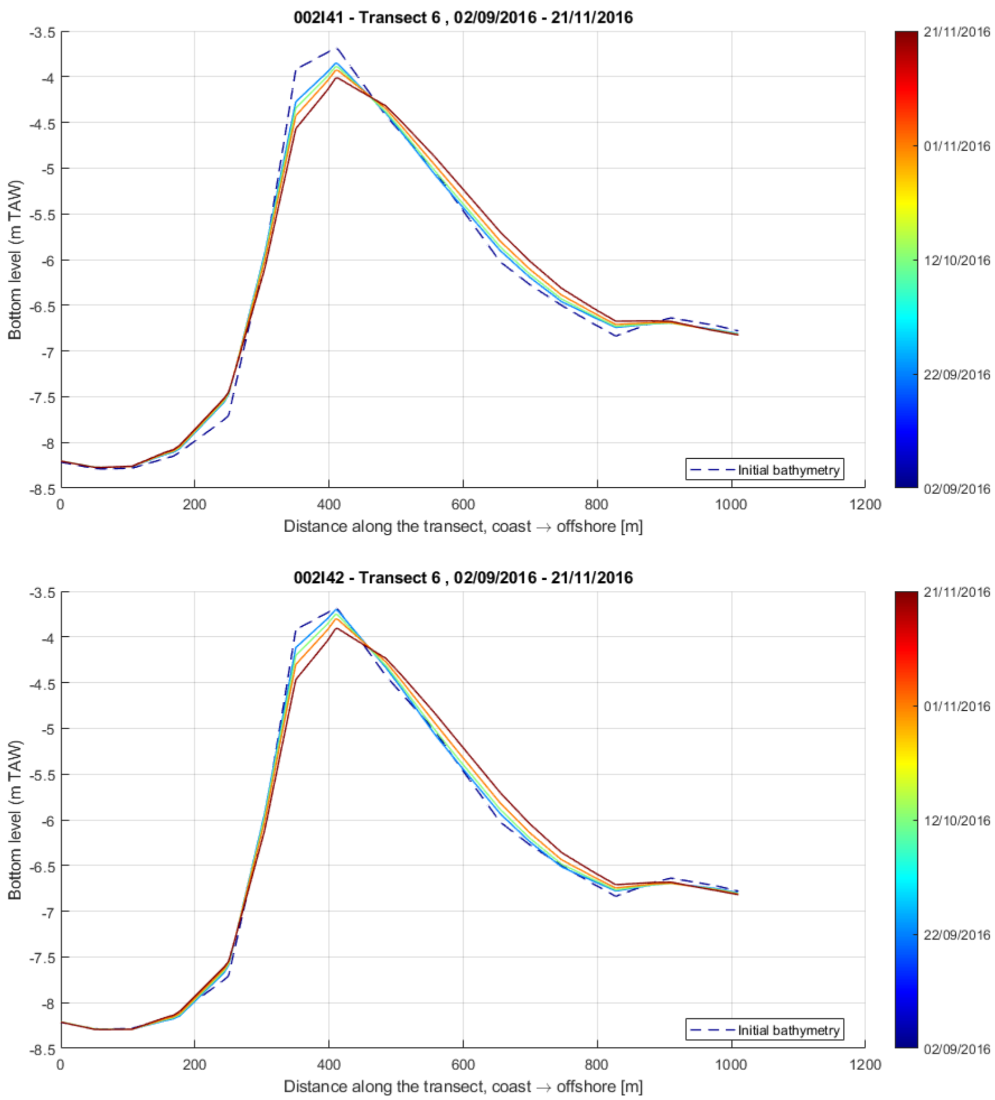

Figure 34: Bed level change [m] at Transect 6 (Stroombank) during simulations with 1st order filter (top) and 2nd order filter (bottom) with varying concentration ratio ($R_{cs,max}$ = 10).

4.3.3 Wave asymmetry & skewness

Wave asymmetry and wave skewness may play an important role on the onshore sediment transport in the surf zone, where the wave non-linearity increases and the waveform changes drastically. A series of tests was performed with different combinations of values for the calibration factors f_{As} and f_{Sk} and they are presented in Table 10. The reference simulation is mcs002I44, which has identical settings with mcs002I42 (presented in the previous section), except that the factors f_{As} and f_{Sk} are now considered constant all over the domain and equal to 0.1 and 0.3, respectively. In general, the factors f_{As} and f_{Sk} are considered constant everywhere in the domain for all the tests presented in Table 10. Note that for simulation mcs002I42 (and in general for simulations presented so far), f_{As} was increasing from 0.1 to 0.3 and f_{Sk} was decreasing from 0.3 to 0.1 for shallow water depths as defined by Eq. 15 of section 4.2. The reason for deactivating this feature of the model is to get a better understanding of the impact of the wave non-linearity mechanisms on cross-shore sediment transport in field conditions.

Table 10: Sensitivity tests for calibration factors f_{As} and f_{Sk} of wave assymetry and skewness.

Run ID	f_{As}	f_{Sk}
mcs002I44	0.1	0.3
mcs002I45	0.3	0.1
mcs002I49	0.1	0.1
mcs002I50	0.3	0.3
mcs002I59	0.1	0.5

In Figure 35 the bed evolution at the end of the simulation period for the reference run mcs002I44 (f_{As} = 0.1 and f_{Sk} = 0.3) and run mcs002I45 (f_{As} = 0.3 and f_{Sk} = 0.1) is presented. Comparing the sed/ero patterns close and along the coast, focusing at the west of Ostend harbour, it can be observed that the sedimentation line in front of the groin heads is more pronounced for the test run mcs002I45. In turn, the erosion among the groins is stronger, indicating enhanced offshore sediment transport. This outcome also shows that onshore directed transport is relatively weaker when the wave skewness contribution is reduced even though wave asymmetry is increased, indicating that wave skewness contributes more to the onshore movement of sediment (at least under the imposed forcing conditions). Note that in deeper areas the results of the two runs are almost identical, as expected.

The numerical predictions for bed evolution at the end of the simulation period for runs mcs002I49 (f_{As} = 0.1 and f_{Sk} = 0.1) and mcs002I50 (f_{As} = 0.3 and f_{Sk} = 0.3), are presented in Figure 36. The results show that the regulation of wave non-linearity components works as expected. Reducing calibration factor f_{Sk} from 0.3 to 0.1 (keeping f_{As} = 0.1) leads into relatively strong erosion among the groins and a more pronounced sedimentation line in front of them (see top panel of Figure 36). Then, increasing calibration factor f_{As} from 0.1 to 0.3 (keeping f_{Sk} = 0.3 as in the reference run), results again into stronger erosion among the groins, but now most of the sediment is transferred towards the coastline , indicating enhancement of onshore directed transport. This behaviour is coupled with the attenuation of the sedimentation line in front of the head of the groins.

The numerical results of the last test presented in in Table 10, i.e. mcs002I59 with increased calibration factor f_{Sk} (= 0.5), are presented in Figure 37. As expected, the onshore directed transport is excessively enhanced. The erosion patterns close to the coastline have been transferred more offshore, getting closer to the head of the beach groins, while sediment accumulation covers most of the area among the groins. The sedimentation line in front of the groins is attenuated.

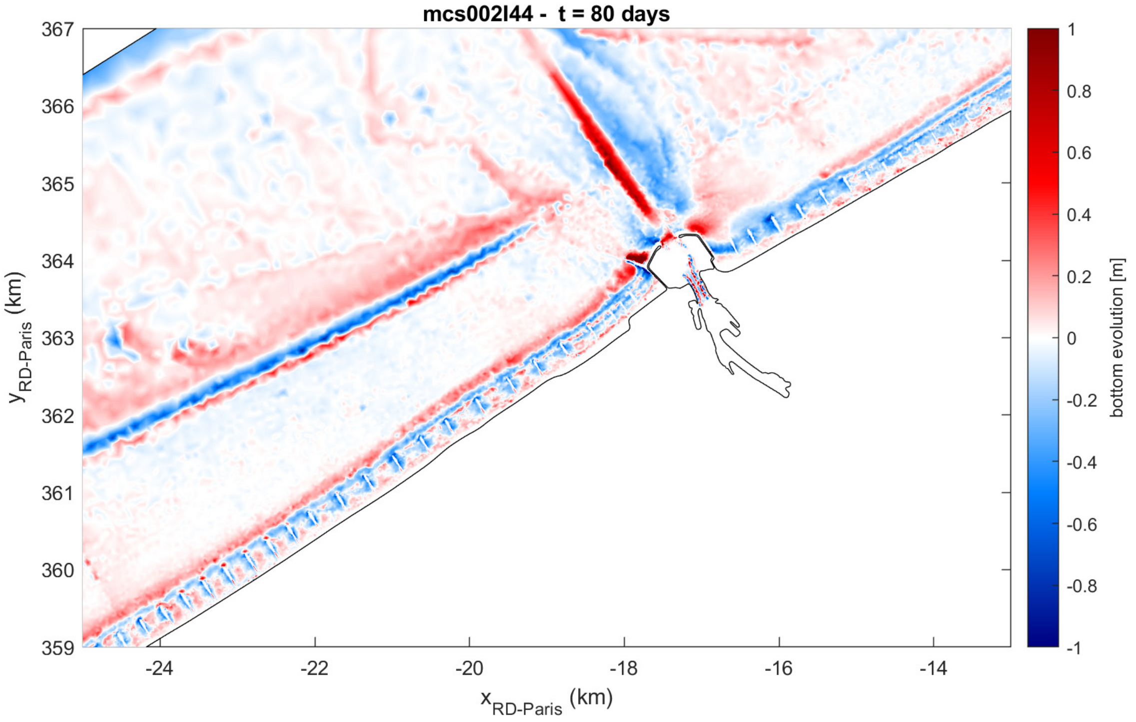

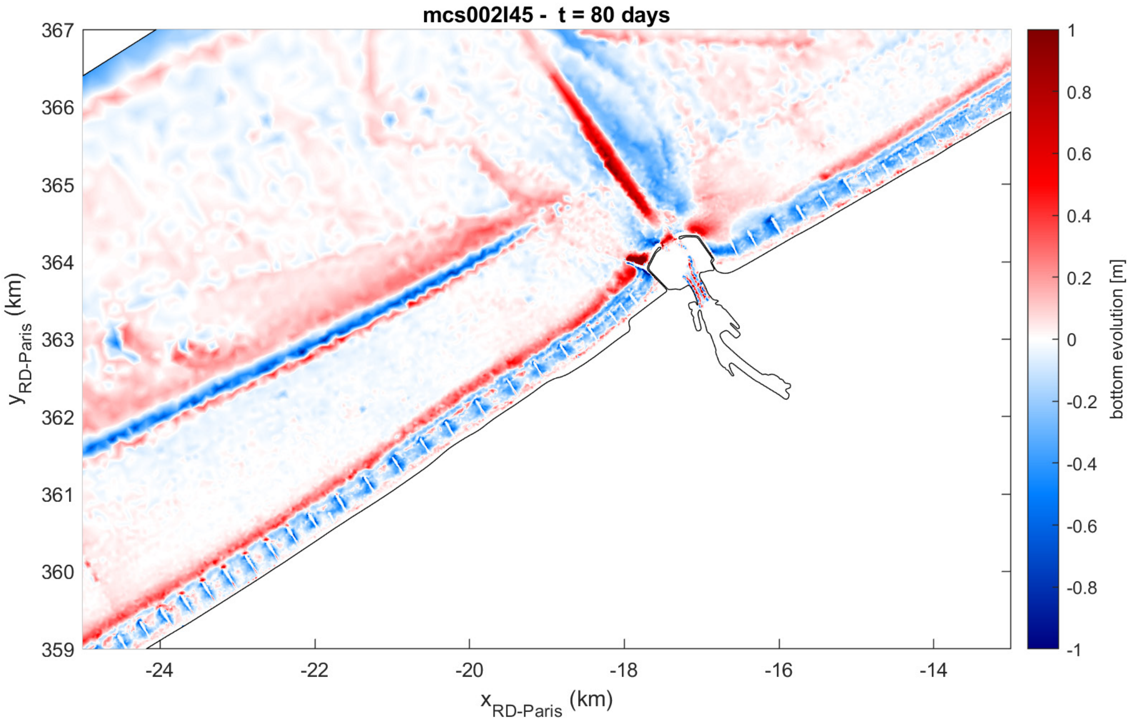

Figure 35: Bed level change [m] at the end of the simulation period for the f_{As} & f_{Sk} sensitivity tests mcs002I44 (reference) and mcs002I45.

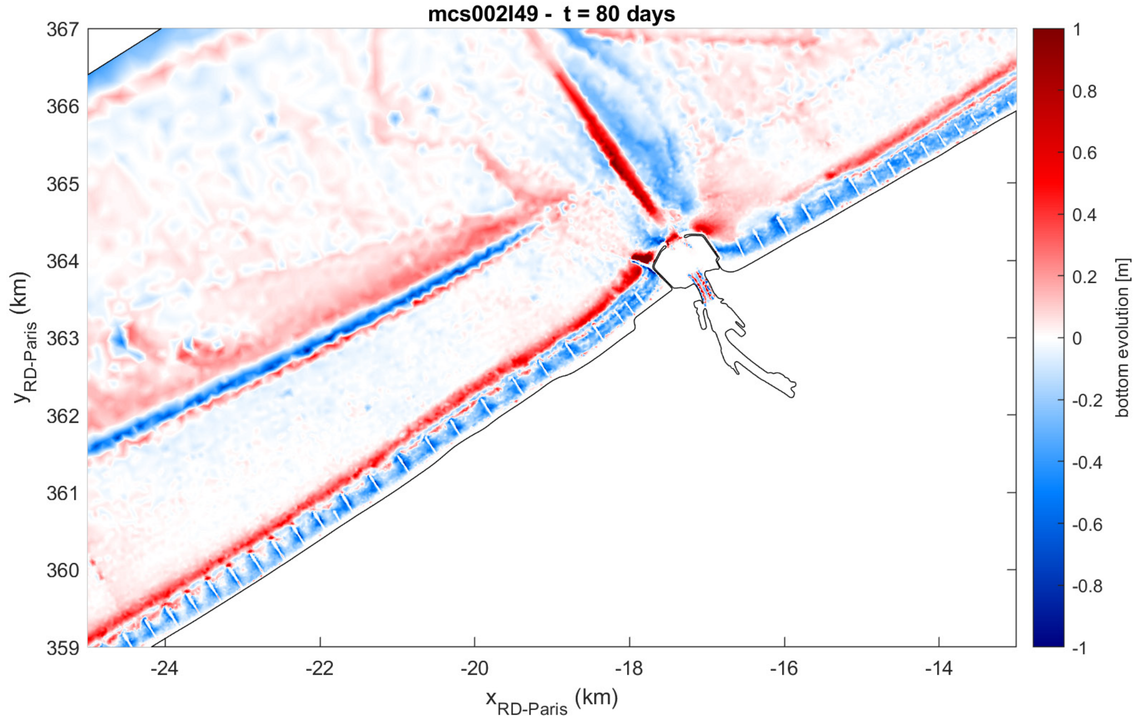

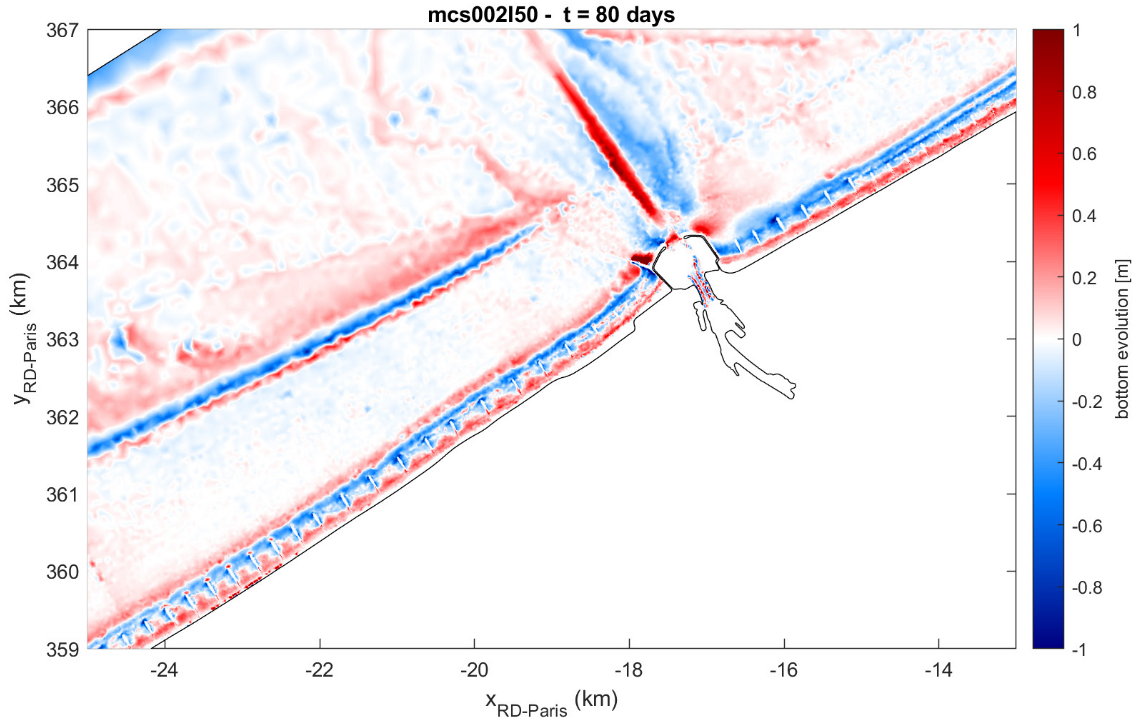

Figure 36: Bed level change [m] at the end of the simulation period for the f_{As} & f_{Sk} sensitivity tests mcs002I49 and mcs002I50.

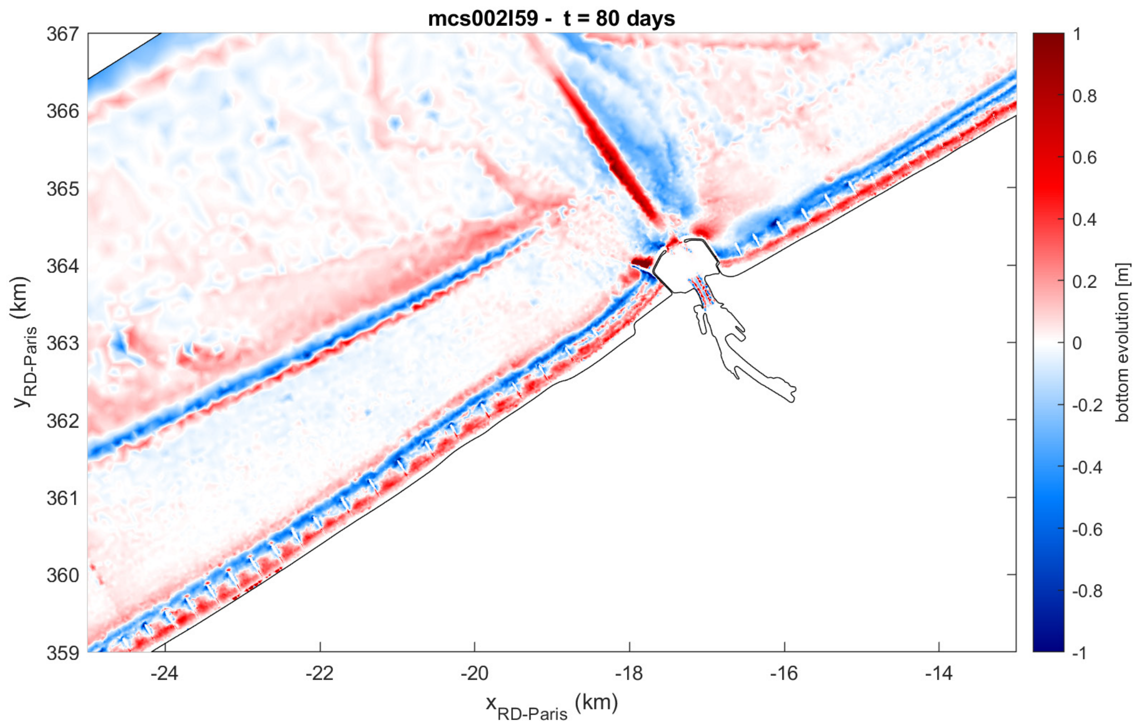

Figure 37: Bed level change [m] at the end of the simulation period for the f_{As} & f_{Sk} sensitivity test mcs002I59.

4.3.4 Bed slope effect

The bed slope effect is not taken into account in GAIA, when sediment transport is calculated by means of the advection-diffusion equation. The bed slope effect is introduced in the model through cross-shore transport modelling according to Eq. 16 presented in section 4.2, which modifies the convection velocities.

In Figure 38 the bed evolution at the end of the test simulation for the reference run mcs002I42 (bed slope effect is off) and run mcs002I61 (bed slope effect is on) is presented. Comparing the sed/ero patterns close to the coast, focusing at the west of Ostend harbour, it can be observed that the sedimentation line in front of the groin heads seems to be more pronounced for the test run mcs002I61. In turn, the erosion among the groins is somewhat stronger, indicating enhanced offshore sediment transport. This outcome shows that the bed slope effect is really contributing in cross-shore sediment transport. Also note that the sed/ero patterns along the crestline of Stroombank are again (slightly) more pronounced. This time, the bed slope effect contributes in the shoreward movement of sediment, as the (red) sedimentation line at the shoreward side of the bank is more intense when bed slope effect is activated.

Another attempt to incorporate bed slope effects took place by modifying the equilibrium concentration (C_{eq}) formula of Soulsby van Rijn (Eq. 12 – section 4.2). Specifically, the modification was introduced in the critical velocity for the initiation of sediment motion (U_{cr}) as similarly proposed by Soulsby (1997, eq.80a, p.107) for the correction of critical Shields number (ϑ_{cr}) and already implemented in GAIA for bedload transport formulas (option SLOPEFF=2). However the aforementioned method for bed slope effect led to results very similar to those of the (reference) simulation without bed slope effects, and therefore it was not considered further.

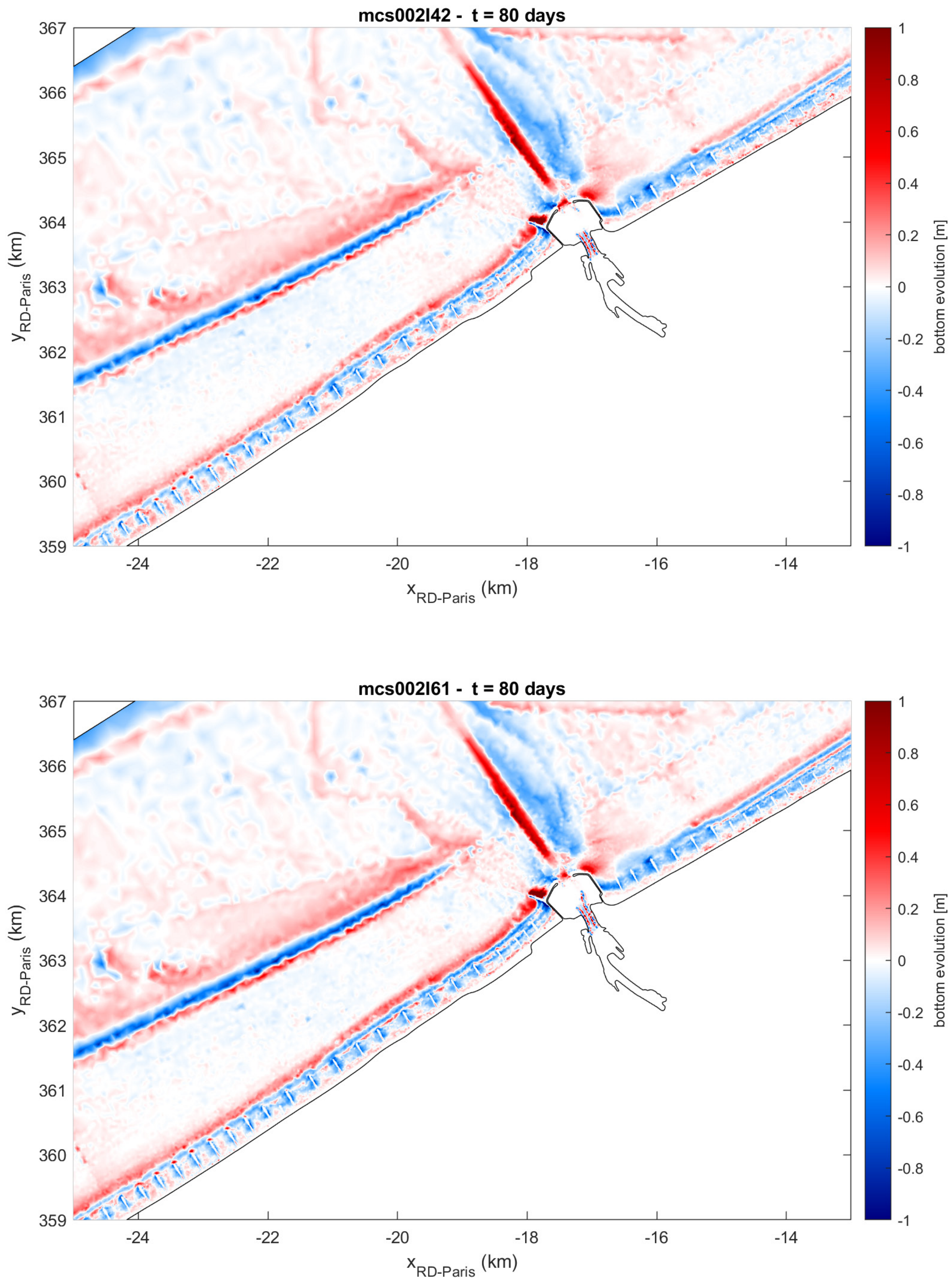

Figure 38: Bed level change [m] at the end of the simulation period for the f_{As} & f_{Sk} sensitivity tests mcs002I49 and mcs002I50.

4.3.5 Soulsby-van Rijn sediment transport formula magnitude

One of the formulas considered by GAIA is the total sediment transport formula by Soulsby (1997), which is introduced in the advection-diffusion equation (Eq. 1, section 4.2) in the form of the equilibrium concentration C_{eq} (sediment transport rate divided by water depth), given by Eq. 12. It has to be noted though that the calibration of such empirical sediment transport formulas is common in morphological simulations at coastal regions.

In this section the numerical results are presented of a sensitivity test (mcs002I54) with a calibration factor A_{cal} = 0.7 imposed to the originally calculated C_{eq} at every time-step. The utilized value for the calibration factor A_{cal} is proposed in the PhD thesis by Dastgheib (2012). The total bed level change after 80 days is depicted in Figure 39. Comparing the bed evolution patterns of this test to those of the reference run, i.e., mcs002I42 depicted in Figure 38 (top panel), it can be observed that their intensity is noticeably attenuated. This behaviour is expected as the calibration factor results into an indirect reduction (by 30%) of the sediment transport magnitude. This outcome is also noticeable in the bed profile evolutions of Figure 40 and Figure 41 at Mariakerke and (especially) at the eastern 'edge' of the Stroombank.

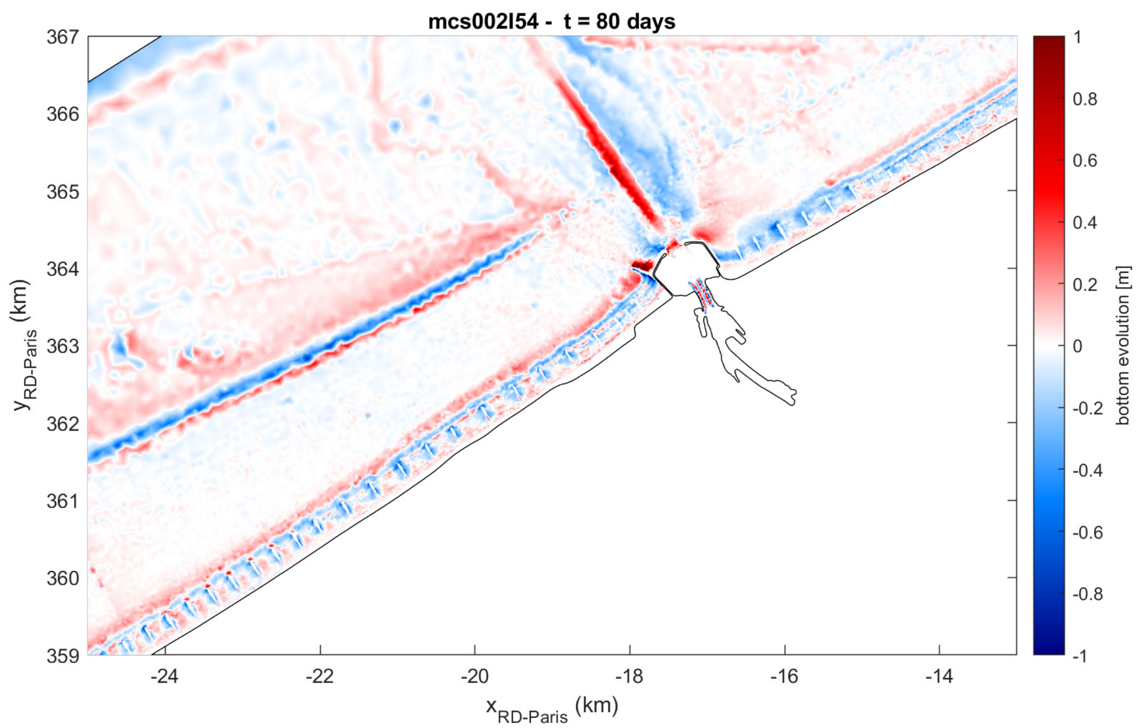

Figure 39: Bed level change [m] at the end of the simulation period for the sensitivity test (mcs002I54) with calibration factor A_{cal} = 0.7 imposed to C_{eq}.

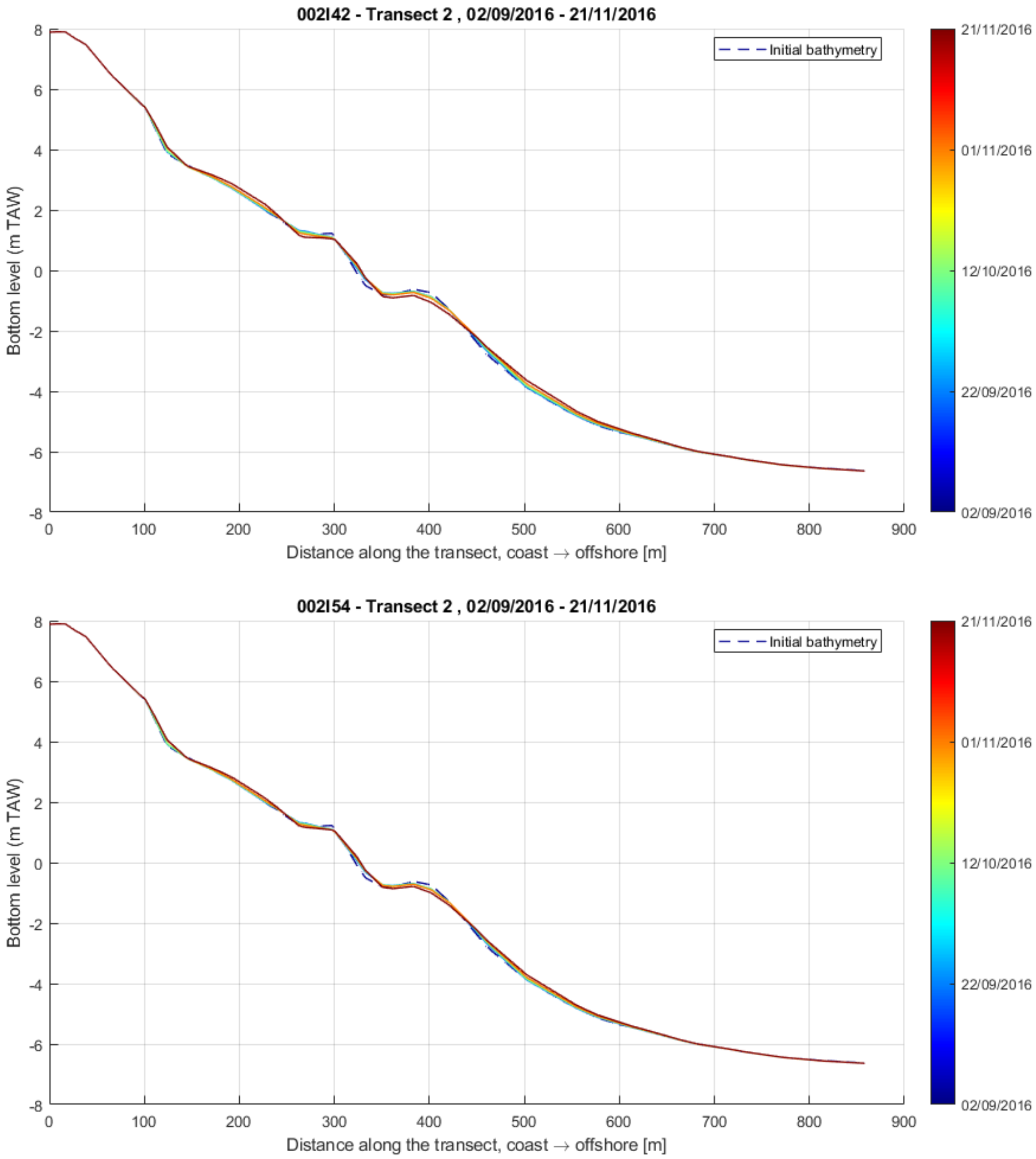

Figure 40: Bed level change [m] at Transect 2 (Mariakerke) during simulations with original SVR formula (top) and calibrated SVR formula (bottom) for C_{eq} calculation.

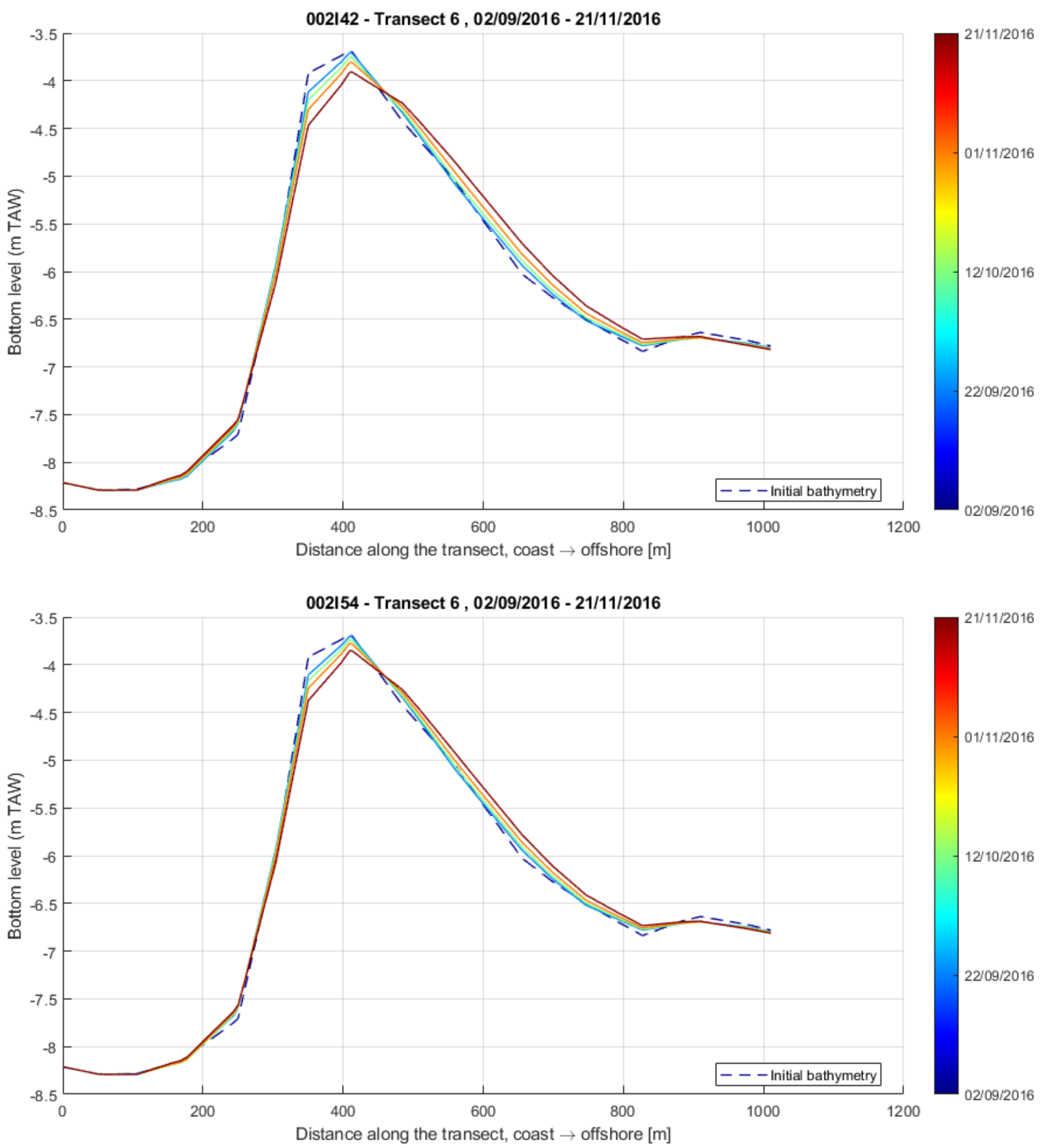

Figure 41: Bed level change [m] at Transect 6 (Stroombank) during simulations with original SVR formula (top) and calibrated SVR formula (bottom) for C_{eq} calculation.

4.3.6 Return flow (Stokes drift) magnitude

Return flow, which counterbalances Stokes drift, is the main driving mechanism of the offshore directed sediment transport in the surf zone. In this section the outcome of sensitivity test runs with different values of the calibration parameter (CP_1) for the magnitude of Stokes velocity U_{ST} is presented. The values of the calibration parameters are shown in Table 11. Note that the simulation period of these sensitivity tests is 243 days equal to the simulation period of the morphological validation which will be presented in the next chapter. Also note that the reference simulation settings are identical to those of the run mcs002I42 (with simulation period equal to 80 days).

In Figure 42 the bed evolution at the end of the reference run, i.e. after 8 months, is presented. As in the case of the shorter in duration simulations, the formation of a sedimentation line in front of the head of the beach groins, the erosion among the groins and the moderate gathering of sediment higher at the beach, are the main features of the nearshore bed evolution at the coast west of Ostend harbour.

Table 11: Sensitivity tests for calibration parameter CP_1 of Stokes velocity (U_{ST}).

Run ID	CP_1
mcs003D	1 (reference)
mcs003E	0.5
mcs003E1	0.75

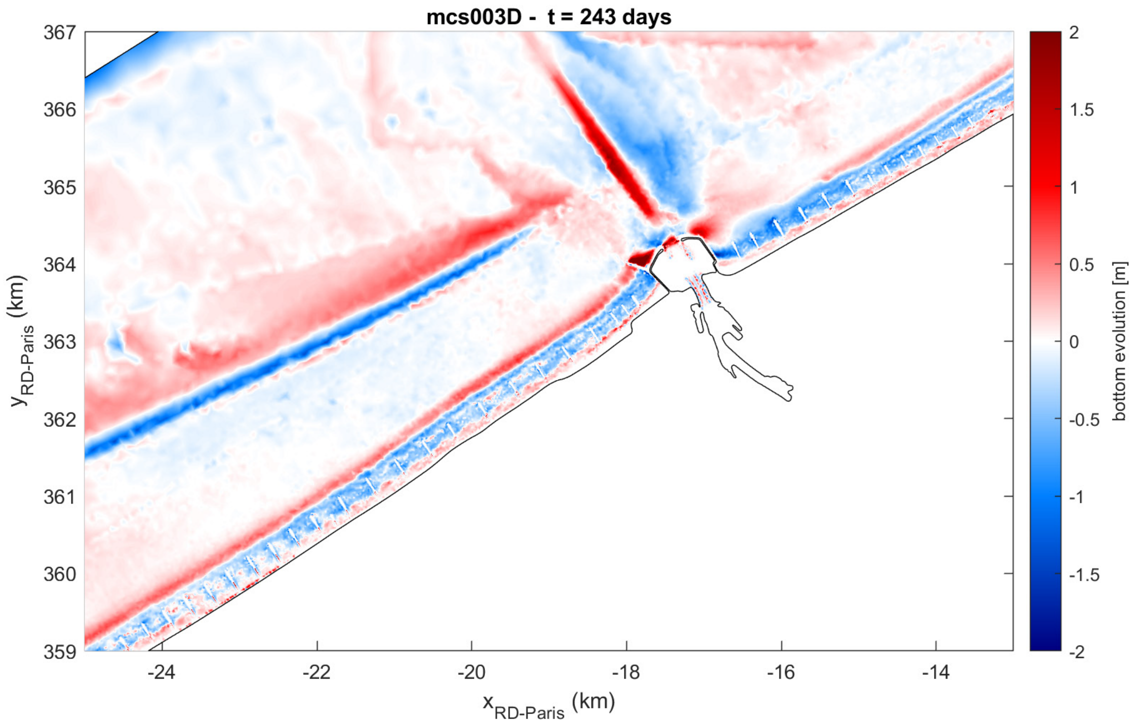

Figure 42: Bed level change [m] at the end of the simulation period (243 days) for the reference run mcs003D without U_{ST} calibration.

The numerically predicted bed evolution at the end of the simulation period for runs mcs003E (CP_1 = 0.5) and mcs003E1 (CP_1 = 0.75), are presented in Figure 43. The sed/ero patterns of the test run mcs003E, which considers 50% reduction of U_{ST} magnitude, indicate that the return flow is substantially weakened and hence the onshore directed transport prevails. The sedimentation line in front of the head of the groins is substantially attenuated, while the eroded sediment along the deeper part of the groins has obviously been transferred to the beach, forming a new (intense) sedimentation line. The same general trend can be observed in the bottom panel of Figure 43, where the bed evolution for run mcs003E1 (CP_1 = 0.75), is presented. However, the sed/ero patterns of this run seem to combine features of both the reference run and the run with the lower CP_1. The attenuated sedimentation line in front of the head of the groins coupled with the milder sed/ero patterns at shallower depths and at the beach is generally desired as will be discussed in the morphological validation of the model. The aforementioned findings are also presented in the bed profile evolutions of Figure 44 at Mariakerke (Transect 2).

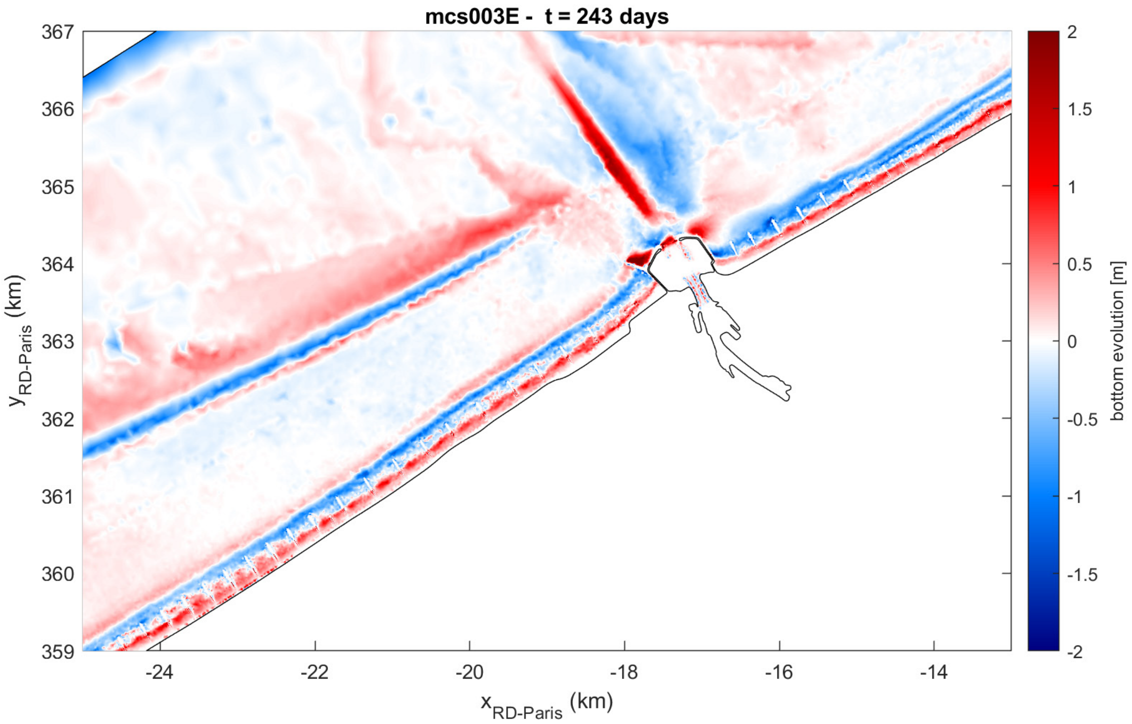

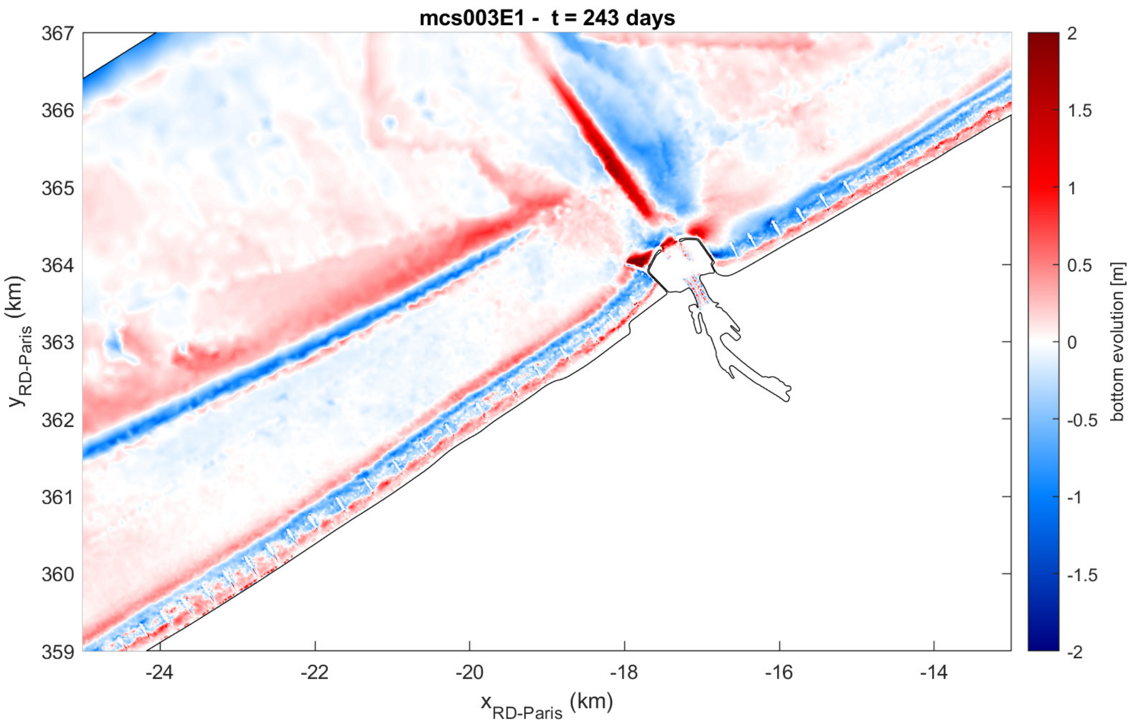

Figure 43: Bed level change [m] at the end of the simulation period (243 days) for the run mcs003E with $CP_1 = 0.5$ (top) and the run mcs003E1 with $CP_1 = 0.75$ (bottom).

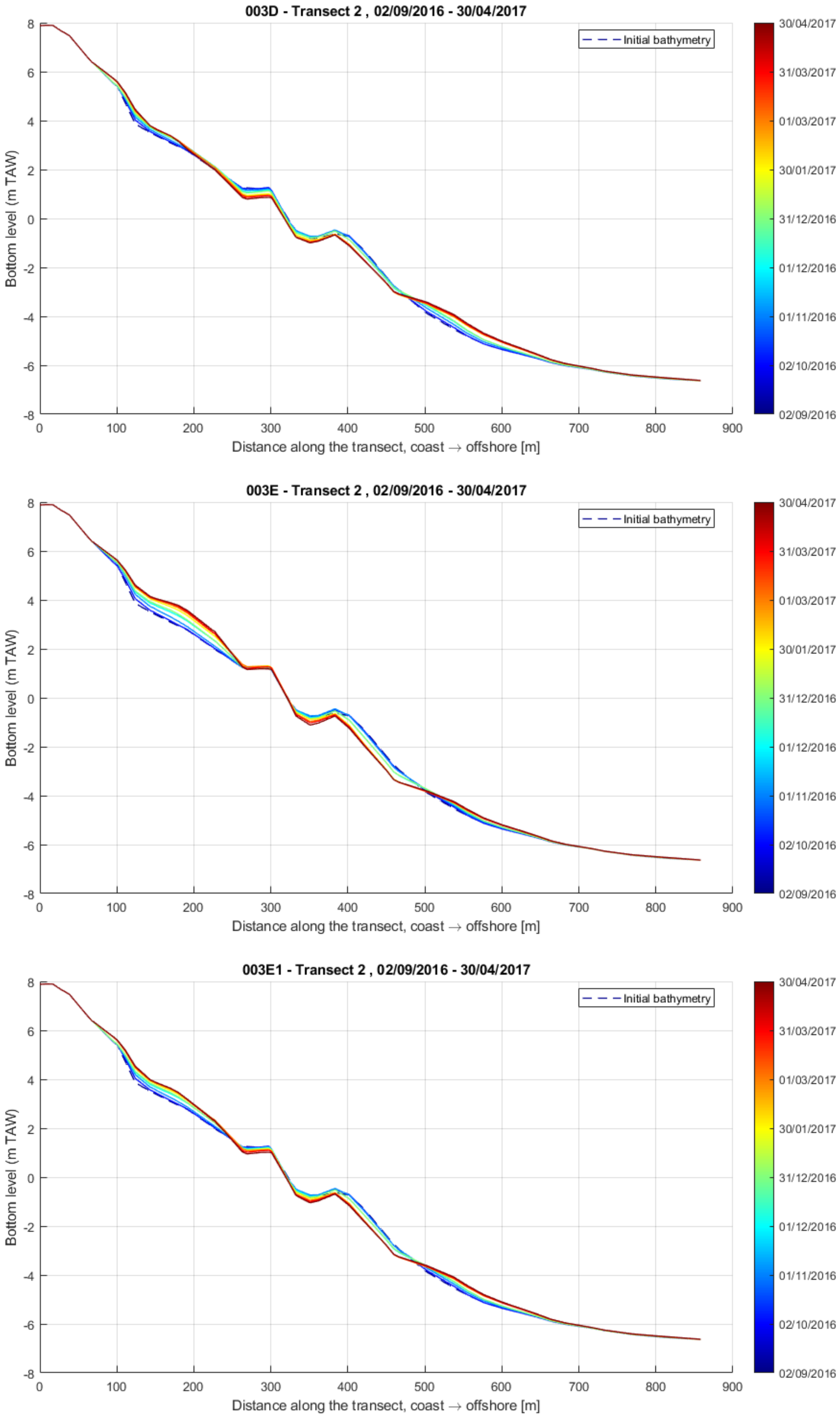

Figure 44: Bed level change [m] at Transect 2 (Mariakerke) during simulations without U_{ST} calibration (top), calibrated U_{ST} with $CP_1 = 0.5$ (middle) and calibrated U_{ST} with $CP_1 = 0.75$ (bottom).

4.3.7 Advection scheme for suspended sediment

In the sensitivity test simulations presented so far, the NERD advection scheme for suspended sediment (option 14) has been utilized. In this section the results of the implementation of the ERIA advection scheme for suspended sediment (option 15) are compared to the NERD's ones. Note that when choosing the ERIA advection scheme, option 3 has to be considered for the treatment of negative depths in the TELEMAC settings.

The total bed level change after 80 days is depicted in Figure 45 for the test run with the ERIA scheme (mcs002I66). Comparing the bed evolution patterns of this test to those of the reference run, i.e., mcs002I42 depicted in Figure 38 (top panel), it can be observed that the ERIA scheme is less diffusive than the NERD one, even though it needs some effort to notice it. This finding is better observed by comparing the bed profile evolution at the eastern 'edge' of Stroombank presented in Figure 46 to the corresponding one of Figure 41 (top panel).

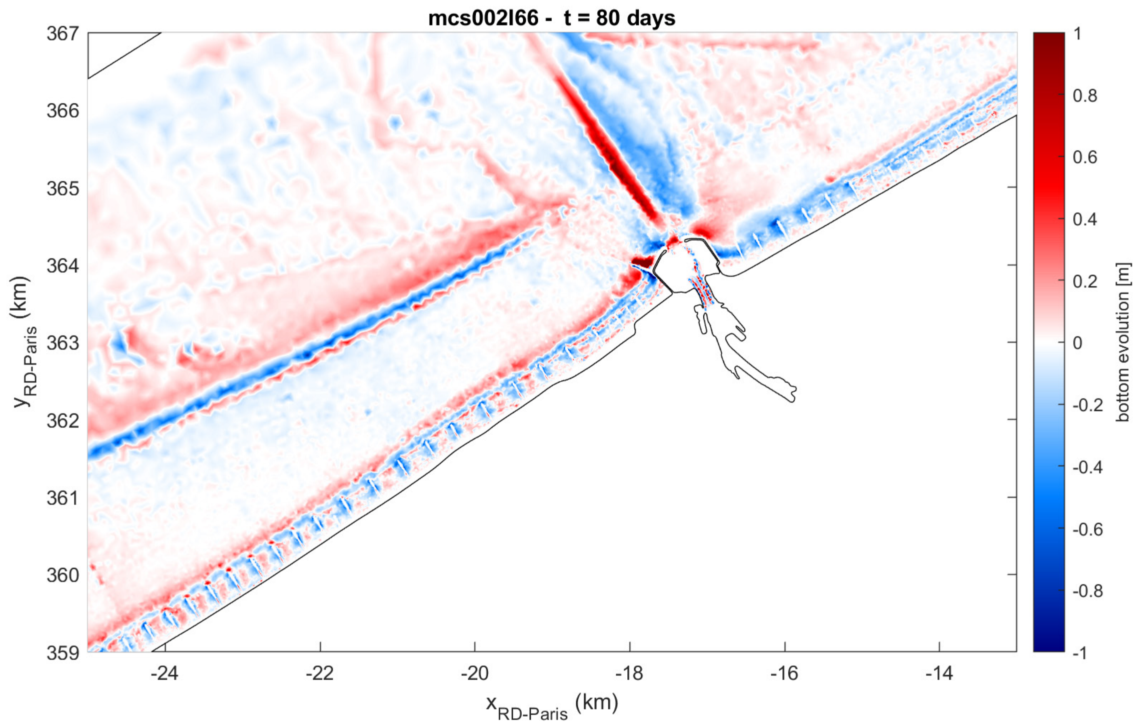

Figure 45: Bed level change [m] at the end of the simulation period for the sensitivity test (mcs002I66) with ERIA advection scheme.

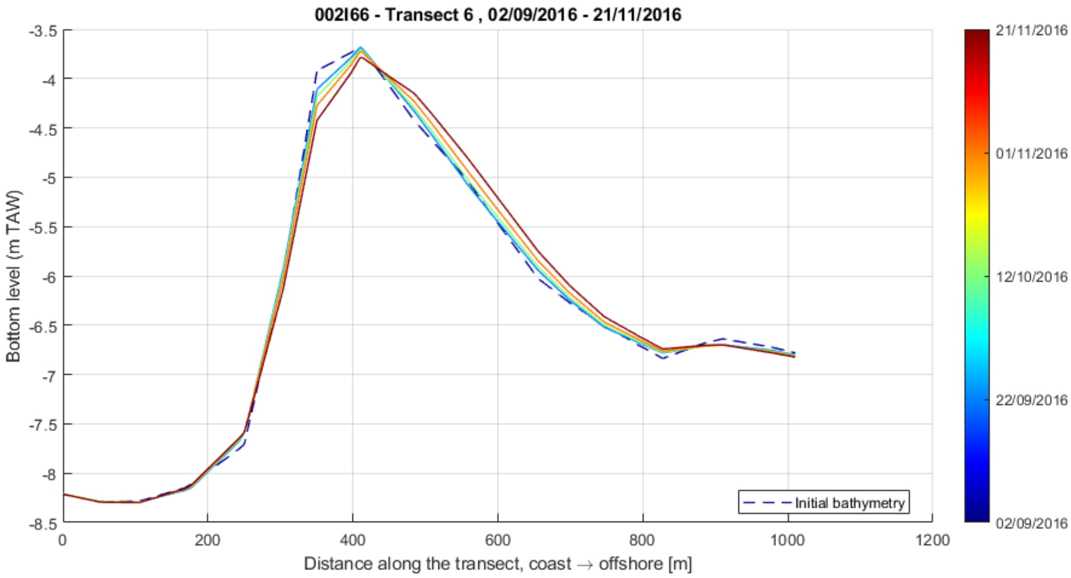

Figure 46: Bed level change [m] at Transect 6 (Stroombank) during simulation mcs002I66 with ERIA advection scheme.

4.3.8 Coupling period for TELEMAC-TOMAWAC

Testing smaller coupling periods for TELEMAC-TOMAWAC equal to 1 min and 5 min, compared to the one used in the hydrodynamic-wave validation (15 min), showed that the effect on the morphological results is negligible.

4.4 Morphological validation

4.4.1 Simulation period

For the morphological validation (hindcasting) a simulation period of 243 days in 2016-2017 (from 02/09/2016 to 02/05/2017) was considered. The selection of the specific period is mainly based on the availability of topographic/bathymetric measurements at the beginning and at the end of the simulation period without any beach/foreshore measurements in between. Furthermore, it was also taken into account that there was availability of wave and wind data.

4.4.2 Measurement data

For the wave forcing of the model time-series from the wave buoy at Ostend Poortjes (OPO), located at the offshore boundary of the TOMAWAC computational domain, are considered for the significant wave height, peak wave period and wave directions. The imposed wave characteristics for the entire simulation period are shown in Figure 47. Note that wave direction is given following TOMAWAC’s convention, i.e. 0^o point to North and 90^o point to East.

Wind time series from Nieuwpoort (NP7) are imposed uniformly on the computational domain of the hydrodynamic module. Wind characteristics for the simulation period are shown in Figure 48.

The locations of the aforementioned stations are depicted in Figure 12 and more information about them is included in Table 4 (see section 3.1).

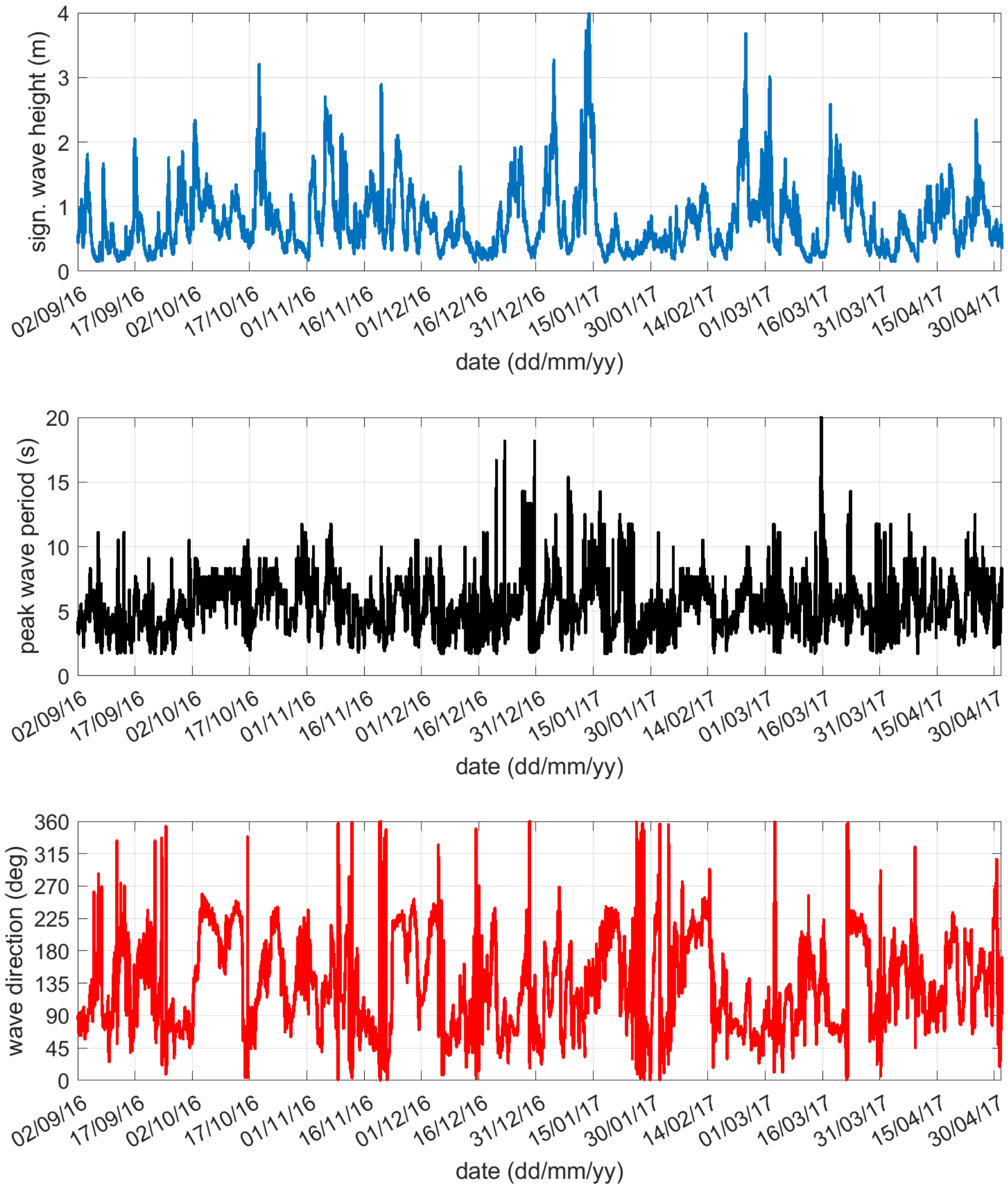

Figure 47: Significant wave height, peak wave period & wave direction measured at Ostend Poortjes (OPO) utilized for the forcing of the model.

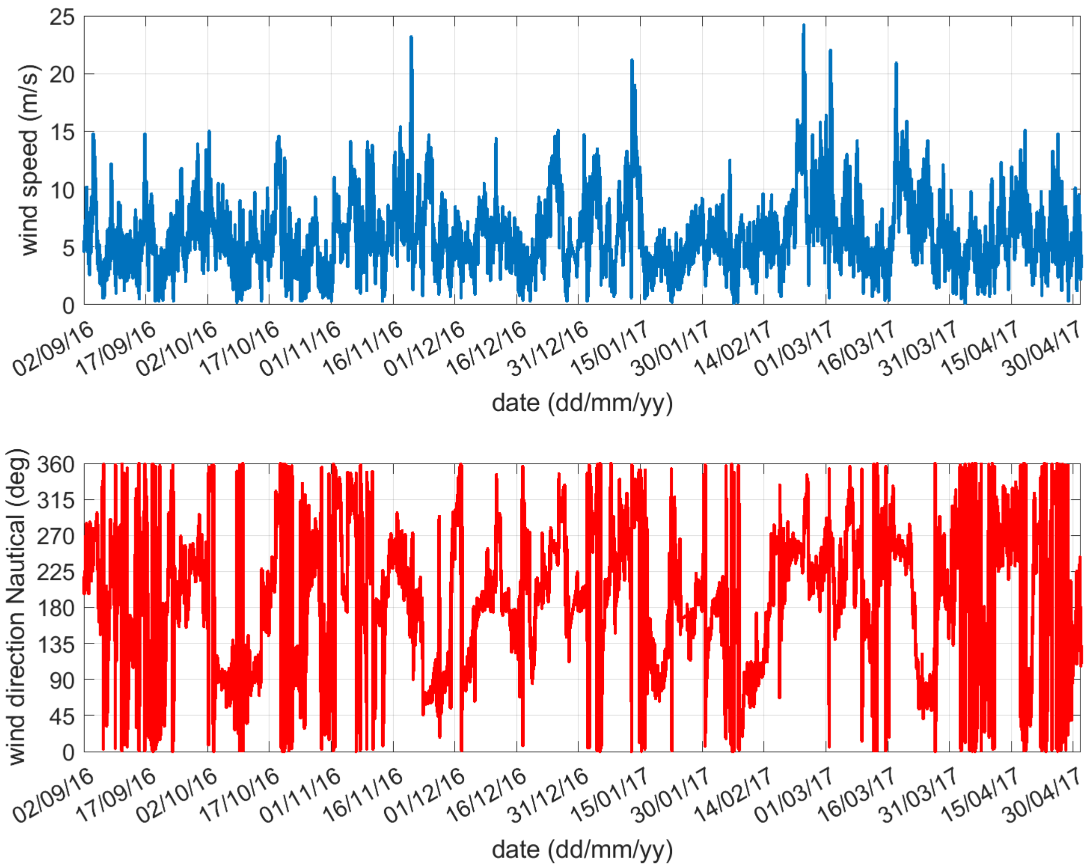

Figure 48: Wind speed & direction measured at Nieuwpoort station (NP7) utilized for the forcing of the model.

The morphological validation of the model is based on bathymetric/topographic data measured at the beginning and at the end of the simulation period, the difference of which, corresponds to the morphological evolution during the investigated period. Information about the bathymetric/topographic data from 2016, utilized for the construction of the model bathymetry, has already been given in section 2.3. As for the data at the end of simulation period, this was retrieved from the same source (Dan et al., 2023). The bed evolution at the end of the considered simulation period (September 2016 – May 2017), at the coastal area west of Ostend harbour, is presented in Figure 49. The topographic data of the beach and the intertidal zone at the area of interest (west of Ostend harbour) come from Lidar measurements conducted the last days of May 2017, while the bathymetric data come from a single-beam survey at the foreshore, conducted in beginning of May 2017.

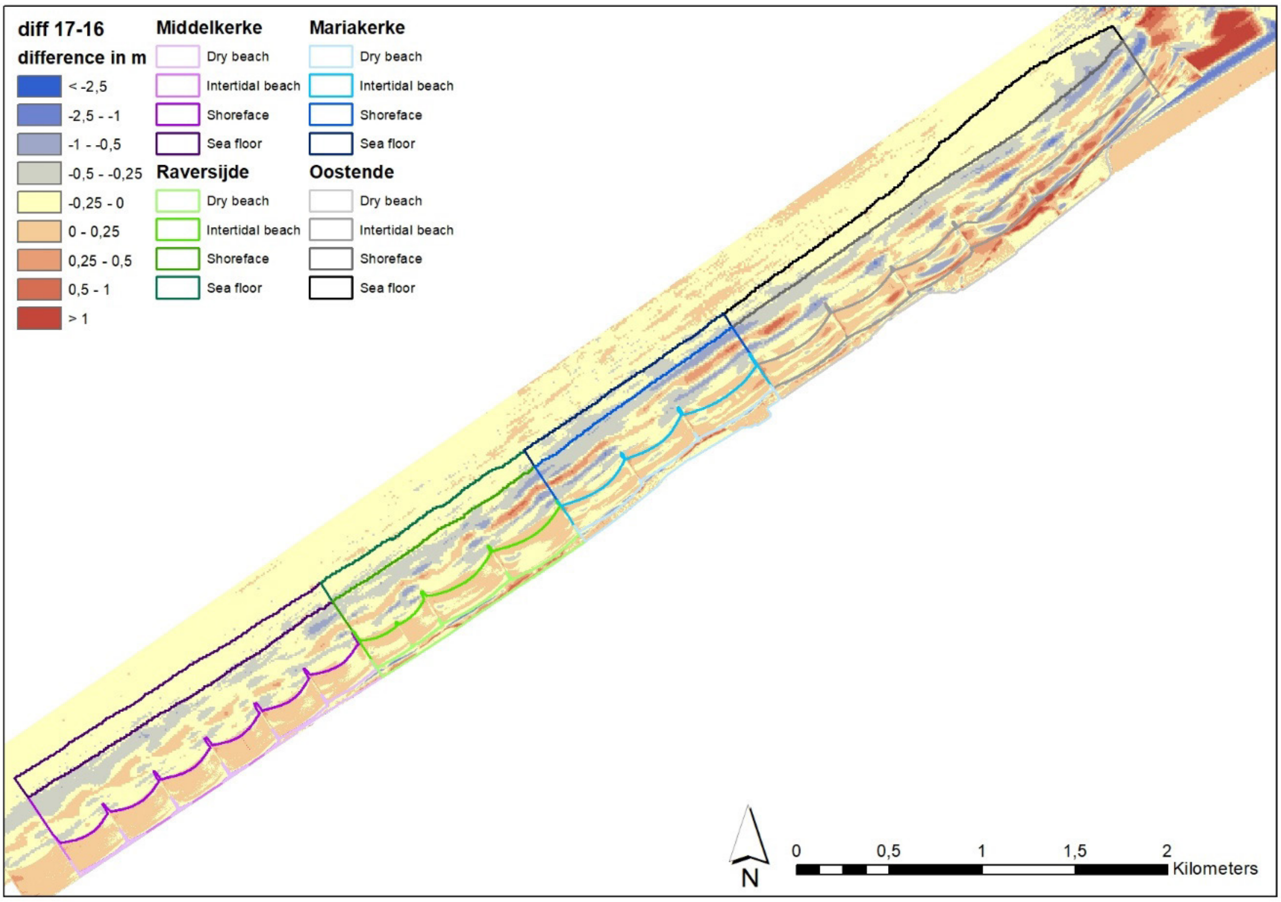

Figure 49: Measured bed level change between 2017 and 2016, at the coastal area west of Ostend harbour (Dan et al., 2023).

4.4.3 Model settings

The basic settings of the hydrodynamic and the wave modules, has already been presented in section 3.3 (Table 6 and Table 7, respectively). However, some additional settings which are related to sediment transport modelling are presented in Table 12. Furthermore the basic settings of the sediment transport and bed-update module (GAIA) are given in Table 13.

Table 12: Additional settings of the Hydrodynamic & Wave modules for morphological simulations.

Hydrodynamic module (TELEMAC-2D)	
Scheme for advection of tracers	15: ERIA scheme for tidal flats
Treatment of negative depths	3: flux control
Wave module (TOMAWAC)	
Surface rollers	ON
BETA S Surface rollers	0.07
Minimum water depth	0.1
Breaking GAMMA1/GAMMA2/ALPHA	0.80/**0.70**/0.80

Table 13: Basic settings of the Morphology module (GAIA).

Morphology module (GAIA)	
Sediment transport equation	Soulsby - Van Rijn (A_{cal} = 0.7; modified to account for both bed load & suspended load)
Suspension for all sands	ON
Bed load for all sands	OFF
Morphological factor (MOFAC)	1
D_{50} / D_{90}	250 µm /375 µm
Effect of waves	ON
Cross-shore current	ON
Cross-shore Asymmetry (f_{As}) / Skewness factor (f_{Sk})	0.1 / 0.4
Constant near-bed concentration ratio R_{cs}	Varying 10 (maximum value)
Slope effect	OFF
Advection scheme for suspended sediments	15: Eria scheme
Scheme option for advection of suspended sediments	1: Explicit scheme

4.4.4 Results

The bed level change between 2017 and 2016, presented in Figure 49 (section 4.4.2), is interpolated on the computational grid of Ostend model so that the comparison with the corresponding numerical results becomes easier. The interpolated measured bed level change (2017-2016) is presented in Figure 50.

A set of numerical simulations listed in Table 14 were executed in order to evaluate/validate the Ostend model with the optimal settings presented in the previous section, switching on and off the cross-shore current contribution. Moreover the influence of the wind-induced current on the bed evolution was checked.

Table 14: Morphological simulations for the evaluation of Ostend model.

Run ID	CROSS-SHORE CURRENT	WIND
mcs003Q2	OFF	ON
mcs003R	ON	OFF
mcs003R1	ON	ON

In Figure 51 and Figure 52, the numerically predicted bed evolution at the end of the simulation period is presented for the runs with activated cross-shore current and wind-induced current deactivated (mcs003R) and wind-induced current activated (mcs003R1), respectively. First of all, comparing these two figures to each other, almost no differences are observed at the coastal area west of Ostend harbor. On the contrary, it seems that the presence of wind in the hydrodynamic calculations results into relatively more intense sed/ero patterns along the Stroombank, indicating relatively enhanced movement of sediment of the crest to the offshore side of the bank. This behaviour could probably be attributed to the prevailing southwest winds during the simulation period.

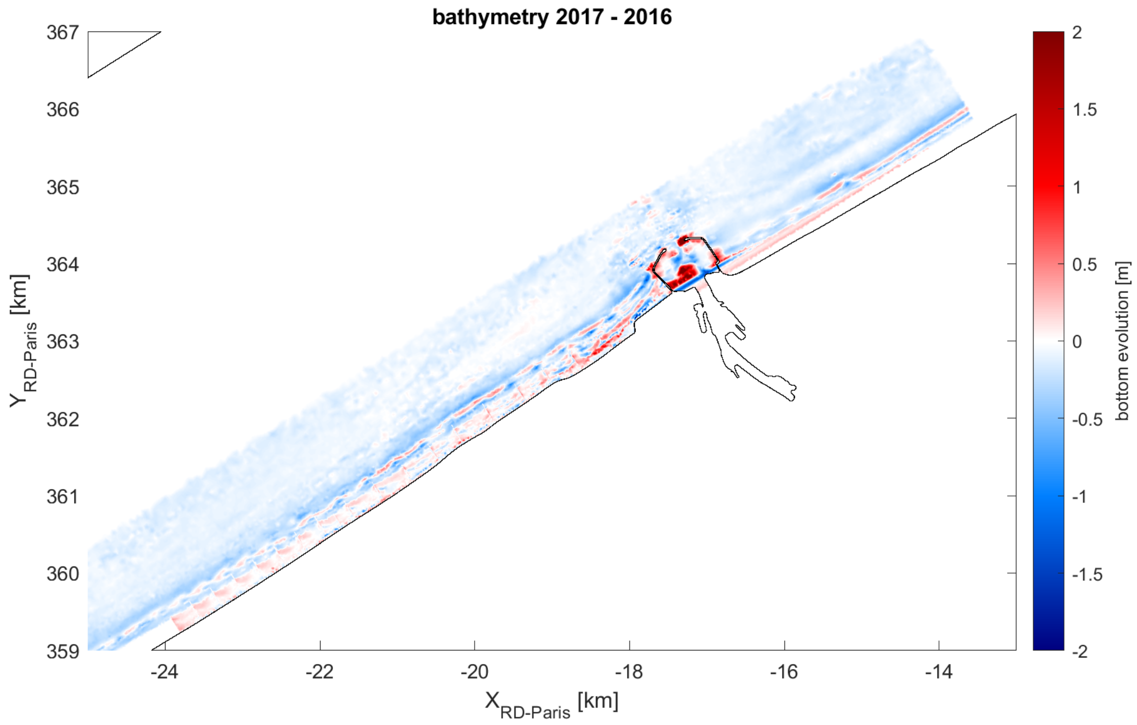

Figure 50: Measured bed level change [m] between years 2017 and 2016 interpolated on the computational grid of Ostend model.

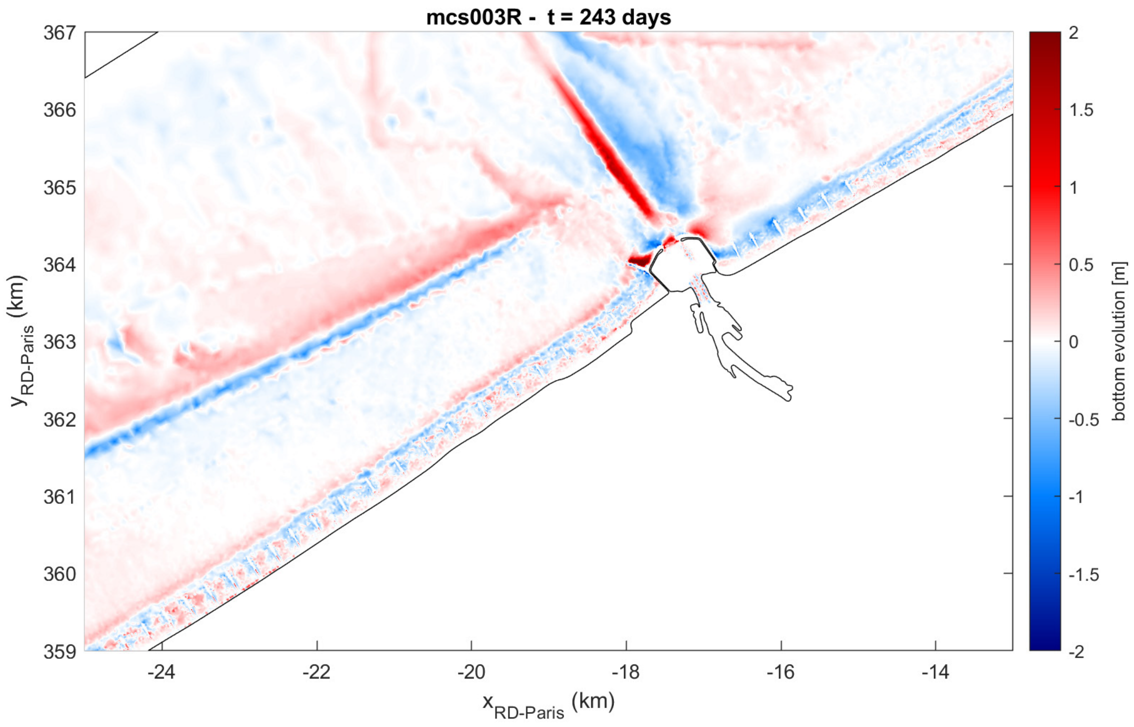

Figure 51: Bed level change [m] at the end of the simulation period (243 days) for the run (mcs003R) with cross-shore current and deactivated wind-induced current.

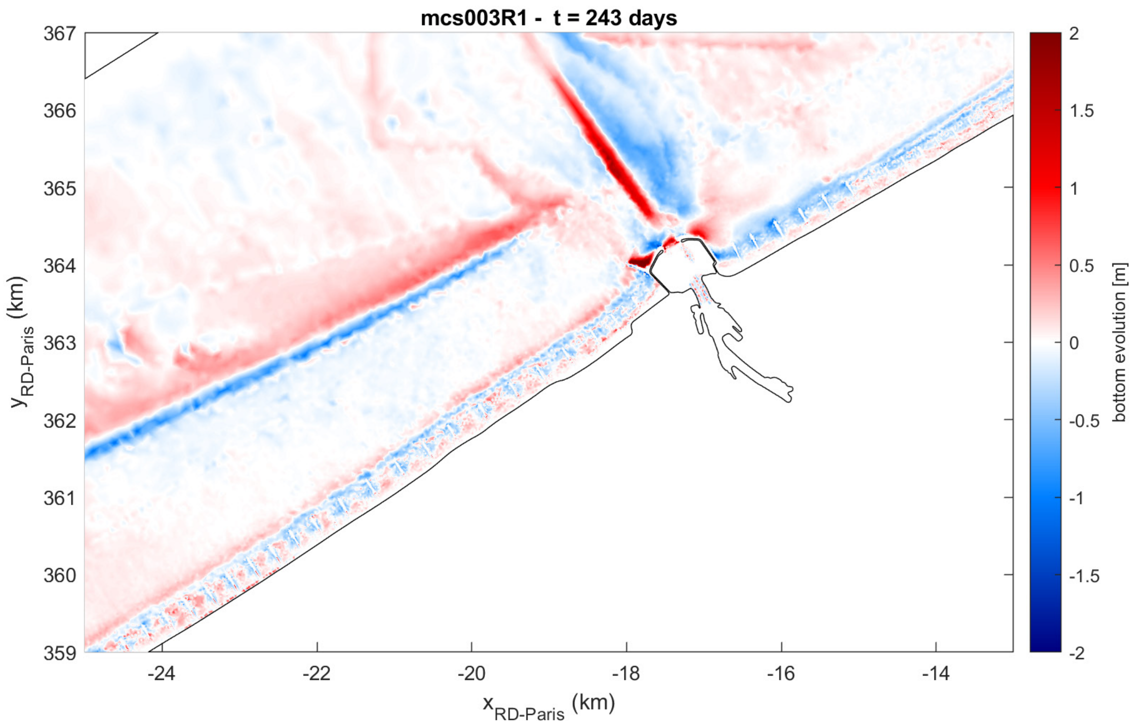

Figure 52: Bed level change [m] at the end of the simulation period (243 days) for the run with cross-shore current and wind-induced current.

Comparing the numerically predicted beach-foreshore sed/ero patterns of Figure 51 (or Figure 52) to the measured ones of Figure 50, focusing at the west of Ostend harbour, some main observations could be made.

- The order of magnitude of the numerically predicted bed level changes are similar to the measured ones.
- The measured sedimentation between the groins is more or less predicted by the model especially at the western part of the area of interest.
- The model predicts relatively more erosion between the groins at the middle part of the area of interest.
- The model seems to predict reasonably well the sed/ero patterns at the eastern part of the coast (close to Ostend harbour). It is very likely though, that the measured sedimentation around X_{RD} = 18 km is a human intervention and not a natural process, even though it is not recorded as a nourishment action.
- The numerically predicted sedimentation line along the tips of the groins is located somewhat deeper than the measured one. The latter seems to present some gaps, while the numerical one seems to be continuous and a bit diffusive.
- There seems to be an erosion line shoreward of the sedimentation line in the measurements which is more or less predicted by the model.
- The measured erosion line which is located deeper than the aforementioned sedimentation line is not predicted by the model.
- The model shows strong sedimentation at the underwater part of the western harbour dam and east of the harbour, which is not observed, or less pronounced in the measurements.

For illustrative purposes, the mcs003R1 run is repeated with deactivated cross-shore current contribution (run mcs003Q2). The numerical results for bed evolution are presented in Figure 53. Comparing the sed/ero patterns of the aforementioned figure with those of Figure 52, it can generally be observed that the patterns among the groins are smoother and that less erosion occurs when cross-current is not taken into account. Moreover the sedimentation and the erosion lines in front of the tips of the groins are no longer that obvious when the cross-shore current is absent.

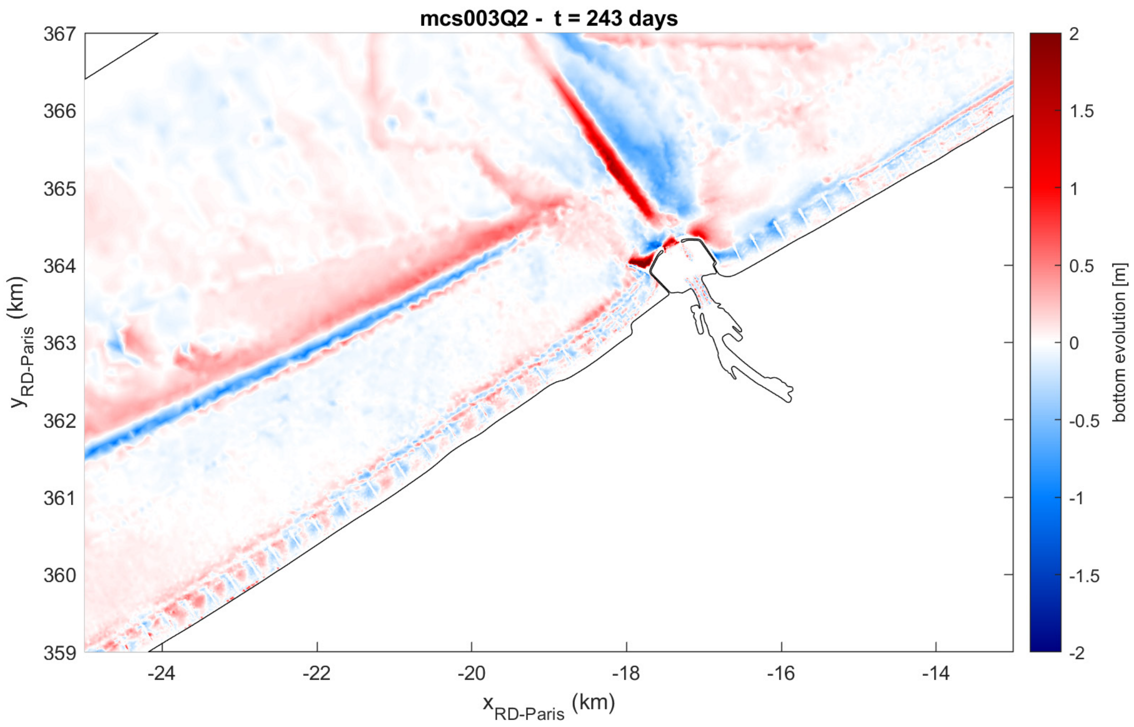

Figure 53: Bed level change [m] at the end of the simulation period (243 days) for the run without cross-shore current (wind-induced current is on).

More insight of the model's behaviour can be obtained by the comparison of measured and numerical bed profile evolutions at the selected transects that have already been shown in Figure 27 (section 4.3.1). In Figure 54 to Figure 56, numerically predicted bed evolutions at three transects at the coastal area west of Ostend harbour, i.e. Transect 1 (Raversijde), Transect 2 (Mariakerke) and Transect 3 (Ostend – west dam), for both runs with and without cross-shore current, are compared to the measured ones. Note that the measured (and the numerical) profiles are extracted from the bathymetry/topography interpolated to the computational grid. In general the Ostend model with cross-shore current included, achieves predictions with a reasonable agreement to the measured profiles. The differences between the modelled bed evolutions (with and without cross-shore current) become larger for the profile parts below the lower waterline (0 m TAW) especially for Transects 2 and 3. At these parts of the profiles the activation of the cross-shore current helps the model to perform better.

The modelled bed profile evolution at two transects across the Stroombank (Transect 5 & 6 shown in Figure 27), is presented in Figure 56 and Figure 57, where the effect of activating cross-shore current is indicated. The main finding is that the offshore directed cross-shore current restricts the sliding of sediment of the bank's shoreward side to the shallower are, while it enhances the offshore movement of the bank slightly compared to the simulation without cross-shore current.

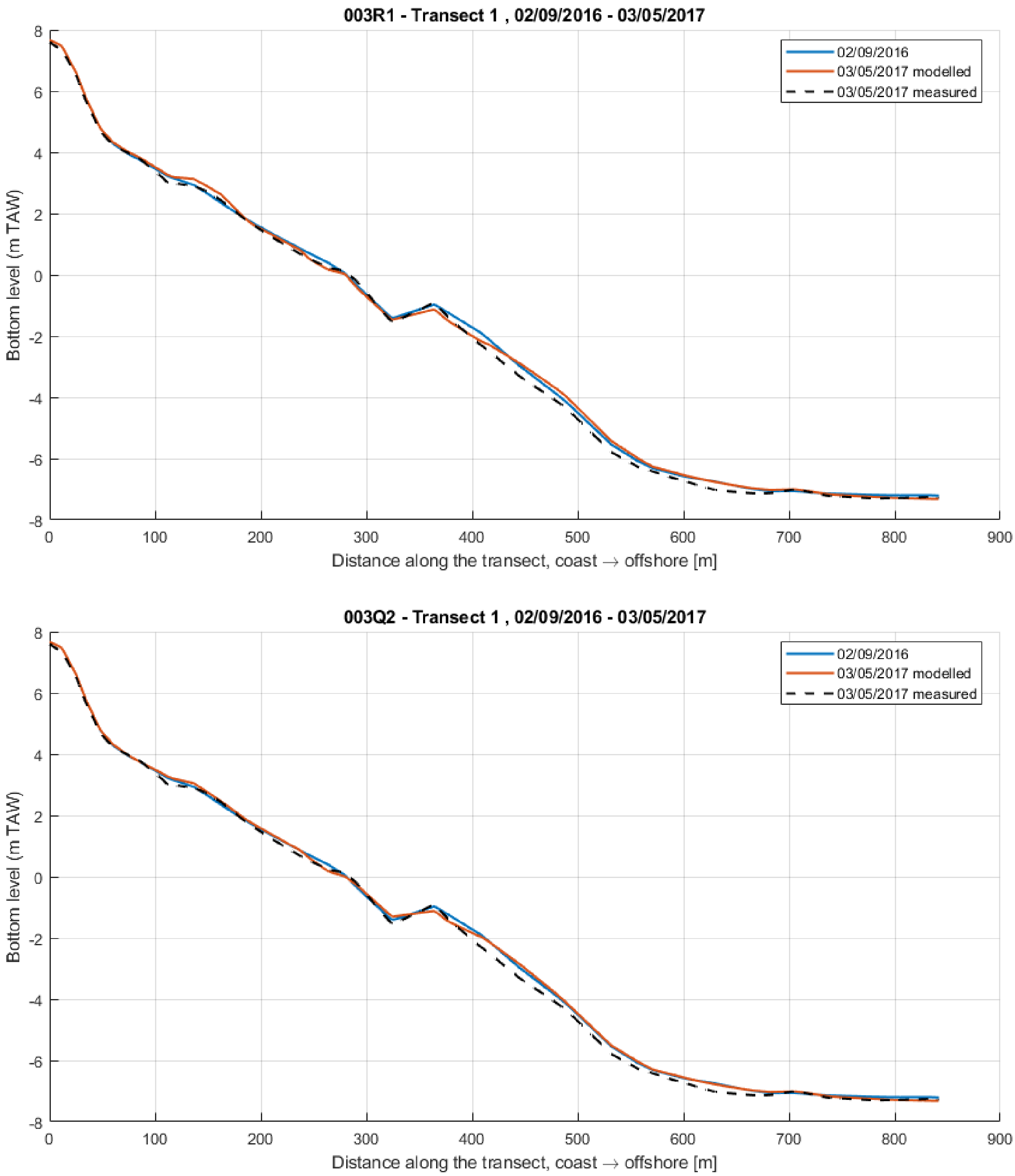

Figure 54: Measured vs modelled bed level change [m] at Transect 1 (Raversijde) for the run with cross-shore current [Wind = ON] (top), and the run without cross-shore current [Wind = ON] (bottom).

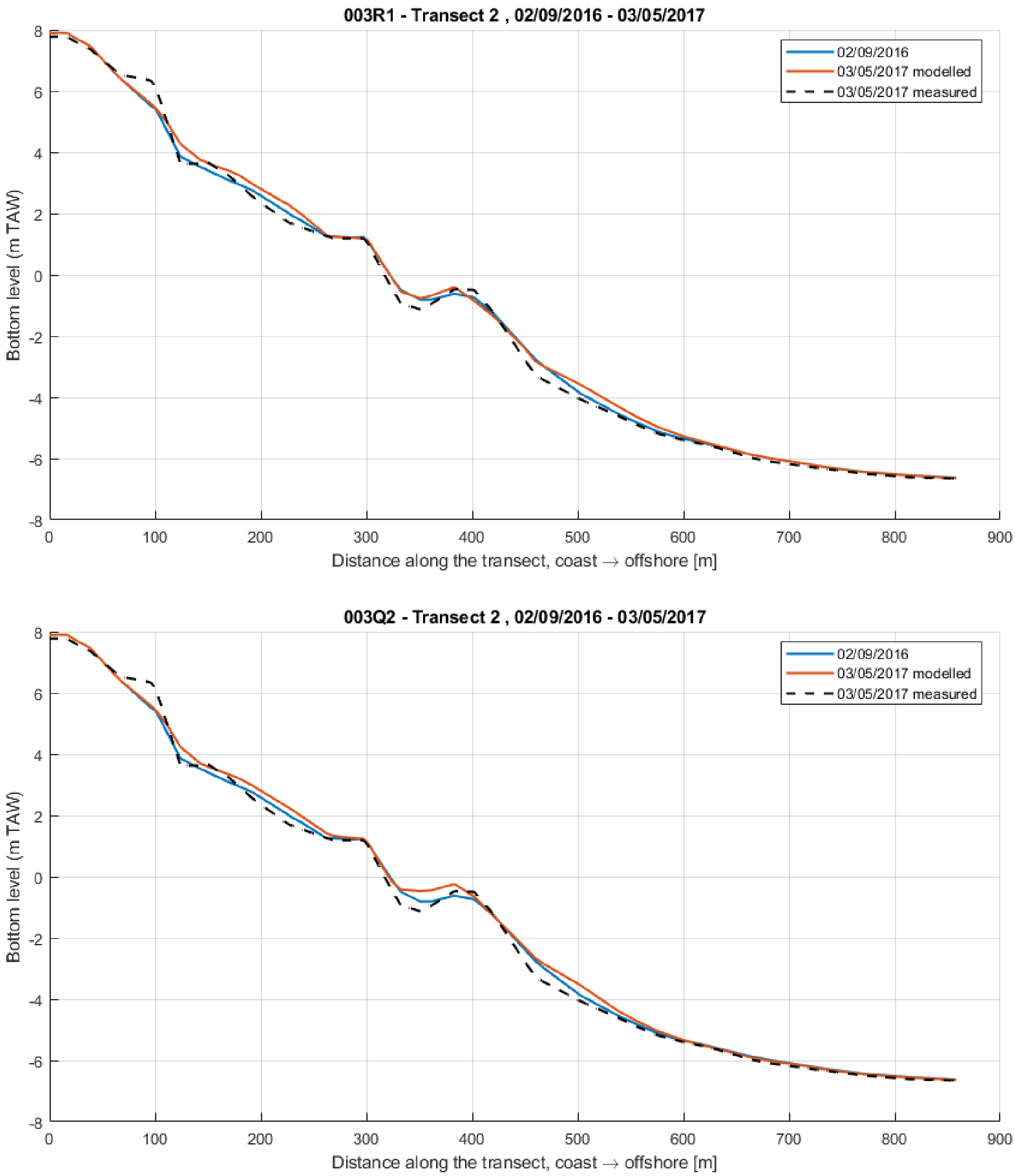

Figure 55: Measured vs modelled bed level change [m] at Transect 2 (Mariakerke) for the run with cross-shore current [Wind = ON] (top), and the run without cross-shore current [Wind = ON] (bottom).

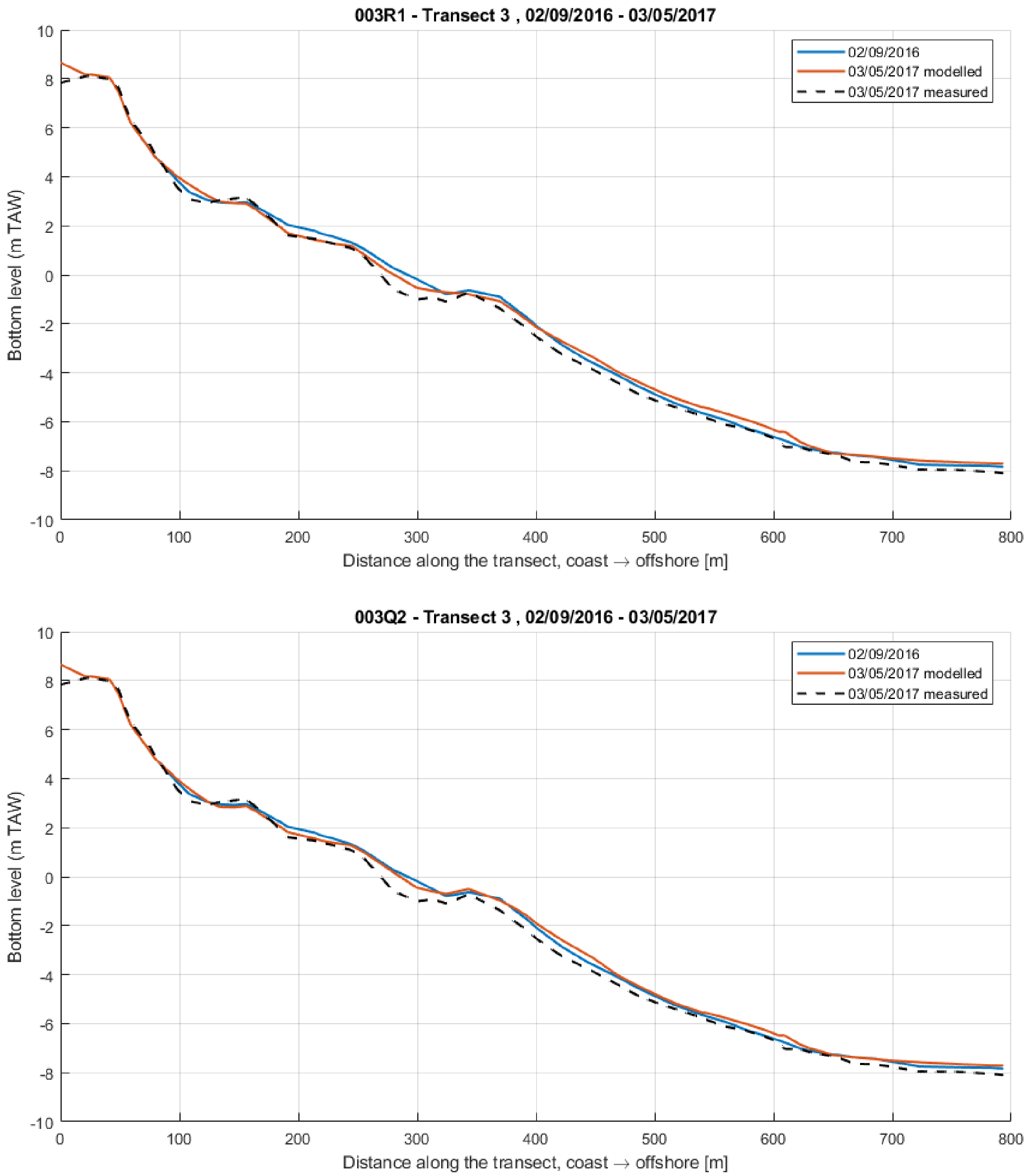

Figure 56: Measured vs modelled bed level change [m] at Transect 3 (Ostend – west dam) for the run with cross-shore current [Wind = ON] (top), and the run without cross-shore current [Wind = ON] (bottom).

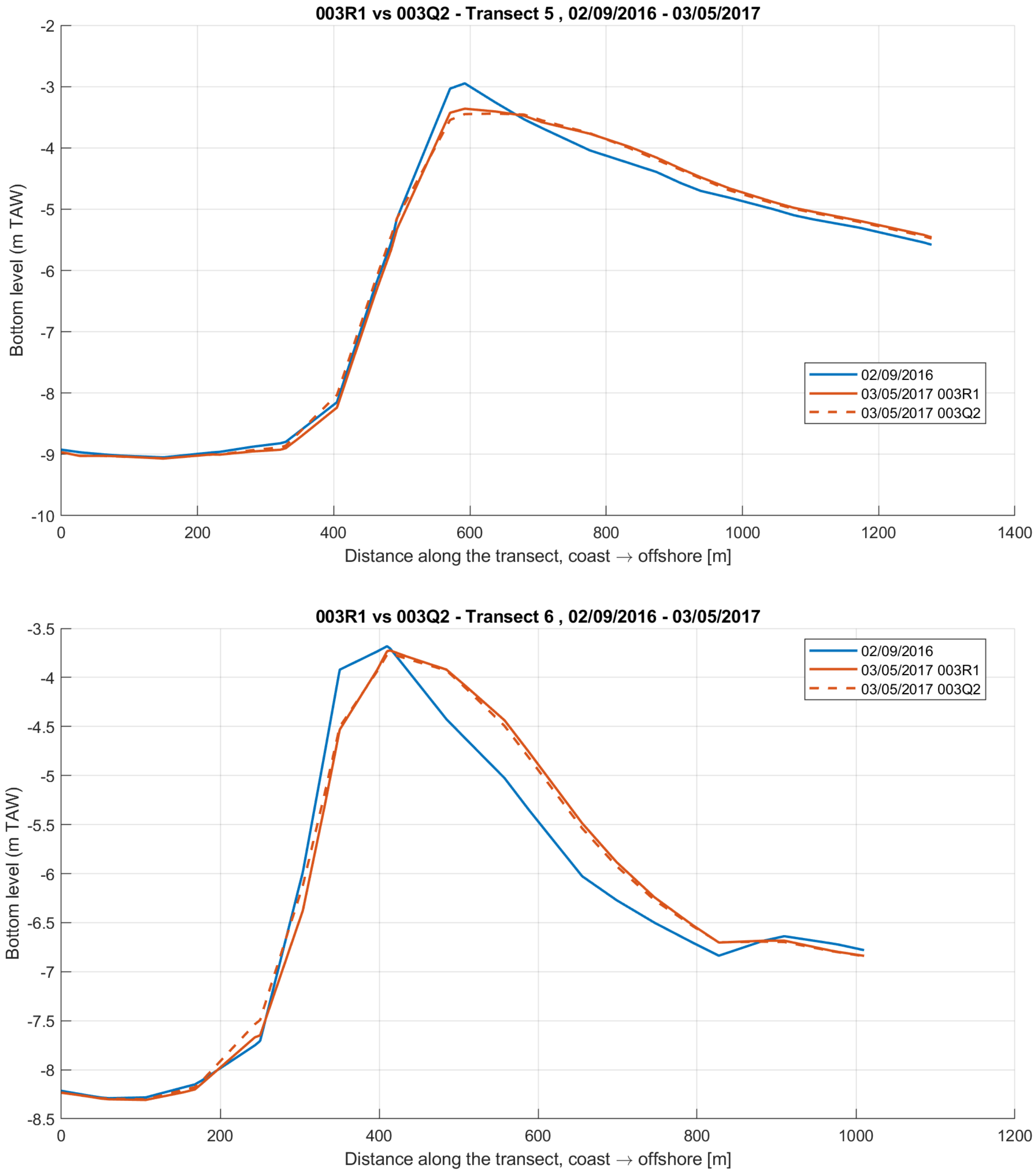

Figure 57: Modelled bed level change [m] at Transect 5 (top) and Transect 6 (bottom) of Stroombank for the run with cross-shore current (mcs003R1) and the run without cross-shore current (mcs003Q2).

5 Conclusions

The main goal of the presented work was the evaluation of a 2D-morphodynamic model for the central part of the Belgian coast, the so-called Ostend model, which was constructed so that the new developments on the cross-shore transport modelling can be validated against larger scale (field) measurements under realistic (measured) forcing conditions. The modelling strategy involved online coupling of the TELEMAC-2D, TOMAWAC and GAIA modules using the TEL2TOM functionality (Breugem et al., 2019) and the implementation of Neumann conditions at the lateral boundaries of the hydrodynamic model (Breugem et al., 2018). The major cross-shore processes incorporated in the model are the Stokes drift (return flow), the surface rollers, the wave non-linearity and the wave breaking induced turbulence.

First, the calibration and validation of the hydrodynamic and the wave modules against tidal current and wave measurements at the nearshore area of Ostend, took place. As for the tidal currents, numerical results were compared to field measurements at the two frames, Hercules and Hylas I, deployed at Mariakerke in autumn 2015. For the wave validation, recordings from two wave buoys at Raversijde and Ostend eastern palisade, were considered. The results of the validation confirm the very good performance of the coupled hydrodynamic-wave modules of Ostend model.

Then the results of the morphological simulations, performed in order to evaluate the updated GAIA module in predicting bottom changes in the surf zone in the time-scale of one year, were presented. A series of sensitivity tests for various numerical and physical parameters and mechanisms introduced in the GAIA module took place first, in order to get a deeper insight of the most important parameters of cross-shore transport in field conditions and more easily calibrate the morphology module. It was found that the model presented substantial sensitivity in a series of parameters, such as wave asymmetry and skewness factors, the ratio between near-bed concentration and the mean concentration and the advection scheme for suspended sediment. Besides, tuning of return flow and the Soulsby-van Rijn equilibrium concentration C_{eq} was performed. Bed evolution (high-order) filtering, with low contribution in the numerical diffusion, was also successfully applied for smoothening instabilities that appear at the shallow (intertidal) area along the coast.

Finally, the model was validated by means of morphological hindcasting taking advantage of the available bathymetric/topographic measurements at the coastal area west of Ostend harbor from the period 2016-2017, which was free from beach/foreshore nourishments. In general the results of Ostend model with cross-shore current included, are in reasonable agreement to the measured profiles.

References

Bosboom, J., & Stive, M. J. F. (2023). Coastal dynamics. In *Hydro Delft: Vol. 1.2*. https://doi.org/10.5074/t.2021.001

Breugem, W. A. (2020). Ongoing developments in TELEMAC and TOMAWAC in IMDCOngoing developments in TELEMAC and TOMAWAC in IMDC. *Proceedings of the XXVIIth TELEMAC-MASCARET User Conference, 14-16 October 2020, Antwerp*.

Breugem, W. A. (2022). Wetting and drying improvements in TELEMAC. *Proceedings of the XXVIIIth TELEMAC-MASCARET User Conference, 18-19 October 2022, Paris-Saclay*.

Breugem, W. A., Fonias, E., Wang, L., Bolle, A., Kolokythas, G., & De Maerschalck, B. (2018). Neumann boundaries in TELEMAC 2D and their application to wave current interaction. *XXVth TELEMAC-MASCARET User Conference (in Publication)*.

Breugem, W. A., Fonias, E., Wang, L., Bolle, A., Kolokythas, G., & De Maerschalck, B. (2019). TEL2TOM: coupling TELEMAC2D and TOMAWAC on arbitrary meshes. *XXVIth Telemac-Mascaret User Conference, 15-17 October, Toulouse: Proceedings*.

Breugem W.A., Doorme S., Bakhtiari A., Figard J., & Di Lauro. (2021). Speeding up TOMAWAC by means of improved numerical methods. *Proceedings of the XXVIIth TELEMAC-MASCARET User Conference, 14th to 15th October 2021, Antwerp*.

Cobo, P. T., Kirby, J. T., Haller, M. C., Ozkan-Haller, H. T., Magallen, J., & Guannel, G. (2007). MODEL SIMULATIONS OF BAR EVOLUTION IN A LARGE SCALE LABORATORY BEACH. *Coastal Engineering 2006*, 2566–2578. https://doi.org/doi:10.1142/9789812709554_0217

Dan, S., Vos, G., Nguyen, D., Montreuil, A.-L., & Verwaest, T. (2023). *Coastal Morphology at Mariakerke: final Report: Vol. 00_128_16* (Version 3., FH Reports). Flanders Hydraulics. https://documentatiecentrum.watlab.be/owa/imis.php?module=ref&refid=363286

Dastgheib, A. (2012). Long-term Process-based Morphological Modeling of Large Tidal Basins. In *UNESCO-IHE Institute for Water Education: Vol. PhD Thesis*.

Fonias, E., Breugem, W. A., Wang, L., Wang, L., Bolle, A., Kolokythas, G., & De Maerschalck, B. (2021). Implementation of cross-shore processes in GAIA. In *Proceedings of the papers submitted to the 2020 TELEMAC-MASCARET user conference - October 2021* (pp. 138–143). [S.n.]. http://0.5.78.221

Geuzaine, C., & Remacle, J.-F. (2009). Gmsh: a three-dimensional finite element mesh generator with built-in pre-and post-processing facilities. *International Journal for Numerical Methods in Engineering 79(11), 0*, 1309–1331. https://doi.org/10.1002/nme.2579

Kolokythas, G., De Maerschalck, B., Wang, L., Fonias, E., & Breugem, W. A. (2019). Scaldis-Coast: An Integrated Numerical Model for the Simulation of the Belgian Coast Morphodynamics. *Geophysical Research Abstracts (Vol. 21)*.

Kolokythas, G., De Maerschalck, B., Wang, L., Fonias, S., Breugem, W. A., Vanlede, J., & Mostaert, F. (2021). *Modelling Belgian Coastal zone and Scheldt mouth area Modelling Belgian Coastal zone and Scheldt mouth area Sub report 12: Scaldis-Coast model – Model setup and validation of the 2D hydrodynamic model*.

Montreuil, A.-L., Dan, S., Vereecken, H, B., De Backer, E., Verzhbitskiy, L., Claeys, S., Deschamps, M., & Mostaert, F. (2015). *Alternative measures for beach nourishment maintenance: monitoring of a pilot experiment at Mariakerke: Measuring campaign October November 2015.*

Roelvink, D., Reniers, A., van Dongeren, A., van Thiel de Vries, J., McCall, R., & Lescinski, J. (2009). Modelling storm impacts on beaches, dunes and barrier islands. *Coastal Engineering*, *56*(11), 1133–1152. https://doi.org/https://doi.org/10.1016/j.coastaleng.2009.08.006

Roelvink, J. A., & Stive, M. J. F. (1989). Bar-generating cross-shore flow mechanisms on a beach. *Journal of Geophysical Research: Oceans*, *94*(C4), 4785–4800. https://doi.org/https://doi.org/10.1029/JC094iC04p04785

Soulsby, R. (1997). *Dynamics of marine sands*. H.R. Wallingford.

Svendsen, I. A. (1984). Mass flux and undertow in a surf zone. *Coastal Engineering*, *8*(4), 347–365. https://doi.org/https://doi.org/10.1016/0378-3839(84)90030-9

van Thiel de Vries, J. S. M. (2009). Dune erosion during storm surges. In *Delft, the Netherlands, Delft Hydraul. Lab., Sep. 2009*.

DEPARTMENT **MOBILITY & PUBLIC WORKS**
Flanders hydraulics

Berchemlei 115, 2140 Antwerp
T +32 (0)3 224 60 35
F +32 (0)3 224 60 36
flanders.hydraulics@vlaanderen.be
www.flandershydraulics.be